INFORMATION TO USERS

This manuscript has been reproduced from the microfilm master. UMI films the text directly from the original or copy submitted. Thus, some thesis and dissertation copies are in typewriter face, while others may be from any type of computer printer.

The quality of this reproduction is dependent upon the quality of the copy submitted. Broken or indistinct print, colored or poor quality illustrations and photographs, print bleedthrough, substandard margins, and improper alignment can adversely affect reproduction.

In the unlikely event that the author did not send UMI a complete manuscript and there are missing pages, these will be noted. Also, if unauthorized copyright material had to be removed, a note will indicate the deletion.

Oversize materials (e.g., maps, drawings, charts) are reproduced by sectioning the original, beginning at the upper left-hand corner and continuing from left to right in equal sections with small overlaps.

Photographs included in the original manuscript have been reproduced xerographically in this copy. Higher quality 6" x 9" black and white photographic prints are available for any photographs or illustrations appearing in this copy for an additional charge. Contact UMI directly to order.

ProQuest Information and Learning
300 North Zeeb Road, Ann Arbor, MI 48106-1346 USA
800-521-0600

UMI®

Rapid Prototype Development of PEM Fuel Cell Gas Delivery Plates

by

Rong Zheng
B.Eng., Tsinghua University, People's Republic of China
M.Phil., The Hong Kong Polytechnic University
M.Sc., University of California, Los Angeles, United States of America

A Thesis Submitted in Partial Fulfillment of the
Requirements for the Degree of

Doctor of Philosophy

in the Department of Mechanical Engineering

We accept this thesis as conforming
to the required standard

Dr. Z. Dong, Supervisor, (Department of Mechanical Engineering)

Dr. N. Djilali, Departmental Member, (Department of Mechanical Engineering)

Dr. J. Provan, Departmental Member, (Department of Mechanical Engineering)

Dr. D. Harrington, Outside Department Member, (Department of Chemistry)

Dr. D. Xue, External Examiner, (University of Calgary)

Supervisor: Dr. Zuomin Dong

Abstract

This research focuses on new rapid prototype development techniques for Proton Exchange Membrane (PEM) fuel cell gas delivery plates. The study addresses several key issues in the design, analysis and manufacturing of fuel cell plates. The approach combines theoretical modeling, experimental study, physical plate making process, and virtual prototyping to form a new scheme for the rapid prototype development of fuel cell plates.

The research extends the newly introduced screen-printing layer deposition manufacturing technique to complete the entire cycle of rapid plate development. A number of key issues on plate materials and the layer deposition process are addressed. The study has identified the cause of the problem with the poster-ink based screen-print ink material, explored various alternative composite ink materials, and narrowed down to the promising "conductive polymer ~ epoxy ~ graphite power" composite. A new, concurrent approach for developing new composite materials through various experiments and material tests has been introduced, and demonstrated through the development of one particular ink composite with promising results.

In this research, the method for virtual prototyping fuel cell gas delivery plate using advanced CAD/CAE commercial software is introduced. The method allows a "virtual prototype" of the fuel cell plate to be constructed and the performance of the plate to be evaluated through various analyses as "virtual prototype tests." These include the prediction of fuel cell performance through the CFD calculation on the average oxygen concentration; as well as the assessments of the maximum stress and undesirable temperature variation on the printed fuel cell plate through finite element analysis.

Design optimization is conducted using the virtual prototypes to improve the design of the flow field and the plate. Three disciplinary models are simulated and their results are subject to disciplinary optimizations. Global design optimization is carried out using multiple objective optimization, combining the functional performance measures from three disciplinary models. This multi-disciplinary optimization integrates performance considerations of PEM fuel cell plate, and provides guidelines to the plate development.

The research contributes to a new approach for the rapid development of fuel cell plates with a great potential to be applied to other mechanical parts. The study also extends the methodology of computational design and rapid prototyping.

Examiners:

____

Dr. Z. Dong, Supervisor, (Department of Mechanical Engineering)

____

Dr. N. Djilali, Departmental Member, (Department of Mechanical Engineering)

____

Dr. J. Provan, Departmental Member, (Department of Mechanical Engineering)

____

Dr. D. Harrington, Outside Department Member, (Department of Chemistry)

____

Dr. D. Xue, External Examiner, (University of Calgary)

Table of Contents

List of Tables

List of Figures

Acknowledgement

First, I would like to express my appreciation to all members of supervisory committer for their advice on this multiple disciplinary research. Thanks to Dr. James W. Provan for his advice on material mechanics at the early stage of the research. Thanks to Dr. Nedjib Djilali for his help on computational fluid dynamics. Thanks to Dr. David A. Harrington for his guidance on fuel cell electrochemistry and the use of equipments in the Dept. of Chemistry.

Special thanks to Dr. Steven Holdcroft at Simon Fraser University for his advice on conductive polymer composites. Some of the experiment work was done in his research lab. In particular, Dr. Jianfei Yu helped on the tests.

I would also like to thank my colleagues, including Walter Merida, Torsten Berning, Dr. Jun Cao, Dr. Dongming Lu, Dr. Gary Wang and Ryan Mackie for sharing their knowledge and insights. Thank all supporting staffs who have assisted me during the past four years.

I wish to thank my wife Zhe Chen for her patience and love during these years of study, as well as her efforts to bring me two lovely babies, Jesse and Alyssa, in the past four years.

Finally, I would like to express my sincere acknowledgement to my supervisor, Dr. Zuomin Dong, for the very valuable supervision and advice on the study. His help is not only on the large amount of detailed work, but also on the idea and methodology, especially in this multiple disciplinary research work. "Know what you need to do before start doing it."

Dedications

To my grandparents.

My grandmother passed away in Beijing, China, on April 16, 1998, a few days before I joined to University of Victoria. My grandfather passed away also in Beijing, China, on November 17, 2001, when I was writing this doctorial dissertation. I will forever remember the happy years of my childhood and juvenile, with my grandparents. I was raised with my grandparents. During my family's hardest China's Culture Revolution years, they always encouraged me to be able to overcome any difficulty in life.

Chapter 1. Introduction

1.1 Background

1.1.1 Fuel Cell Technology: History and Advantage

A fuel cell is an electrochemical device that produces electricity through a controlled electrochemical reaction of hydrogen and oxygen. A fuel cell converts hydrogen fuel, obtained from natural gas, methanol, etc., and oxygen from air into electricity with by-product heat and water. Unlike an electrochemical battery, in which reactant is regenerated by recharging, a fuel cell does not store energy. As long as a continuous supply of fuel and oxidant is provided, the fuel cell will continue to produce electricity.

Back in 1839, Sir William Grove, "the father of fuel cell" thought that it should be possible to reverse the experiments on the electrolysis of water, by reacting hydrogen with oxygen to generate electricity. The concept of hydrogen fuel cell was thus introduced. In 1889, Ludwig Mond and Charles Langer first used the term "fuel cell" when they attempted to build the first practical device using air and industrial coal gas. In 1932, first successful fuel cell device was revealed from the inventions by engineer Francis Bacon. He improved the expensive platinum catalysts used by Mond and Langer, using a less corrosive alkaline electrolyte and inexpensive nickel electrodes in a hydrogen-oxygen fuel cell [Blomen 1993].

However, the technical challenges were daunting and it was not until 1959 when Bacon and his co-workers were able to demonstrate a practical 5 *kW* fuel cell system capable of powering a welding machine. In October of that same year, Harry Karl Ihrig of Allis-Chalmers Manufacturing Company demonstrated a 20-horsepower fuel cell-powered tractor, which was the first fuel cell vehicle. 1960's can be thought of a glory period of fuel cell application, while the NASA space fuel cells provided electrical power to the spacecraft and enabled men to fly to the moon [Kordesch 1994]. During 1959 to 1982, General Electric developed various Polymer Exchange Membrane (PEM) fuel cells for the Gemini spacecraft and other space applications. The technology was then transferred to UTC-Hamilton Standard and Siemens AG for the air-independent submarine application in mid-1980s.

Ballard Power Systems began to work on PEM fuel cell in 1983 and later became the leader of PEM fuel cell development for transportation applications. Over the years, considerable fundamental research has also been carried out in various academic institutions, including Los Alamos National Laboratory, Texas A&M University and many others. In the last decade, new materials and processes have significantly improved the performance of the PEM fuel cell, making it the most promising among the six types of fuel cells.

In 1993 Ballard Power Systems completed the first North American fuel cell bus using a Ballard PEM fuel cell system. Since then, several smaller PEM fuel cell vehicles have been built in Asia, Europe and North America. The advantage of a fuel cell vehicular engine includes: (1) much higher efficiency; (2) zero emission of any unfavorable combustion by-products other than pure water and heat; (3) trace amounts of NOx and CO and small amounts of evaporated fuel as the only emissions from a fuel cell vehicle, even if hydrocarbon fuel and a reformer are used.

The core of a fuel cell is the electrolyte, which separates the two electrodes. Different electrolytes make the different types of fuel cells. The categories include:

1. <u>Phosphoric acid fuel cell</u> (PAFC), which is directly related to the William Grove's original sulfuric acid fuel cell. PAFC operates at temperature from 150 to 200 °C, and is the only fuel cell technology that is in commercialization use. Most PAFC plants being used are in the 50 to 200 KW range, where large plants with power 1 MW and 5 MW have been built.

2. Molten carbonate fuel cell (MCFC), operated at approximately 650 °C and initially appeared at 1950. The nowadays fuel cell industry Fuel Cell Energy is pursuing its commercialization.

3. Solid oxide fuel cell (SOFC), introduced in 1951, normally operates at temperature over 800 °C. Recently, the intermediate temperature SOFC operating at 550 to 800 °C allows to reduce the cost of materials used for components working at this relatively lower temperature.

4. Alkaline fuel cell (AFC), which initiated by Bacon in the 1930s, provided on-board electric power for the Apollo space vehicle in 1960. This type of fuel cell has been tested under a wide range of temperature, between 30 °C and 240 °C.

5. The low temperature Polymer Exchange Membrane (PEM) fuel cell, originally conceived by William Grubbs in 1959, has attracted more attention in these years.

While a variety of fuel cells are being researched and developed, the three most promising types of fuel cells for vehicular application are PEM fuel cells, phosphoric acid fuel cells, and solid oxide fuel cells. They are also presently considered the most well developed fuel cells. Due to the temperature limitation of the polymer membrane, PEM fuel cell's operational temperature is somewhere between room temperature and 100 °C, which allows quick production of electricity. Meanwhile, the lightweight of PEM fuel cells and system is particularly suitable for the application as movable power plant in vehicles. PEM fuel cell has been considered a technically feasible alternative to internal combustion engines for transportation applications due to its lightweight, low operating temperature and quick start-up. A PEM fuel cell powered vehicle can be quickly refueled and operated on a satisfactory range, to replace the high emission internal combustion engine that caused 60 percent environmental pollution today [Watkins 1994].

Although fuel cells were used and proven in aerospace applications in the past, the use of fuel cells in commercial vehicles has only received attention in the past decade. Fuel cell technology offers an attractive power plant alternative due to its ultra-high energy conversion efficiency and extremely low environmental emission [Binder 1998]. The application of fuel cell technology in vehicles, with inherent high efficiency, high power density and zero-emission potential, has advanced significantly over the past decade, and is now a serious contender for use in zero-emission vehicles. PEM fuel cell has been selected as the main candidate for application on the transportation vehicles.

1.1.2 PEM Fuel Cell and Major Research Issues

Proton exchange membrane (PEM) fuel cell, also called polymer electrolyte membrane fuel cell, has a membrane electrode assembly (MEA), a hydrogen fuel delivery plate and an oxidant air delivery plate, as shown in Figure 1-1 (a). The MEA is made using a polymer membrane electrolyte sheet, sandwiched by two electrodes, an anode and a cathode on each side. Each of the electrodes is coated on one side with a thin layer of catalyst of platinum or platinum alloys. At the anode, hydrogen fuel catalytically dissociates into free electrons and protons (positive hydrogen ions). The free electrons are conducted in the form of usable electric current through the external circuit. The protons migrate through the membrane electrolyte to the cathode side where they combine with the oxygen from air and the electrons from the external circuit to form water and by-product heat. Two grooved fuel cell gas delivery plates are assembled on each side of the MEA to continuously supply hydrogen fuel and oxidant air as well as to propel the by-product water through flow channels on the plates, and to conduct the waste heat to radiation elements.

A single fuel cell does not generate enough electricity to power an electric device, such as the electric drive of a vehicle. Thus many fuel cells are assembled in series to obtain enough high voltage and to provide the amount of electrical power required. A fuel cell stack consists of many series fuel cells as illustrated in Figure 1-1 (b).

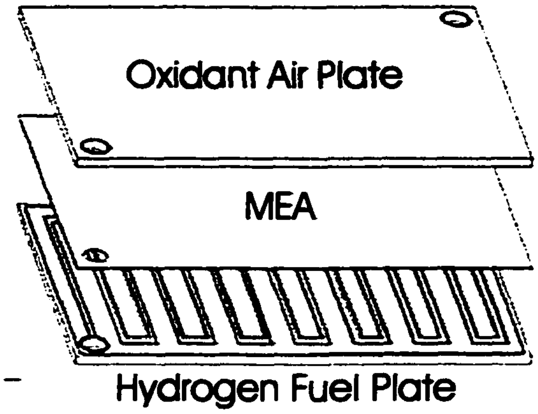

(a) A single PEM fuel cell

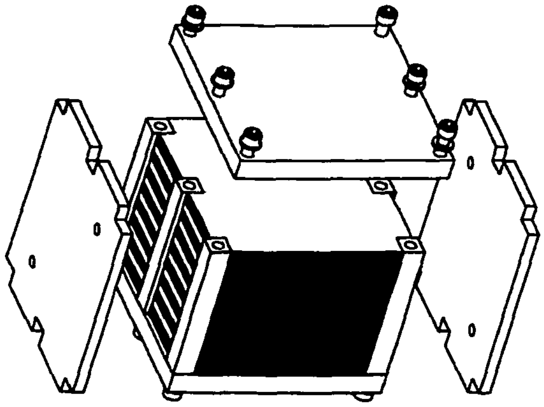

(b) A PEM fuel cell stack

Figure 1-1 A PEM fuel cell and fuel cell stack

The most critical issues facing the transportation fuel cell developers include overall power plant efficiency, interfacing the power plant with the infrastructure of fuel supply, and power plant cost [Plowman 1994]. The cost of fuel cell power plant plays a very significant role on its commercialization. Within the present PEM fuel cell system, which still bears a cost much higher than the commercial target, the fuel cell stack is the current focus for cost reduction. There are three major stack components that contribute to its high cost [Pastula 1997]. Fuel and oxidant delivery plates (or reactant gas delivery plates, flow field plates, and fuel cell plates), electro catalyst, and the proton exchange membrane. At present, they contribute to 25%, 6%, and 27% of the total cost of the fuel cell system, respectively.

In early 1970s, DuPont introduced the Nafion membrane. Since then, many developers use this 50 – 200 micrometer-thick Nafion film as the electrolyte of a PEM fuel cell. However the cost of Nafion membrane and platinum catalyst are quite high and fuel cells requires a specialized environment, with ideal temperature, compression, hydrated oxidant air and hydrogen fuel, to operate efficiently. The combination of these challenges make fuel cells not yet affordable at the marketplace.

The catalyst cost includes platinum material and the process for loading on the polymer membrane. Using platinum as catalyst makes the PEM fuel cell highly sensitive to carbon monoxide (CO). The problem can only be solved while removing CO chemically and physically, and/or increasing the CO tolerance of the fuel cell. The tolerance threshold lies at 10 CO molecules per one million catalytic atoms. A large amount of CO is introduced in reforming various coal fuels to produce the hydrogen, or through the chemical reaction associated with the degradation of the graphite plate materials. The issues of fuel cell plates relating to its high cost and chemical stability will be discussed in next section.

1.1.3 Fuel and Oxidant Delivery Plates of PEM Fuel Cell

The cost of gas delivery plates, which dominate the cost as well as weight and volume of a PEM fuel cell stack, include the cost of material and its fabrication method. At present, the gas delivery plates are made mostly with graphite solid through computer numerical control (CNC) machining, although molding, pressing and many other processes are being developed and tested [Pastula 1997]. The machining method requires slicing, cutting, grinding and polishing, and leads to unreasonably high manufacturing costs.

The cost of a new product normally comes from two areas: development cost and manufacturing cost. Conventional product development is carried out through a trial and error process requiring many design and prototyping iterations [Menon 1998]. The lengthy design lead-time leads to high cost at the early stage of product development. The manufacturing cost of a product primarily depends on its production process, part material and mass production potential. The high cost of fuel cell gas delivery plate relates to all of these aspects.

The new fuel cell gas delivery plate development will consider both development and manufacturing costs as well as fuel cell performance improvement.

1.2 Related Work

This work intends to apply leading-edge design and manufacturing technologies to the development of fuel cell plates. Previous research related to the proposed work and their limitations are discussed in this section. This review helps to understand these technologies and to define the research tasks for extending these technologies for the proposed application.

1.2.1 Fuel Cell Gas Delivery Plate Manufacturing

At present most fuel cell companies, such as Ballard Power Systems, use high-density graphite solid to produce gas delivery plates. These plates are sliced from graphite blocks, milled using CNC machines with desired flow channel patterns and grinded under high tolerance to achieve good contact. Even though the manufacturing technique used is mature, the high accuracy requirements and poor machinability of the graphite material lead to a high cost, time consuming and labor intensive process.

The difficulty and the high cost of the current fuel cell delivery plate manufacturing come from the characteristics of solid graphite material. Manufacturing cost reduction is considered with development of new materials such as embossed, laminated and stamped materials [Wilkinson 1997]. Some other options in plate manufacturing including close molding, injection molding, and pressing of either graphite foils or graphite particles and a binder have been considered as alternatives. Molding methods impose manufacturing challenges on the fine flow channels and thin plate thickness, and much research still needs to be done. Foil pressing was found to cause poor cross plate conductivity that is desired by fuel cell application. Both molding and particle pressing also face the problem on the die release and die occupancy during material solidification and structure formation.

1.2.2 Fuel Cell Plate Structure and Thermal Issues

Fuel cell plate structure is an important issue relating to weight, geometry, material performance, loading and other structure responses. When using solid graphite as the only plate material, the structure response is not very significant with normal structure loads and 80°C temperature load during PEM fuel cell operation. If considering alternative materials, such as composites for the fuel cell plate, or applying different layer materials, the structure issue becomes more complex. The challenge is similar to those in the smart layer structure [Benjeddou 1999] or electronic packaging interconnection [Polycarpou 1997]. For these cases, structure effects such as thermal stress, stiffness, and through-thickness electric potential need to be considered. Therefore, the structure issues on the fuel cell plate are material dependant.

As an energy system, thermal issue directly relates to the efficiency of fuel cell systems. The heat balance includes the thermal effect on fuel cell stacks, fuel cell cooling panels, fuel cell gas plates, and other fuel cell components that need power supply [Kratschmar 2001]. In most conditions, the heat source is from the ohmic heat generation and electrochemical reaction [Dong 2001]. The heat sources and heat transfer coefficients may need to be determined through certain numerical and experimental studies [Abou khachfe 2001].

1.2.3 Fuel Cell Flow Field Design and CFD Analysis

The efficiency of a single PEM fuel cell is affected by membrane, catalyst, and flow channel of gas delivery plates. The function of the fuel cell gas delivery plates is to distribute fuel and oxidant gases to the MEA through flow field channels embossed on the plates. Analytical model can predict the performance of a hydrogen/air PEM fuel cell electrode under various operating conditions, including pressurization, stoichiometry changes and oxygen enrichment [Boyer 1998]. Experimental results show large deviations due to technical limitation for measuring millimeter sized flow field [Pastula 1997].

The flow field plate design is an integral part of fuel cell design, which includes consideration on mass transfer issues, water management, water removal, temperature gradient, pressure drop, etc. [Pastula 1997]. Study on flow fields has been carried out at leading fuel cell companies such as Ballard Power Systems for many years [Watkins 1992; Kaskimies 1999]. Water management and removal in the flow channels are important issues on high efficiency fuel cell operation [Voss 1995; Wetton 1999]. Numerical study indicates that the oxygen reaction rate influences the current density and the flow configurations affect the performance [Singh 1999].

Flow field channel structure geometry directly affects the fuel cell efficiency. The flow field plates with parallel straight channels, single serpentine channels, discontinuous channels and spiral channels with high and low air Stoichiometries have been simulated with CFD models on the flow channel configurations of the PEM fuel cell cathode [Kaskimies 1999]. The current-voltage measurements in different operating conditions, using different channel geometries were applied as verification of the CFD models. Current density distribution was modeled with fixed geometry, such as very narrow and low channels 2 *mm* wide and 2 *mm* deep serpentine and spiral channels. More even distribution of oxygen in the air to the whole cathode active area was found an effective mean to obtain high efficiency design. These CFD models could be used on both hydrogen and oxygen channels [Weisbrod 1996].

In the study carried out at University of Victoria, numerical simulation was applied to predict the status of gas flow in the flow channel. The effect of microstructures on oxygen enhancement at the air to MEA interface within the air channel was considered to enhance the fuel cell efficiency [Lu etc. 1998, Dong etc. 1998]. The performance improvement introduced by various oxygen enhancing structures needs to be further studied and verified through comparative cell tests.

1.2.4 Fuel Cell Plate Fabrication Using Screen Printing Technology

The demand for low-cost components in the rapidly growing fuel cell market needs mass-production techniques based on advanced materials. Meanwhile, long lifetime associated with the low costs is also a prerequisite for the commercialization of these products. Low-cost graphite solid needs a lengthy fabrication process, leading to costly plates. Broad materials based on related manufacturing methods are being developed and material development will dictate the success of cost reduction of fuel cell plate fabrication.

Fuel cell plates support electrodes, contain gas delivery flow field and form the stack. They also need to have high electrical conductivity to collect the current and high corrosion resistance to ensure prolonged operation. Highly conductive and low-cost metals such as stainless steel have less corrosion stability than that of carbon-based components by a factor of 1000. In fact, only special high-cost metal materials, e.g. gold have the sufficient corrosion resistance that is achieved by graphite materials.

The conductivity, indolence and strength requirements of PEM fuel cell plates suggest carbon, graphite and certain indolent metals as potential materials for the fuel cell gas delivery plate [Ronne 1995]. Conductive polymers with their main industry applications on the micro-electronic with thin film technology provide a good alternative. The relatively high cost and poor mechanical performance of conductive polymer is the key obstacle for a broad and direct application. Composite materials show flexible processing and good performance potential in the fuel cell plates. Most low-cost composite materials with polymer matrix are not electronically conductive, even if some conductive fillers are used as reinforcement.

From fuel cell electrochemistry point of view, electrical conduction in a fuel cell is achieved through electronic and ionic conductions [Oldham 1994]. All metals are (free) electron conductive, except a few high cost noble metals. Earlier research found that most metallic fuel cell bipolar plates are corroded to release metallic ions [Mallant 1994]. These ions poison the electrolyte or the catalyst in the MEA by exchanging with proton in the fuel cell environment, leading to degradation of fuel cell performance.

When considering the strength of the fuel cell plate, the high porosity that reducing the plate structure performance will benefit the fuel cell efficiency because of the gas mixing effect. The plate with non-resin-impregnated graphite had good conductivity but the hydrogen leaked out through the graphite [Kaskimies 1999]. The leaking can be solved through impregnating the plates with resin. However, the conductivity of the composites, e.g. graphite-polypropene was not satisfied enough. In fact, the work for finding a low cost and efficient substitute materials on the fuel cell plate has been going on for many years, with no success. Fuel cell plate material development based on new manufacturing process has not been well studied.

A low-cost, flow field plate manufacturing method using screen-printing has been introduced at University of Victoria [Dong 1999a, Perry 1997]. Screen-printing, as a two-dimensional fabrication technique, is widely used in garment printing and integrated circuit production. Dong's group is the first one to invest screen-printing in the three-dimensional (3D), 0.7~2 *mm* thickness fabrication of fuel cell gas delivery plate. The technique applies liquid phase conductive materials and the add-on process to build the 3D structure layer by layer. The method is similar to the rapid prototyping technique, which have been widely used to carry out design verification in product development. The material development proposed in this study is associated with the new screen-printing based fuel cell gas delivery plate manufacturing technique.

1.2.5 Conductive Polymer and Conductive Polymer Composites

Polymers that repeat their structure regularly in long chains and networks with molecules, unlike metals, do not conduct electricity, and are used as insulators. For a polymer to be able to conduct electric current it must consist of single and double bonds alternately between the carbon atoms, and/or also be "doped", which means that electrons are removed through oxidation or introduced through reduction. These "holes" or extra electrons can move along the molecule, therefore it becomes electrically conductive. This characteristics is found at late of the 1970s by Alan J. Heeger from University of California at Santa Barbara, Alan G. MacDiarmid from University of Pennsylvania, and Hideki Shirakawa from University of Tsukuba. Year 2000 Nobel Prize in Chemistry was awarded to these three researchers for their jointly discovery and development of conductive polymers.

The conductive polymer has also yielded important practical applications. They have been used in industries and are developed for anti-static substances for photographic film, shields for computer screen against electromagnetic radiation and for "smart" windows that can exclude sunlight. In addition, semi-conductive polymers have recently been developed in light-emitting diodes, solar cells and as displays in mobile telephones and mini-format television screens. At present, the most widely used and well-developed conductive polymers include polyacetylenes (PAC), polypyrrole (PPY), polyaniline (PANI), polythiophene (PT), polyparaphenol (PPPH), polyphenylenviny (PPHV), etc. [Gul 1996].

Some researchers have begun to investigate the conductive polymer composites on applications of electronic devices [Gul 1996]. In fuel cell gas delivery plates, people are testing low-cost conductive polymer composites as substitute of present high cost fuel cell plate. Ledjeff-Hey used the 30 *wt%* carbon black to modify the polypropylene to get the conductivity of 2.5 *S/cm* [Ledjeff-Hey 1998]. The break elongation and tensile strength of this thermoplastic composite have reached over 3 *%* and 20 *MPa*, respectively. Busick investigated a thermosetting graphite composite, Graphite/Vinyl

Ester for making the bipolar plate [Busick 1998]. The composite can get conductivity over 100 *S/cm* at 68 *wt%* graphite and perfect test result in a single cell operation. Both methods focused on the molding process with a relatively long fabrication time. The Busick's approach also needed further machining to produce the final plate form. Both Ledjeff-Hey and Busick's approaches are concentrated on directly applying new conductive materials to form the fuel cell plates.

1.2.6 Virtual Prototyping and Rapid Prototyping

Prototyping includes the production of the design prototypes and various tests to be carried out on the prototypes to identify the flaws, limitations, and advantage of the design under working conditions. Virtual prototyping (VP) technique uses computer model to replace the physical prototype and the analyses/simulation using the computer model to replace the various tests required in a physical prototyping process. The technique starts with a complex, parametric, solid model of the mechanical design that is generated using a professional CAD system, such as Pro/ENGINEER from Parametric Technology Company (PTC). The integrated analysis tasks are carried using finite elements analysis tools, either by a stand-alone system such as ANSYS, or the built-in CAE program, such as Pro/MECHANICA in Pro/ENGINEER. At early 1999, PTC and ANSYS Co. started cooperation on their interface development between CAD and finite element [PTC web]. This joint development led to design tools that formulate virtual prototyping applications [Chang 1999]. Many finite element analysis packages that were originally developed for structure analysis have been extended to carry out other applications, such as thermal, computation fluid dynamics and electromagnetic analysis [ANSYS 2000]. Design optimization and manufacturing functions are also found in these design and analysis tools [Yang, 1999].

Due to their short life, most of these new tools have not yet been fully tested in an integrated model. The development of the method to build an adequate computer model and to effectively apply the finite element analysis tool for various design performance analyses for virtual prototyping and design optimization is still a major technical challenge. In addition, at present a significant portion of part performance can only be accurately modeled and analyzed using mathematical model and computer simulation, such as gas flow conditions. For most analysis tools, the method to effectively incorporate computer simulations into the design optimization is also to be developed.

Rapid Prototyping (RP), which appeared in mid-1980s, is a technique that could convert a design from a CAD model directly into solid objects within hours without human intervention [Schaub 1998; Chua 1997]. The technique utilizes layered manufacturing method, by which parts are built layer by layer. With this layered method, the relatively complex geometry can be made [Schaub 1998]. Even though the construction of the prototype is straight forward, the development of prototyping materials is quite challenge and blocks the RP development [Ashley 1998]. In recent years, research on the RP development has switched to focus on the use of final part materials instead of some types of model materials [Ashley 1998; Dong 1999a]. Throughout RP development, the material issue still predominates.

Layered manufacturing along with materials study can be integrated with the structure analysis and material processing of the parts [Cham 1999]. Manufacturability study on rapid prototyping involves considerations on material processing, costs, tooling, cycle time, and sometimes tolerance [Vliet 1999; Armi 1999]. The computer aided design and engineering (CAD/CAE) tools are also used for manufacturing studies through CAD models and finite element analysis [Vliet 1999]. The finite element analysis plays a key role on RP through virtual prototyping. In addition, virtual prototyping has more flexibility on materials design and selection due to unlimited material availability.

1.2.7 CAE and Design Optimization

Virtual prototyping is an emerging technique that rooted from a more general technique, Computer-Aided Engineering (CAE). Computer-Aided Engineering, which generates design models using a CAD package and uses the models to analyze a design, is not new to engineering applications. However, the rapid development of computer hardware and professional CAD/CAE tools made design and analysis of complex mechanical design feasible. These progresses facilitated the virtual prototyping technique that applies complex computer models to carry out analysis, simulations and heuristic evaluations of a designed product as if on a physical prototype [Wang, 1999]. These virtual prototypes give the quantitative evaluation on the design [Chang, 1999], and provide the technique that supports cross functional teams for evaluation of product performance, reliability, and manufacturing costs at the early stage of product development. The approach is also able to conduct quantitative trade-off through design optimization for design decision making.

In structure design, geometric parameters, material volume and weight are often used as design variables while optimization programs are used to identify the design optimum [Fleury 1979]. Most structure design can only be carried out through indirect performance function evaluations and global optimization since there exists no clear analytical relation between design variables and optimization functions, and the design functions tend to have illed shape for optimization search [Wang 1999]. The sensitivity of design variables to the design function determines the role of each variable for the design under certain structure loads [Ohsaki 1998]. The constraints of the optimization are formulated with loading constraints, boundary conditions, as well as geometry and materials requirements [Li 1998].

Today structure design optimization problems are often evaluated using linear finite element analysis and formulated using linear empirical constraints [Patnaik 1998]. But most structures and materials present nonlinear behaviors requiring nonlinear analysis [Liu 1999]. Analysis methods with nonlinear modeling capability and more accurate constraint definition for design optimization become necessary, especially to uncertainty loading condition [Li 1998; Liu 1999; Chang 1999].

A more quantitative optimization method, which eliminates the empirical constraint definition, called anti-optimization, has been used on the structure design [Qiu 1998].

The method applies a two-step optimization algorithm, which optimize both objective and constraint functions. The advantage of this method is that it can solve the problem under any uncertain loading conditions. The key issue in the structure anti-optimization is the constraint definition [Lombardi 1998].

Design optimization based on fluid dynamic simulation can be used to identify the optimal part geometry, fluid parameters, velocity, temperature, pressure or even grid refinement and convergence rate. Today commercial engineering codes for computational fluid dynamic (CFD), such as CFX and Fluent, are widely used. However, due to the complexity of the mathematical models and the extensive computation process of CFD, design optimization has not yet been incorporated into these commercial packages. Application of design optimization is still limited to specific CFD applications [Zapach 1991]. At present, flow dynamics simulation only serves as a method to model and evaluate the functional performances of fuel cell plates and flow fields. Using a commercial CFD tool to automatically optimize key design parameters of the fuel cell gas delivery plates and flow fields is still an untouched field.

1.3 Proposed Approach

This research investigates the rapid prototype development techniques for fuel cell gas delivery plates to replace the traditionally high cost fuel cell plate development method. The study covers both of the virtual prototyping and physical prototyping aspects of the plate development, which relates to many issues discussed in the last subsection. Specifically, the research is to be carried out in the areas of rapid product development, prototype/batch plate manufacturing, virtual prototyping of plates, and virtual prototyping-based plate optimization.

1.3.1 Rapid Product Development

To reduce design lead time and lower manufacturing costs for producing fuel cell plate, a material adding, instead of subtracting method for building complex geometry is applied in this work. Computer modeling and simulation on thermal, structure and fluid analysis form the plate virtual prototyping method. The physical prototyping method is based on the layer deposition technique through screen printing as well as ink materials development. Both virtual prototyping and physical prototyping methods follow the concurrent engineering approach, and apply parallel developments on design optimization and material development.

1.3.2 Prototype and Batch Production Plate Manufacturing

A prototype is a test model used for the verification of a concept design. Batch production is a method of production where one operation is completed on a number of units of the product, before they are passed on to the next stage of the process and/or mass production.

Compared to most traditional product development, which follows the material development maturity, this study combines the composite material development with fuel cell plate prototype development. Since the screen printing manufacturing method is one, which can be applied on the batch production as well as the mass production potential, the research task is aimed to improve the methodology on manufacturing and product development for either fuel cell plate or other mechanical components. Both the plate design and composite material development are carried out to inherit the manufacturing scalability of the patented screen-printed fuel cell plate manufacturing technique.

1.3.3 Virtual Prototyping Method

Development of fuel cell technology needs considerations from multiple disciplines, including electrochemistry, materials science, mechanical and electrical engineering. The proposed virtual prototyping technique for concurrent and rapid product development incorporate modeling and analysis from three related areas: structure, thermal and fluid dynamics for the development of fuel cell gas delivery plates. These tasks are performed using commercial design and analysis codes Pro/ENGINEER, Pro/MECHNICA, ANSYS, and CFX as well as dedicated research programs.

The parametric CAD tool, Pro/ENGINEER, is used to model the layer structure of the flow channel. The model is formed following the screen-printing layer building process with a solid substrate and building layer. The model is to be used for structure integrity and thermal analysis using finite elements method. The geometry formed by the layer structure is to be used to form CFD codes for flow-field flow condition analysis, particularly the oxygen level of the compressed air at the air channel and MEA interface. The parametric model supports performance analysis and allows design optimization to be carried out on the plate structure and flow field. It provides quick feedbacks and optimal configuration to a new fuel cell fuel and oxidant delivery plate.

The purpose of thermal finite element analysis on the wall structure and channel is to verify the temperature distribution in the plate to avoid over-heated hot spot on the MEA, which is a common failure mode of PEM fuel cells. The convection effect of wall model and fluid model is simulated through thermal analysis conducted with boundary conditions. The finite element analysis tool in ANSYS is used for this simulation. Due to the complexity of the problem, this analysis decouples its inter-related aspects, focuses on one aspect each time, and discusses the potential side effects. Specifically, the temperature field from the convection computation is not used in structure analysis and the wall convection effect is not combined with fluid convection effect.

The purpose of structure analysis is to simulate the structure response under certain loading conditions (pressure and temperature) and to optimize the plate structure. The stress analysis FEA calculation is performed using the solid CAD model and commercial FEA code. The solid model of the plate is first generated using the Pro/ENGINEER CAD system. The model is then passed to FEA tools, including Pro/MECHANICA and ANSYS. The advantage of Pro/MECHANICA lies on its full integration with the Pro/ENGINEER system, while its main limitation is its limited capability of handing only linear structure problems. ANSYS can carry out nonlinear structure analysis through an interface to the Pro/ENGINEER system. Nonlinear structure analysis is carried out by modifying the Pro/ENGINEER input file and adding nonlinear stress-strain relation on the material properties through appropriate commands.

Flow field analysis using CFD models predicts fuel cell performance for given flow-field and printed layer design. The method is used to monitor pressure drop and oxygen content along the MEA-channel interface. These are the two major design factors of PEM fuel cell flow-field. The former was patented by Ballard Power Systems [Watkins 1992]. The later was introduced in our earlier study [Dong 1998]. Fuel cell performance is enhanced by adding blocks with different geometry at certain interval in the flow channels of the air delivery plate. Due to these blocks, air flow along the blocked channel forms vortex, which increases the oxygen concentration at the MEA surface [Lu 1998]. This phenomenon is predicted using CFD simulation with commercial CFX codes. Results of the simulation are used in the flow-field design optimization.

1.3.4 Virtual Prototype Based Design Optimization

Design optimization of fuel cell plates includes flow channel layout, plate structure and their main parameters. The fuel cell gas flow channel design covers both topology and geometry. The design objectives include: maximizing active area; minimizing the potential of by-pass; achieving ideal pressure drop; delivering maximum amount of oxygen; and minimizing electric resistance, thus to achieve the best fuel cell performance. Many design requirements such as satisfactory of strength integrity under various structure and thermal loads are to be satisfied as design constraints.

The objective and constraint functions in design optimization, or in short optimization functions, are evaluated using finite element and finite volume analyses, which may contain multi-minima and discrete values. The optimization thus has to be carried out using a special optimization tool. The built-in optimization routines of Pro/ENGINEER and ANSYS are applied to the structure and thermal integrity. The optimization tool based upon the recursive quadratic programming method is integrated to the CFX code during CFD simulation. The optimization is aimed at providing best design solution based on the quantitative results from the virtual prototyping.

Chapter 2. Prototype and Batch Production Methods for PEM Fuel Cell Gas Delivery Plates

2.1 Layer Deposition Approach

Layer deposition is a technique widely used for the deposition of thin films in the electronic industries. The technique applies chemical or physical vapor deposition, sputtering, and/or physical printing. The processes involve chemical reaction, mechanical bonding, sintering as well as any method in electronic packaging. The materials used in the deposition include metals, ceramics, polymers, and their composites.

Screen printing, as a layer deposition technique, is also used in electronic industries. While using this method as prototype and batch production in fuel cell gas delivery plate, it has the characteristics of similar mass production method used in electronic industries. Screen printing for fuel cell plate manufacturing provide a low cost, alternative manufacturing method for producing fuel cell plates.

Layer deposition has flexibility on building complex geometry, which is hard to achieve with traditional cutting machining process. Identical to the production of electronic circuit, the layer deposition method on fuel cell plate manufacturing also includes the process of chemical reaction, mechanical bonding, etc. Based on the fuel cell operation and process cost requirements, only polymer and polymer-based composites are considered in this study.

2.2 Advanced Plate Materials

Fuel cell plate materials are subjected to the fuel cell operation requirements. The cell is based on a Proton-Exchange-Membrane (PEM) sandwiched between two electrodes, the anode and cathode, consisting of platinum (catalyst) supported on a carbon fiber sheet electrode support. At the anode, hydrogen (H_2) is separated into protons (H^+) and electrons (e^-). The protons diffuse through the membrane while the electron current, travels via an external circuit to the cathode. There, they split air oxygen molecules (O_2) and the resulting species (O^{2-}) combines with the diffused protons to form water (H_2O). To provide an efficient passage for the electric current through the entire stack and to separate both gases of the individual fuel cells, graphite-based bipolar plates are utilized.

From pure cost consideration, graphite, metal, most ceramics and polymers as well as their composites are potential candidates for the application. Almost every catalogue group has been tested with certain types of fuel cell. Considering the PEM fuel cell performance, corrosion resistance to above molecules and ions, such as H^+, O_2, and H_2O, limits most metals applications. Since elemental metals are easily corroded by the proton except some high-cost noble metals, directly application with metallic materials is impossible. Only ceramics, polymers, and their composites are able to serve as substitution to the graphite solid for the fuel cell plates. In short, the materials used on the fuel cell gas delivery plate needs to be electrical conductive, mechanically and fuel cell electrochemistry suitable.

2.2.1 Screening Printing Ink Material Alternatives and Conductive Polymer Composite Materials

The success of layer deposition fuel cell plate manufacturing technique highly relies on the materials used in the deposition. An industrial poster ink, which has good printability and satisfactory conductivity, was used to produce functional fuel cell plates [Petty 1998]. However, these printed plates have been found unstable in prolonged use during the fuel cell operation. Efforts are devoted in this research to investigate the cause of the problem, and based on this acceptable composition to develop new, more suitable composite materials specifically for the fuel cell plate layer deposition manufacturing process.

With the screen printing layer deposition method, the composite materials are applied in liquid form and "dried" under certain conditions to solidify and to form the flow channels. Polymers and polymer-based composites can be based on either thermoplastic or thermosetting polymers to achieve this "forming" process. Thermoplastic polymers are high molecular weight, linear or branched polymers, which are either crystalline or amorphous, depending on their chemical compositions. These polymers need to be heated to their glass transition temperature, T_g, or melting point, to be the liquid form. Thermosetting polymers are typically low molecular weight polymers that go through major chemical and physical changes during material processing. The thermosetting polymers can react either at room, or elevated temperatures, with or without catalysts to form a cross-linked network formation, that is a relatively stable form. Any polymer or polymer-based composite is sensitive to temperature. The most traditional polymers and polymer composites are insulators, which cannot be used to make fuel cell plates.

To satisfy the mechanical requirements, electrical conductivity, and fuel cell electrochemistry stability, conductive polymer composites are developed in this work to form the flow channels of the screen-printed PEM fuel cell gas delivery plates.

To develop the polymer-based composites, the non-conductive nature of the polymer matrix phase needs to be modified to allow the final composite materials to possess certain level of conductivity. Traditional method is to apply graphite or metal reinforcement phase to a significant loading level. However, this approach has inherent limitations. The high ratio of conductive solids added to the composite considerably reduces the fluidity of the composite, reducing the printability of the composite ink for screen-printing.

In this work, conductive polymer is used as additional phase to modify the non-conductive polymer matrix for the printed flow field of the fuel cell plate. Applications of conductive polymers as function materials individually or combined with other polymer have been used. The weak bonding nature of the conductive polymers, however, limits their application as a structure material. Certain strong bonding polymer, like epoxy, is used as the original binder, while conductive polymer is used as modifier to form a new conductive binder to overcome the structure weakness. The resulting composite binder has better conductivity, comparing to epoxy, and better bonding effect, comparing to conductive polymer phase. Conductive solids, like graphite powder (or sometimes combined with metal powder), are later added to form the final conductive polymer composites for the flow channels of the printed plates.

In short, the conductive polymer is used as modifier phase to provide and improve conductivity, epoxy serves as a matrix phase to provide binder performance, and solid graphite is added as reinforcement phase as well as conductivity improvement ingredients. The composition and forming process of the final composites depend on the balance between the three phases and fuel cell operation condition and requirements. This study concentrates on the feasibility of this type of materials to support the new layer deposition technique for fuel cell plate manufacturing.

2.2.2 Selection of Conductive Polymer Additions

Among the three major ingredients of conductive composite materials, the selection of appropriate materials for making conductive polymer composites for fuel cell plates is based on the nature of material conduction. The conduction method between free electron conduction and ionic conduction is called π electron conduction. The presently used solid graphite material of fuel cell belongs to this category. π electron is formed through the conjugate bond (called π bond) change along the molecule chain. Similar phenomenon happens in the semiconductor with electron or hole moving at certain direction [Oldham 1994]. Intrinsic conductive polymers show the conduction through π electron or sometimes called soliton [Hummel 1985c]. Many literatures have shown the ionic conductive materials influence the fuel cell performance [Scholta 1997, Wilkinson 1997]. The stabilities of ionic conductive or non-ionic conductive bipolar plate materials have been examined with Scanning Electron Microscopy (SEM) and Energy Dispersion X-ray (EDX) [Scholta 1997, Mallant 1994] to find mechanical damage and ionic influence caused by electrochemistry corrosion under fuel cell environment. This study will select non-ionic conductive materials as candidates for fuel cell plate.

Graphite particle is the key ingredient in the composition in order to get good conductivity and through bonding effect to reach ideal mechanical performance. It has solid resistivity of 0.34 *ohm-cm*, thus being used in every composition for making composite materials for fuel cell plates. Based on the accepted understanding on the mechanism of electrically conductive polymer composites, the electric conduction is achieved by the direct contact of electrically conductive filler particles and/or charges passing by a tunneling mechanism. This study only discusses the combined effect without detail analysis on the two mechanisms. According to the previous studies, graphite particle size with ranges of $75<d<150$ μm and $53<d<75$ μm in poster ink are adequate for screen-printing in making ideal conductivity plates. Thus this study still selects the $75<d<150$ μm graphite particle to make conductive polymer composites for fuel cell plates.

2.2.3 Forming Process of Composite Materials for Fuel Cell Plate

In order to produce accurate and repeatable sample of high quality, a new close mold, which accommodates the mixed component materials together, is designed. The design supports the conductivity test associated with consideration of screen-printing material requirement. Thin sample coupons of 28.57 *mm* diameter and 1 *mm* thickness are made to fit the conductivity test set-up. Meanwhile the screen-printing technique requires the materials forming from liquid phase to solid phase without applying high pressure.

Accordingly the close mold is designed with a chamber, forming a low compressive environment to ensure no air pockets or other curing deformities produced.

The aluminum mold includes a mold plate, base plate, top plate and locking coupon, which show in Figure 2-1 (a). The mold plate that is bolted to the base plate contains a two-stage sample chamber. Liquid sample material is poured into the first stage of the chamber, which is precision machined to meet diameter and thickness constraints. The locking coupon is then placed in the second stage of the chamber to provide the second sealing face. The locking coupon is slightly deeper than the second stage of the chamber, ensuring that it sits higher than the mold plate surface. The top plate, not showing in Figure 2-1 (a) is then placed on top of the locking coupon and bolted to the base plate. The compressive pressure from the bolts is transferred through the top plate to the locking coupon. This ensures an even pressure distribution to the sample as it cures.

Once the sample has cured, the mold is unbolted and a hex screw is threaded into the top of the locking coupon. This allows the coupon to be removed while simultaneously pulling the base plate from the mold plate. The sample can then be easily accessed from both sides and removed without damage. Figure 2-1 (b) shows the assembled mold with no compressive top plate.

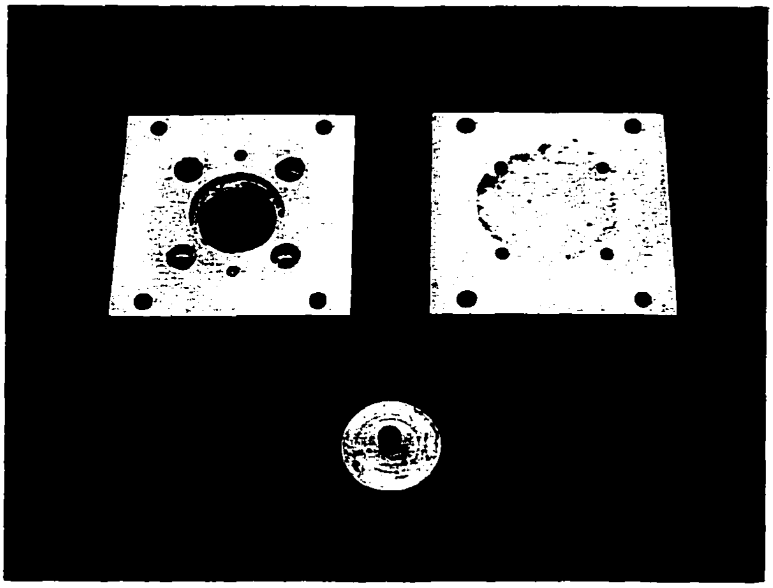

(a) Mold components

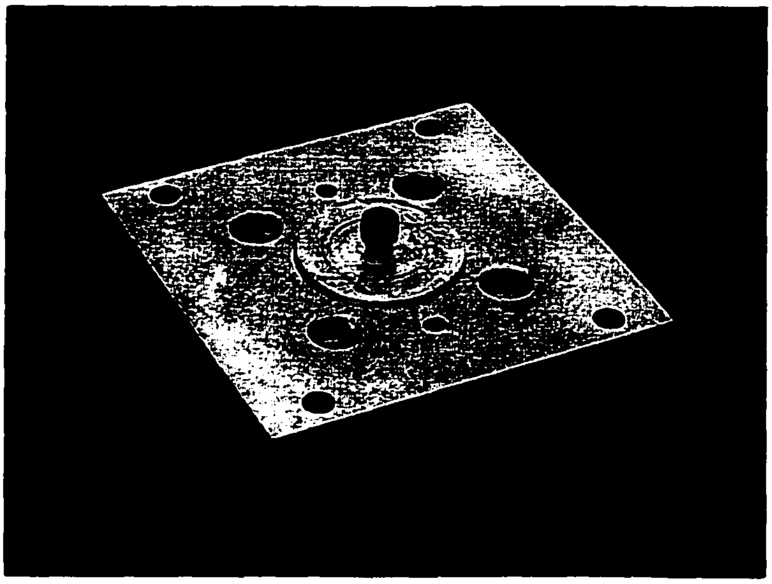

(b) Fully assembled mold

Figure 2-1 Mold for test samples

The composition of conductive composites used in this study is discussed in following sections. These compositions and considerations do not cover all of the composite development work for the screen-printing technique. Associated material development is used to prove the feasibility of screen-printing layer deposition manufacturing technique.

(1) Water based poster ink/graphite

Water based poster ink/graphite was the first developed ink material for screen printing layer deposition technique on fuel cell plate. The plate made by this composite ink had good electrical conductivity similar to graphite particle, but had serious MEA contamination after fuel cell operation [Kratschmar 1997]. This ink composition is used as reference for the new conductive polymer composite ink material development.

(2) Graphite/ConductiveLacquer(Polyaniline)/Epoxy, or Graphite/Polyaniline/Epoxy

Polyaniline as one of widely used conductive polymer materials is formed through polymerization of aniline monomer. Polymerization of in situ aniline with the formation of insoluble polyaniline is accompanied by sedimentation of copolymeric latex with formation of macroscopic composites. This causes the dispersion difficulty of mixing the polyaniline with other materials such as graphite and epoxy [Wessling 1998]. To overcome this problem, a "metallic form" polyaniline derivative, called polyphenyeneamine as shown in Figure 2-2, made by ORMECON® of Germany, is used. This polymer is dispersed with solvent to get commercial lacquer product.

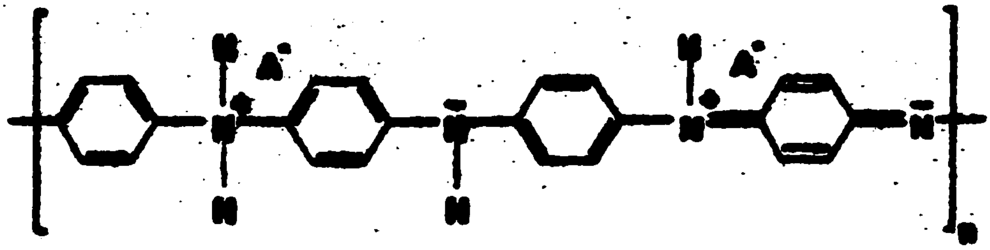

Figure 2-2 Polyphenyleneamine, green metal form (from ORMECON manu)

Epoxy is a mature polymer material, which has over 100 commercial products. The pre-polymerized epoxy resin is started by initiator to begin polymerization. There are three types of initiators: amine hardener, acid hardener and light source curing. Light source curing is to use light to initiate the polymerization, and the epoxy resin then cures itself. UV light is widely used in electronic industries for epoxy curing. The normal UV light exposure time with 100 ~ 500 W/cm^2 power density is about a few seconds.

Acid hardener needs temperature at least 100 ^oC, normally above 150 ^oC, to make the epoxy curing. The lacquer products used in this study have a limitation of 120 ^oC for processing and application, which make acid hardener not applicable. Amine hardener is very popular in epoxy application, which can be processed under from low temperature (below 0 ^oC) to high temperature (above 800 ^oC). This study uses the amine hardener at room temperature or elevated temperature below 100 ^oC to make Graphite/Conductive Lacquer(Polyaniline)/Epoxy, or shortly Graphite/Polyaniline/Epoxy composites.

One of the key mechanisms for polyaniline (or polyphenyleneamine) lacquer conductivity is the π bond in the polymer chain. This phase can exist only under acid phenomenon. The amine in the epoxy hardener can deteriorate this state to turn the polyphenyleneamine into non-conductive polyaniline. To avoid this situation, the amine hardener is mixed with pre-polymerized epoxy resin first, and then added the polyphenyleneamine lacquer. This process can let the amine hardener partially cross-link with epoxy resin and neutralize the alkalinity of amine hardener to minimize the lacquer's conductivity loss. Thorough mixing is necessary to ensure proper dispersion of the lacquer within the epoxy to form a uniform ink binder.

Once the ink binder has been prepared, graphite particles are added. It is recommended that small amount of graphite be gradually added and then mixed to avoid over-saturating the mixture too quickly. The reason that causes this over-saturation is unclear. Surface tension that influences the mixture's viscosity might be a reason.

(3) Graphite/SilverEpoxy/Epoxy;

Silver epoxy, one of the widely used conductive polymers in electronic industries, is also considered as a modifier for making the conductive polymer composite. The epoxy resin is applied as a binder phase.

(4) Graphite/SilverEpoxy/PosterInk;

Since the poster ink was used successfully in exploring the feasibility of the screen printing fuel cell plate manufacturing technique, the Graphite/SilverEpoxy/PosterInk is selected as a reference in the development of silver epoxy based conductive polymer composites.

2.3 Identification of Ideal Composite Composition

Application of composite materials for making fuel cell plates through the screen-printing layer deposition technique is a challenging task due to the complex material requirements of the plate and the printing process. These include viscosity, electric resistivity/conductivity, mechanical properties, heat transfer thermal properties, curing procedure, and fuel cell electrochemical stability. All these requirements are satisfied by the proper selection of composite ingredients and the optimal fraction of each ingredient in the composition.

2.3.1 Viscosity

The viscosity of ink materials is critical to the screen-printing process, since the printable composite material requires liquid phase in printing and curing/drying to form solid phase through certain procedure. Previous study at our Fuel Cell Lab in University of Victoria found that the approximate viscosity of 25000 cp is suitable to the screen-printing process [Kratschmar 1997]. This viscosity is determined by the viscosities of liquid ingredients, as well as the size and amount of solid graphite particles. In this composite material development, the stated suitable viscosity is targeted.

2.3.2 Electric Resistivity/Conductivity

Electric resistivity of composite materials is a key consideration for fuel cell plate application. The resistivity is determined by the bulk resistance of composite ingredients, surface contact resistivity, and environmental temperature.

Normally, the contact resistivity is much higher than the bulk resistivity of the plate material, and is quite different between contact surfaces of an experimental setup and those between fuel cell plates. For simplification, this study only considers the overall resistivity, trying to eliminate the influence of contact resistance by applying a high compression on the experimental setup. Meanwhile, all resistivity tests are carried out at room temperature, ignoring the difference with elevated fuel cell operation temperature. Only material composition with acceptable resistivity is kept in further investigation.

2.3.3 Mechanical Properties

Mechanical properties of the plate materials directly relate to the lifetime of the fuel cell plate. These properties include any characteristics that influence the load and deformation as well as their relation. The key properties for an early stage material investigation cover stiffness or Young's modulus, yield stress, strength, max elongation or displacement, thermal expansion coefficient, etc. and their temperature dependent values. They determine whether the material is working at the conditions of elasticity, plasticity, viscoelasticity, fatigue, or creep. Stress, displacement and stiffness can be measured with material testers such as a MTS machine, while their temperature related performance and viscoelastic properties are determined by dynamic mechanical analysis (DMA) method. The thermal expansion coefficient is measured using thermal mechanical analyzer (TMA) by monitoring the sample dimensional change as a function of temperature. When using composites as plate materials, the bonding effect between different phases, called interface performance, influence all these stated mechanical properties.

The interface performance of the composite materials is studied through microstructure observation using scanning electron microscope (SEM) on damaged or non-damaged samples. The SEM investigation in this study provides the information for evaluating the mechanical properties of composite ink materials after drying. It should be noted that the SEM microstructure investigation is only used as the first step in mechanical performance evaluation. The fully development of composite in materials for fuel cell plate should follow the whole required mechanical property study based on ASTM or ASME testing standard, combined with the SEM microstructure investigation to modify the material processing method.

Good interface bonding, shown as good fiber coverage by resin or adhesion, relates to good mechanical properties, indicating that the material can be used for further investigation such as fuel cell operation test. Bad interface bonding indicates that the material needs to be modified through composition process, such as additional adhesion or even fiber treatment. At most cases, the bonding effect investigation using SEM microstructure examination can provide information for the mechanical property evaluation of fuel cell plate materials.

2.3.4 Thermal Properties

The thermal properties of fuel cell directly determine its heat balance and energy efficiency. For fuel cell plate, a significant parameter, thermal conductivity is the one directly relates to the material itself and varies with temperature. Thermal conductivity testing (TCT) based on ISO 8894 is a common way to determine this parameter. As an early stage in plate material development, this study does not measure any thermal property coefficient. The thermal properties of fuel cell plate materials are quite important in fuel cell development.

2.3.5 Curing Procedure

When using polymer to make composite materials, the forming process directly affects the resultant material performance. This forming process is controlled using curing time and temperature, and determined using Differential Thermal Analysis (DTA) and Differential Scanning Calorimetry (DCS). In principle, the curing temperature selection can be determined by the temperature corresponding to the maximum rate of heat energy release in the curing reaction of the resin. The curing time is obtained by monitoring the residual curing energy through the postcuring test using DTA or DSC. This study applies the DSC test on the cured composites by heating the sample from room temperature to monitor the postcuring reaction. Meanwhile, the thermal stability and oxidative stability are also evaluated through this DSC test.

2.3.6 Fuel Cell Electrochemical Stability

The best way to monitor the fuel cell electrochemical stability of gas delivery plate is through the fuel cell operation. Polarization curve from the fuel cell operation is an important indicator of stability. However, many detailed reaction or phenomena happened inside a fuel cell is hardly shown in the polarization curve, although they directly affect fuel cell power producing stability in long term operation. Some measurements are needed to monitor these inside changes to identify the associated problems. The reason causing the instability includes chemical impurity, chemical evaporation, as well as harmful ionic ingredient.

The X-rays produced in a scanning electron microscope include X-rays with energy characteristic of the elements in the specimen. Energy Dispersion X-ray (EDX) analysis is done through the segregation of X-rays according to their energy counting to generate a spectrum. When applying EDX on a composite sample, the elemental ions can be detected. Mostly, these ions may influence the fuel cell operation based on the discussion of Chapter 2.2. EDX analysis applies electrons on the samples while proton acts on the materials inside a fuel cell. The ions produced from EDX may not be identical to those in a fuel cell environment. However, the active ions are the same in these two conditions.

Beside the influence of ions from the plate materials, other chemical ingredients such as chemical evaporation also affect the fuel cell electrochemical stability. Using DSC test to monitor these non-ionic impurity provides information for further material modification. This study applies both EDX and DSC to check the material stability under the fuel cell electrochemical environment.

2.3.7 Outline of the Testing Methods

The polymer based composite materials used for fuel cell plate have multiple function requirements. The discussion based in Chapter 2.3.1 ~ 2.3.6 has already been simplified, while the practical requirement includes a lot more. A sequential approach on the fuel cell plate material development, which concentrates on one or two properties each time with other properties considered as constraints, cannot satisfy the rapid development requirement. This research applies a concurrent, parallel approach in the development of conductive polymer composite for the screen-printing layer deposition fuel cell plate manufacturing method. The development process is illustrated by the diagram shown in Figure 2-3.

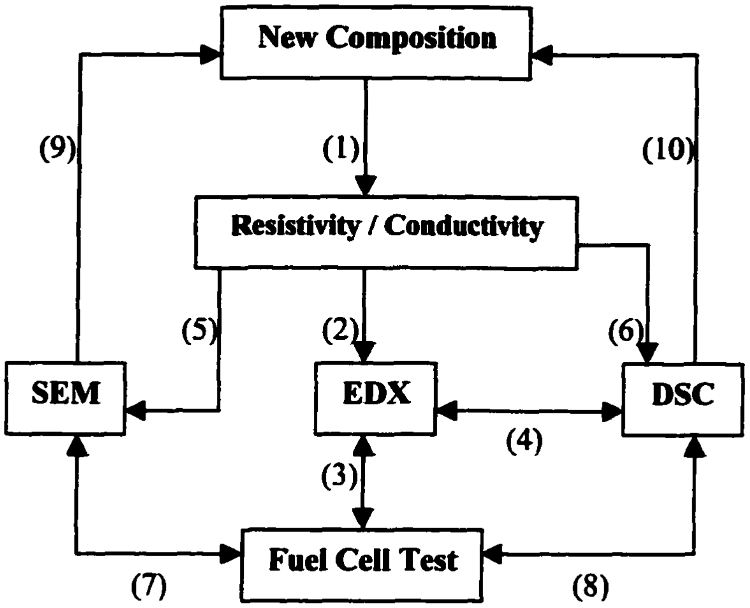

Figure 2-3 Conductive polymer composite development method

for PEM fuel cell plates

Figure 2-3 outlines the development method of conductive polymer composites for fuel cell plate. The path number (1) ~ (10) indicates the test sequence and relations between test results. The bi-directional paths (3), (4), (7) and (8) indicate that the results between the two tests explain each other. The single directional paths indicate that the next test is based on the result from previous test. These relations are further discussed in the following.

- Path (1) – Every new material composition must be first tested on electrical conductivity. Only those with satisfactory conductivity are passed for further measurement and evaluation. However, in this study, some low conductivity samples are still further investigated in order to evaluate the whole material development approach.

- Path (2) – Composite with satisfactory conductivity is checked with the existence of active element ions using EDX. The composite is then tested through fuel cell test indicated by Path (3) and DSC test indicated by Path (4). If no any harmful elemental ion is found in EDX, harmful element ion contamination, such as metallic ions, is not considered as the cause to the instability of the fuel cell found in fuel cell test. Otherwise, the harmful ions may be one of the reasons to cause the fuel cell instability, and further explanation on this instability may be found from DSC test.

- Path (5) – Composites with satisfactory conductivity is passed to the following SEM investigation. Path (7) indicates that SEM needs to be done on the material before and after fuel cell test. Material with good interface bonding and fiber coverage should not have direct mechanical damage in fuel cell operation. The comparison tests identify possible mechanical damage by other reasons such as chemical corrosion in fuel cell operation.

- Path (6) – Composite with satisfactory conductivity is passed to go through DSC to check the chemical stability, thermal stability and chemical evaporation. The result is compared with those from EDX indicated by Path (4) and fuel cell test indicated by Path (8). An unsatisfied DSC result may help to explain the harmful ions found from EDX and the reason of unstable fuel cell test.

- Path (9) – Test on mechanical properties provides information for the further composite modification.

- Path (10) – Test on chemical stability provides information for the suggestion of new composite formation.

In short, any material with satisfactory conductivity goes through the SEM, EDX, DSC and fuel cell test. SEM, EDX and DSC are used to monitor the direct material performance and to give the explanation for unstable fuel cell operation. There is no direct relation between SEM and EDX results even though they are conducted at same time. The information obtained from EDX needs further explanation from DSC test results to determine how to modify the composite. Finally the composite can be improved mechanically and chemically. Only those composite materials, which passed all the tests, including fuel cell test, can be considered successful. These materials are then subject to long term fatigue test in fuel cell operation.

The key aspect in the concurrent material development is the fuel cell test. Due to the multiple functional performance and invisible change of fuel cell plate in fuel cell operation, the development process involves many modern material testing technique, including SEM, EDX and DSC, to investigate the reason of undesirable fuel cell performance caused by plate material and to guide the material modification. Based on this frame, more test methods can be added.

2.4 Fuel Cell Plate Material Testing of Results

One material composition, Graphite/ConductiveLacquer(Polyanaline)/Epoxy, is extensively tested following the procedure illustrated in Figure 2-3, and discussed previously. Other material compositions have also been considered to explain their performance relative to the conductive composites.

2.4.1 Electric Resistivity/Conductivity Test

The measurement of electric resistivity is carried out with an experimental setup made following the ASTM D257-93 standard, shown as in Figure 2-4. The overall resistivity of a sample material is calculated using the equation:

$$\rho = \frac{V}{I} \cdot \frac{A}{t} \tag{2-1}$$

where ρ is the overall resistivity (*ohm-cm*), V is the measured voltage (*volts*), I is the applied current (*amps*), A is the surface area (*cm*^{2}), and t is the sample thickness (*cm*).

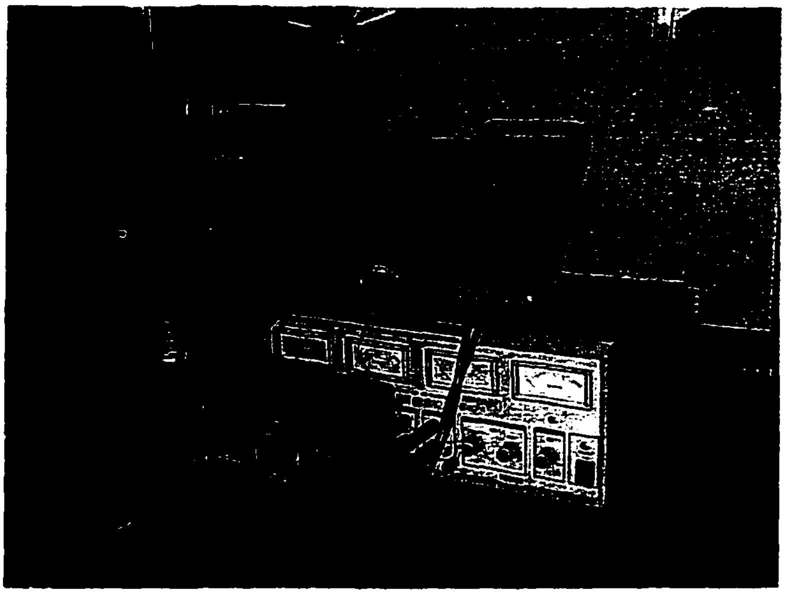

Figure 2-4 Electric resistance testing set-up

The resistivity of conductive polymer composite used for screen printing is set to be of solid resistivity of 3.4 *ohm-cm*, which is one order of magnitude of the solid graphite resistivity of 0.34 *ohm-cm*. The resistivity is tested using samples with different compositions of composite materials.

- Graphite/ConductiveLacquer(Polyanaline)/Epoxy, or Graphite/Polyanaline/Epoxy

The challenge associated the development of this composite comes from the fact that it involves at least three independent materials, each of which may affect the others to produce certain conductive/non-conductive properties. It is necessary to establish an effective methodology, which would allow us to systematically determine the combination of three phases to produce acceptable resistivity. The development procedure of Graphite/Polyanaline/Epoxy provides a guideline for the development of other conductive polymer composites.

Initially, various compositions of lacquer polyanaline and epoxy were made as binder shown in Table 2-1.

Table 2-1 Samples A~C (Epoxy~polyanaline ratio tests).

	Epoxy (%)	Polyanaline (%)
Sample A	20	80
Sample B	50	50
Sample C	80	20

The dry lacquer has a resistivity of 0.4 *ohm-cm*, while the epoxy is a non-conductive material with resistivity between 10^{15} and 10^{22} *ohm-cm*. Their composite combination Sample B (50/50) is semi-conductive with a resistivity of 10^{7} *ohm-cm*. Both Sample A and Sample C have higher resistivity. The result indicates that the lacquer addition can modify the conductivity of epoxy, and certain fraction between lacquer and epoxy, such as 50% to 50%, is adopted in further development.

Holding the lacquer/epoxy composition constant as 50/50 and varying the amount of graphite added, several samples are prepared as in Table 2-2.

Table 2-2 Samples D~G (Graphite addition test)

	Epoxy (%)	Polyanaline (%)	Graphite (%)
Sample D	25	25	50
Sample E	30	30	40
Sample F	35	35	30
Sample G	40	40	20

The results of the resistivity tests shown in Figure 2-5 indicates that the greater the amount of graphite in the sample the lower the resistivity. Sample D (50% graphite) shows the lowest resistivity of only 0.89 *ohm-cm*. However, the mixture was found to be too viscous to be properly screen-printed. Also, sample G (20% graphite) had a resistivity of 18.9 *ohm-cm*, which is substantially higher than the criteria of 3.4 *ohm-cm*. Thus a recommendation of graphite loading in the range of 30-40% appears to be ideal for the mixture.

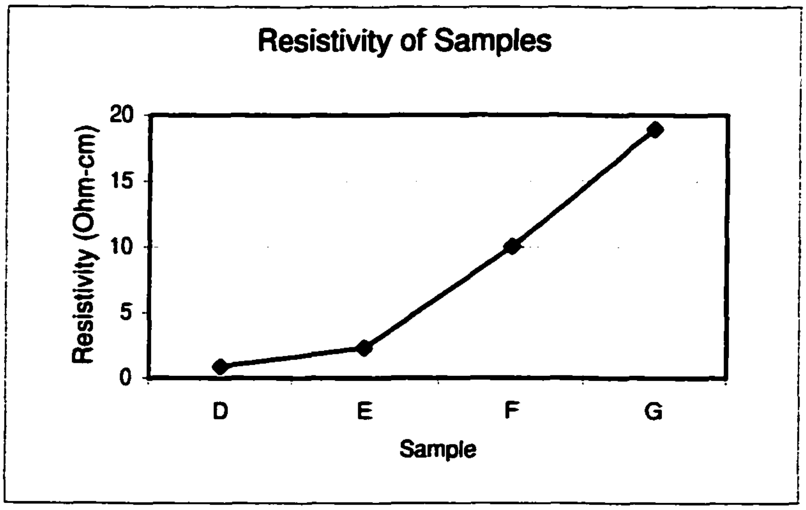

Figure 2-5 Resistivity of Sample D~G

Holding the graphite percentage constant such as 30%, changing lacquer polyanaline and epoxy combination is shown in Table 2-3 to determine the effects of lacquer polyanaline. While the epoxy fraction changed from 60-10%, the lacquer content was varied from 10-60%.

Table 2-3 Samples H~M (Polyanaline~epoxy ratio tests)

	Epoxy (%)	Polyanaline (%)	Graphite (%)
Sample H	60	10	30
Sample I	50	20	30
Sample J	40	30	30
Sample F	35	35	30
Sample K	30	40	30
Sample L	20	50	30
Sample M	10	60	30

As the lacquer polyanaline content was increased from 10% to 40% the resistivity of the samples continued to decrease, to a low of 5.25 *ohm-cm* for Sample K as shown in Figure 2-6. However, after that, the resistivity of the samples appeared to begin increasing with Sample L resistivity of 8.25 *ohm-cm*. This trend cannot be accurately verified due to the fact that Samples L and M with lacquer polyanaline contents over 40% did not cure properly, forming rubber-like resultant samples. Based on this phenomenon and the result from binder composition of Table 2-1, it is believed that extremely high lacquer polyanaline content may actually be detrimental to the conductivity and curing of the sample. Thus the mixture of approximately 30-40% lacquer polyanaline and 40-30% epoxy is adopted for 30% graphite the samples.

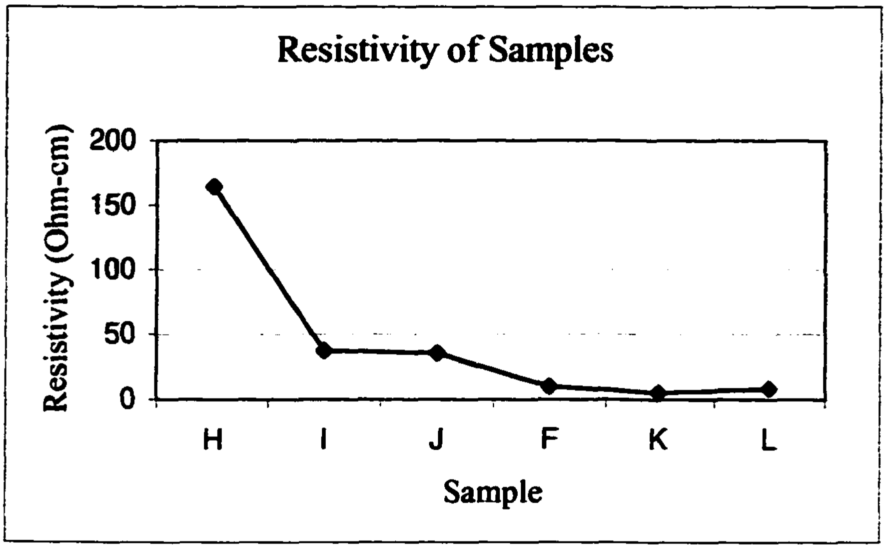

Figure 2-6 Resistivity of Samples H~L

Using graphite contents of 35% and 40%, and varying the relative polyanaline/epoxy contents as Samples J(40/30), F(35/35) and K(30/40), a new set of samples was made as in Table 2-4.

Table 2-4 Samples J~Q (Epoxy~polyanaline ratio tests)

	Epoxy (%)	Polyanaline (%)	Graphite (%)
Sample J	40	30	30
Sample F	35	35	30
Sample K	30	40	30
Sample O	37.1	27.9	35
Sample P	32.5	32.5	35
Sample R	27.9	37.1	35
Sample N	34.3	25.7	40
Sample E	30	30	40
Sample Q	25.7	34.3	40

Sample Q with relative epoxy/polyanaline/graphite content as 25.7/34.3/40 could not be cured properly. The resistivity test results from Samples J, F, K, O, P, R, N and E are shown in Figure 2-7. While the resistivity decreases as lacquer polyanaline content increases for 30% graphite in Samples J, F, and K. This trend is not kept for 35% graphite Samples O, P and R. For Sample K, which has lowest resistivity 5.3 *ohm-cm* and still higher than the desired resistivity of 3.4 *ohm-cm*, and the 30% graphite content seems not enough to reach the ideal conductivity. The lacquer polyanaline content plays a key role to resistivity reduction at relatively low graphite content of 30%.

Samples N, E and Q vary the lacquer polyanaline content from 25.7% to 34.3% with constant graphite content of 40%, and Samples N and E both resulted in excellent resistivities of 2.7 *ohm-cm* and 2.3 *ohm-cm*, respectively. Even though these samples are too viscous for screen printing, these compositions are still considered in generally application of conductive polymer composites for fuel cell plates. The tests also indicate that the 40% content graphite loading begins to show that the variations of lacquer polyanaline content from 25.7% to 34.3% do not influence much on the resistivity.

The resistivity of Samples O, P and R with constant graphite content at 35% shows the lowest value at 2.2 *ohm-cm* for Sample O and increased resistivity for both P and R. The unexplainable sharp varying results among O, P and R may be considered as deviation. Meanwhile this deviation also indicates that the lacquer content has great influence on the sample's resultant resistivity when graphite content is around 35%.

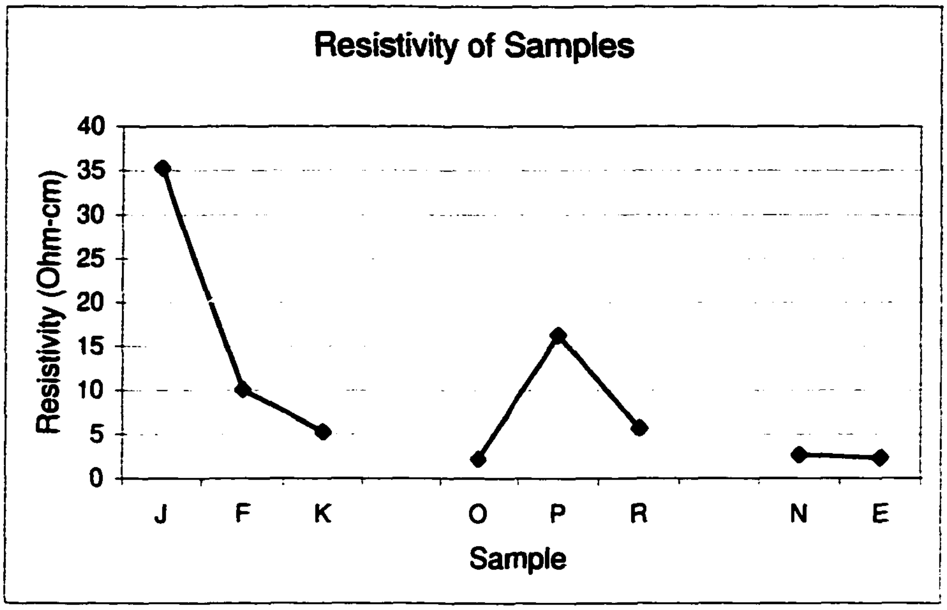

Figure 2-7 Resistivity of Samples J, F, K, O, P, R, N, E

In conclusion of this first step of the conductivity based material development of Graphite/ConductiveLacquer(Polyanaline)/Epoxy composite, Sample O with 2.2 *ohm-cm* resistivity is the most effective. The graphite loading below 30% is considered unacceptable, while above 40% is not suitable to screen printing.

The optimum composition between the three phases fall in a narrow range for both lacquer polyanaline and epoxy contents between 27.9% and 37.1% respectively, with graphite loading around 35%.

- Other compositions

The composite made of 20% Graphite ~ 12% SilverEpoxy ~ 68% PosterInk showed really good conductivity. The electric resistivity of the composite is between 1 ~ 10 ohm-cm, partially due to the softness of the sample.

On the other hand, the composite made of 35% Graphite ~ 25% SilverEpoxy ~ 40% Epoxy appeared totally insulated with a very high resistivity.

2.4.2 Energy Dispersion X-ray (EDX) Study

The EDX machine associated with the scanning electron microscopy (SEM) used in this study is shown in Figure 2-8, which located in the Department of Biology, University of Victoria.

Figure 2-8 EDX (left) and SEM (right)

The EDX tests on a dried sample of commercial water based, organic poster ink showed *Ba* and *S* ions as shown in Figure 2-9. When testing the mixture of poster ink and graphite powder that is used to make the screen-printed fuel cell gas delivery plate, the same ions still show up as in Figure 2-10. These ions are considered harmful to the fuel cell electrochemistry environment.

Figure 2-9 EDX, commercial poster ink, dried sample (#Ink-1)

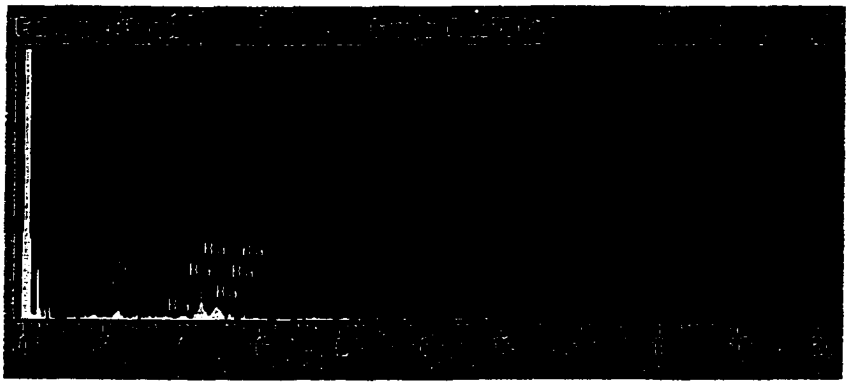

Figure 2-10 EDX, poster ink and graphite screen printed plate sample before fuel cell test (#Paint-1)

After the plate is tested in a running fuel cell, the plate material shows *Ba* and *S* as well as additional *O* ions in the EDX test, as shown in Figure 2-11. Meanwhile, *F* ion can be detected in the plate material located closer to the MEA reaction area, as shown in Figure 2-12. The only possibility for the *F* ion to appear in the plate is that the dried organic ink material reacted with the membrane material ($R_f[OCF(CH_3)CF_2]OCF_2CF_2SO_3H$).

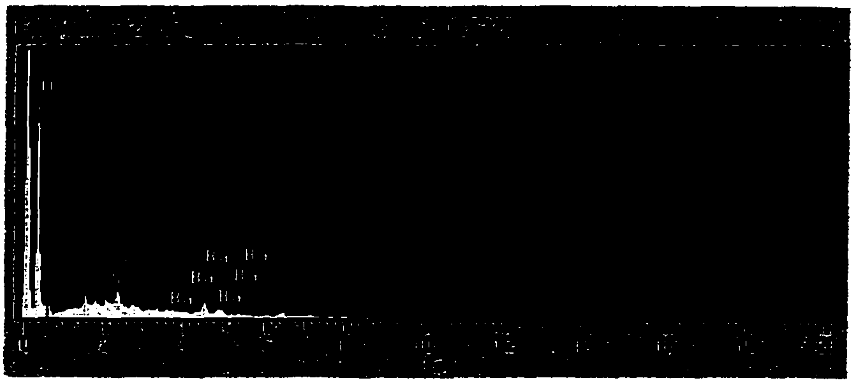

Figure 2-11 EDX, *Ba* and *S* ions from the poster ink/graphite Screen-printed plate sample after fuel cell test (#Sp1-2)

Figure 2-12 *F* ion appears in the water-based organic composite ink after fuel cell test (#Spm2-1)

The Graphite/Polyanaline mixture solid sample did not show any metallic ions in the EDX tests (Figure 2-13). Graphite/Polyanaline/Epoxy material used for making the fuel cell plates shows same phenomena before and after fuel cell test, even though unstable fuel cell performance was observed curing fuel cell tests. This issue is to be discussed in Chapter 2.4.5. The tests indicate that the fuel cell electrochemistry problem caused by the composite material is not due to the active metallic ions.

Figure 2-13 Graphite/Polyanaline sample (#g24-3)

Other EDX tests on composite made of 20% of Graphite, 12% of SilverEpoxy and 68% of PosterInk revealed *S* and *Ba* ions in non-silver part (Figure 2-14), while the general image shows mainly *Ag* ions (Figure 2-15). This result is caused by both poster ink and silver epoxy. In general, the *Ag* ions are more active, and the *S* and *Ba* ions are found in some portions in the composite, even though 68% poster ink has been used. In comparison, the 35% of Graphite, 25% of SilverEpoxy and 40% of Epoxy mixture shows no any ions in the EDX test, even though the silver epoxy amount is much higher. In short, the strong binder epoxy can limit the activity of the metallic ion, such as *Ag*, thus sacrificing the electric conductivity.

Figure 2-14 EDX, 20% Graphite ~ 12% SilverEpoxy ~ 68% PosterInk sample, non-silver part (#0412a-1)

Figure 2-15 EDX, 20% Graphite ~ 12% SilverEpoxy ~ 68% PosterInk, general image (#0412a-4)

2.4.3 Scanning Electron Microscope (SEM) Microstructure Analysis

The SEM machine used in this study is shown in Figure 2-8, where is located in the Department of Biology, University of Victoria.

The dried sample of commercial water based organic poster ink showed a uniform surface under the SEM microstructure examination, as shown in Figure 2-16. The screen-printed fuel cell gas delivery plate made by the mixture of poster ink and graphite powder, formed a good coating surface (Figure 2-17) before the fuel cell test. After the running fuel cell test, the plate material showed serious coating lost (Figure 2-18). The binder lost is a typical of mechanical damage caused by the weak interface between the ink binder and the graphite powder, as well as certain chemical corrosion. The SEM examination concluded that a stronger binder needs to be used for the printing ink to replace the weak water based organic poster ink.

Figure 2-16 SEM, commercial poster ink (Magnification ×350, #Ink1)

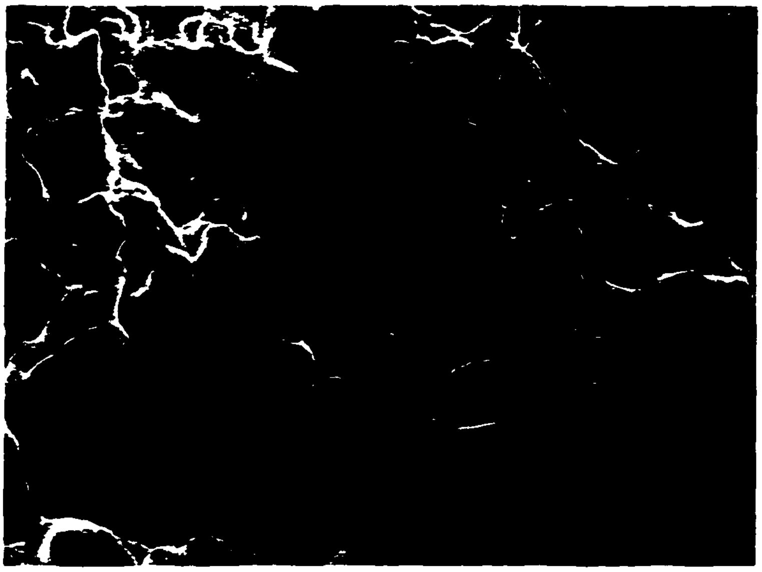

Figure 2-17 SEM, poster ink and graphite screen printed plate sample before fuel cell test (Magnification ×200, #Paint1)

Figure 2-18 SEM, coating wore out in the poster ink/graphite Screen-printed plate sample, after fuel cell test (Magnification ×350, #Sp2-1)

The Graphite/Polyanaline mixture solid sample shows smooth lacquer coating on the graphite powder surface (Figure 2-19). Two promising compositions of the Graphite/Polyanaline/Epoxy material, Sample K and Sample O, are selected for the SEM microstructure study. Figure 2-20 shows that the Sample O has a much smoother binder coating surface than the Sample K shown in Figure 2-21, with a different weight fraction, even though both have low electric resistivity as shown previously in Figure 2-7. The smooth microstructure of fuel cell plate is achieved with the approximate 1/3, 1/3, 1/3 weight fraction of Graphite/Polyanaline/Epoxy between Samples K and O. No mechanical damage is found after fuel cell running test (Figure 2-22). The unstable fuel cell performance, to be discussed later in Chapter 2.4.5, is not caused by mechanical bonding weakness.

Figure 2-19 SEM, Graphite/Polyanaline mixture solid sample

(Magnification ×50, #G24-2)

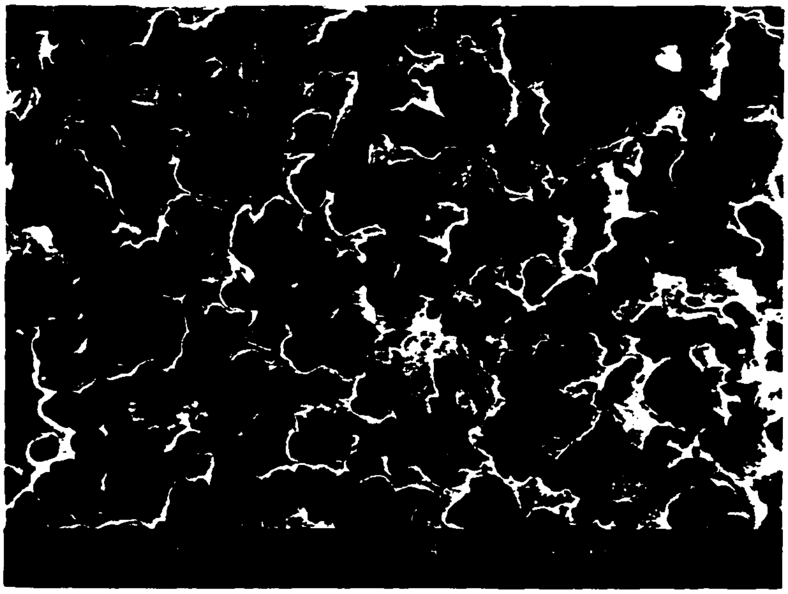

Figure 2-20 SEM, Graphite/Polyanaline/Epoxy with 35%~28%~31% weight fraction (Sample O)

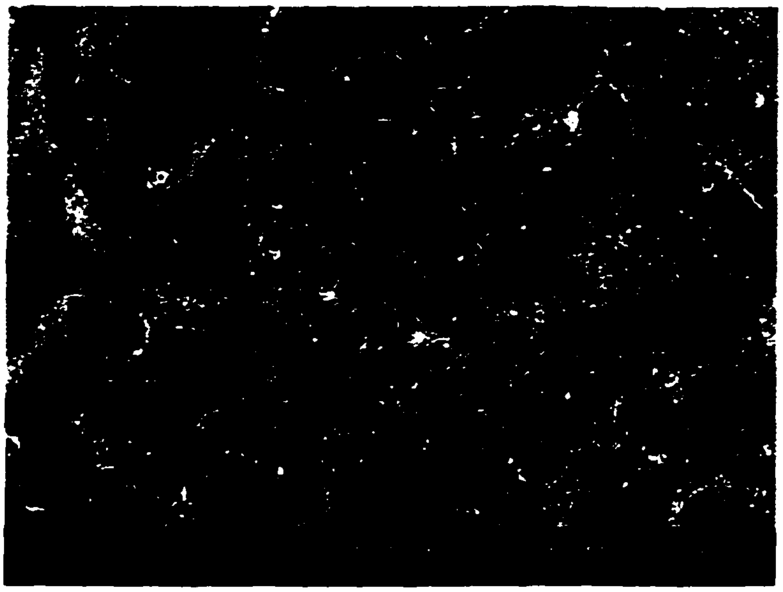

Figure 2-21 SEM, Graphite/Polyanaline/Epoxy with 30%~40%~30% weight fraction (Sample K)

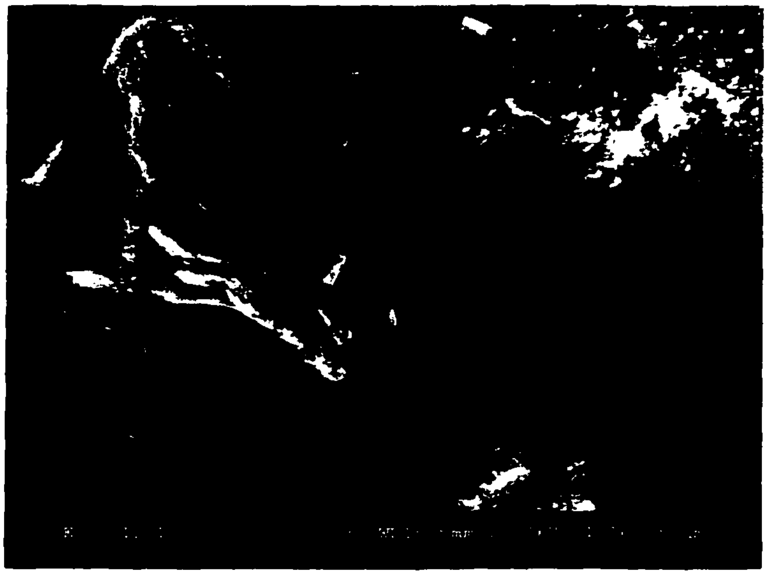

Figure 2-22 SEM, Graphite/Polyanaline/Epoxy, approximate 1/3,1/3,1/3 weight fraction, plate after fuel cell test (#990415a)

The microstructure of the 20% Graphite ~ 12% SilverEpoxy ~ 68% PosterInk shown in Figure 2-23 is much rougher than that of the 35% Graphite ~ 25% SilverEpoxy ~ 40% Epoxy shown in Figure 2-24. The strong binding of epoxy in the 35% Graphite ~ 25% SilverEpoxy ~ 40% Epoxy provides a very good coating on the graphite powder and forms a smooth surface. Obviously, the weak bonding of the 20% Graphite ~ 12% SilverEpoxy ~ 68% PosterInk is not enough to prevent mechanical damage during the fuel cell operation.

Figure 2-23 SEM, 20% Graphite ~ 12% SilverEpoxy ~ 68% PosterInk (#990412a)

Figure 2-24 35% Graphite ~ 25% SilverEpoxy ~ 40% Epoxy (#990413a)

2.4.4 Differential Scanning Calorimeter (DSC) Analysis

The DSC tests used in this study are done in the Department of Chemistry, Simon Fraser University, and in the Department of Chemistry, University of Victoria. The machine is shown in Figure2-25.

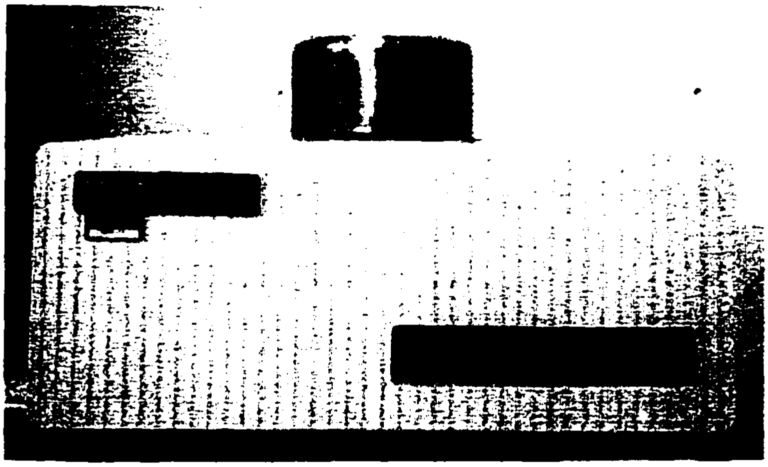

Figure 2-25 DSC testing machine

On the Graphite/Polyanaline/Epoxy composite development, the successful samples identified by the discussed process with different weight fraction were passed for DSC analysis. The result from a typical DSC test from the composite and the result from pure conductive lacquer polyanaline are shown in Figure 2-26. The lacquer polyanaline shows complex reaction after 120°C, that is the upper working temperature limit recommended by the manufacturer. The Graphite/Polyanaline/Epoxy composite has a remarkable reaction peak at around 75°C, which is within the range of fuel cell operation temperature. Comparing these two curves, this reaction peak is not directly caused by the lacquer itself, rather by the combination of lacquer polyanaline and epoxy, which are unsaturated or unstable. This hidden "defect" provides a good explanation to the unstable performance of fuel cell operation to be discussed in next sub-section. The processing method and/or composition of the composite should be modified.

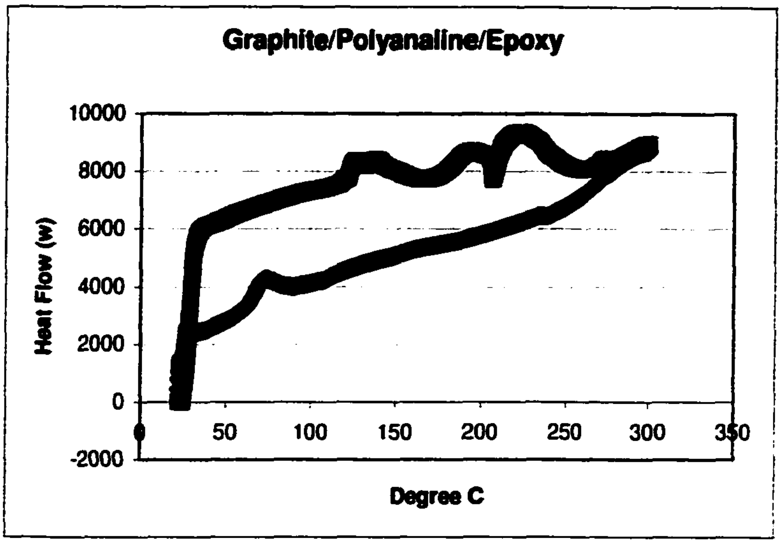

Figure 2-26 DSC, Blue (or black): Graphite/Polyanaline/Epoxy; Red (or grey): pure lacquer polyanaline

The DSC test result of 20% Graphite ~ 12% SilverEpoxy ~ 68% PosterInk (Figure 2-27) presents very unstable thermal behavior within the temperature ranged from 60°C to 250°C. The broad range indicates that it is not related to the post-polymerization reaction of SilverEpoxy, and must be caused by the organic ink itself. Reducing the amount of organic poster ink and/or applying elevated temperature to "burn out" the organic ingredient are possible solution to this problem.

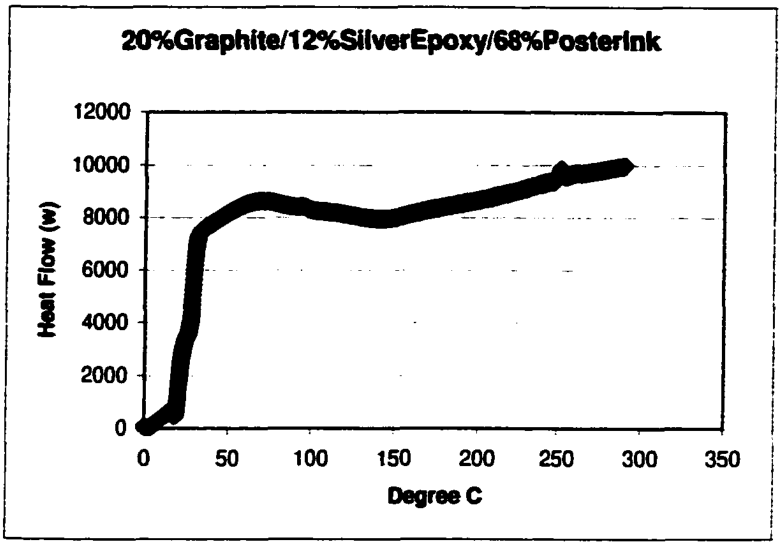

Figure 2-27 DSC, 20% Graphite ~ 12% SilverEpoxy ~ 68% PosterInk (#SP2)

Figure 2-28 shows that the 35% Graphite ~ 25% SilverEpoxy ~ 40% Epoxy composite has excellent thermal stability with a wide temperature range. Epoxy is the only polymer ingredient in this composite. The use of epoxy as the binder is a good solution for the fuel cell plates working at elevated temperature, even though its electric conductivity is still a major concern.

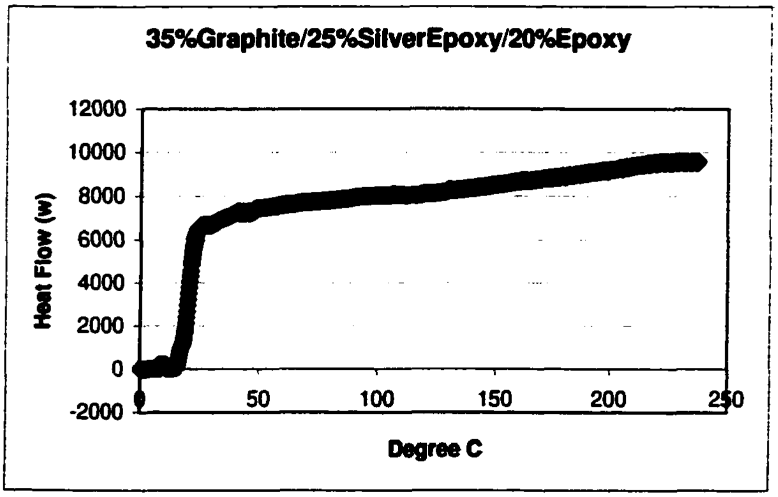

Figure 2-28 DSC, 35% Graphite ~ 25% SilverEpoxy ~ 40% Epoxy (#SP3)

2.4.5 Single Fuel Cell Test

The fuel cell test is carried out using the ASA fuel cell test station in the Fuel Cell Research Lab at University of Victoria. The fuel cell test station is shown in Figure 2-29.

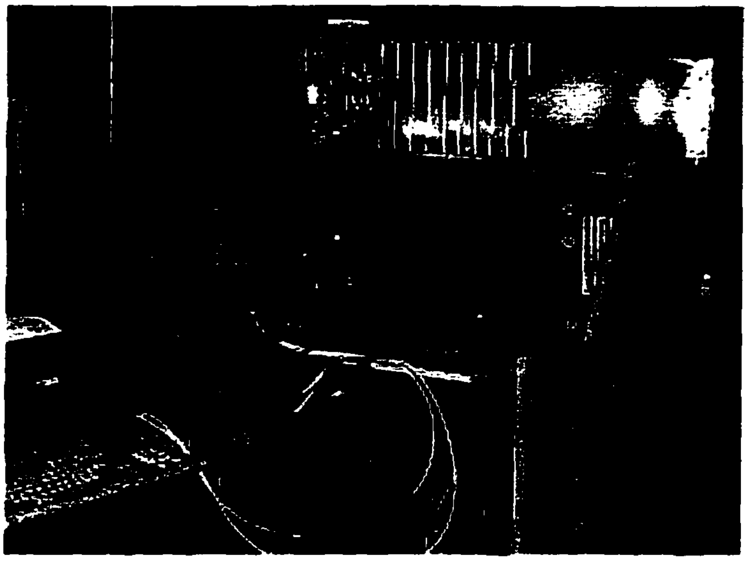

Figure 2-29 ASA Fuel cell test station

Verification on electric conductivity of the conductive lacquer polyanaline was done by applying lacquer paint on a solid graphite plate and using it as the oxidant gas supply plate of a fuel cell. The polarization curves of the fuel cell using bare and paint solid graphite plate are shown in Figure 2-30. The lacquer polyanaline painted plate is coated with a thick lacquer layer with a thickness of about 0.2 *mm* on the top of the flow channel and channel wall sides. The top painted surface directly contacts with the MEA. The relatively rough top surface and the additional interface between coating lacquer and solid graphite considerably increase electric resistance. The result in Figure 2-30 indicates that the ohmic loss by this increased resistance is under acceptable. Meanwhile, the lacquer polyanaline working under the fuel cell environment remains stable and strong.

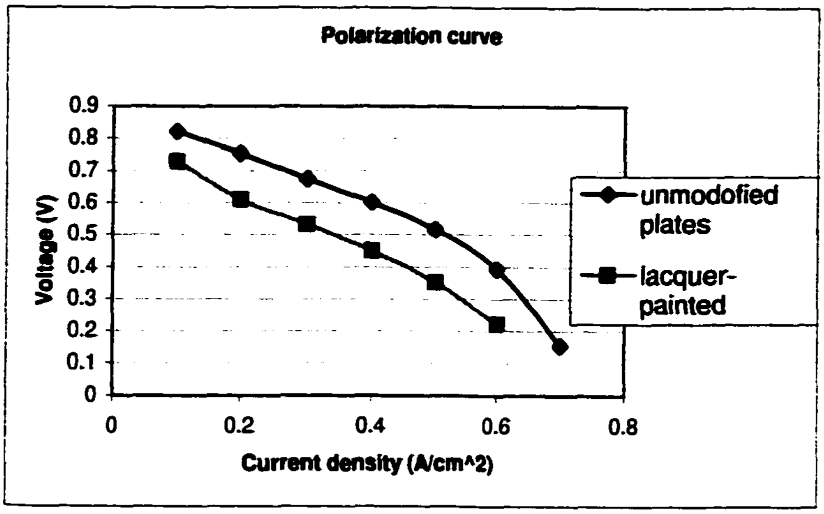

Figure 2-30 Polarization curve of conductive lacquer polyanaline paint on plate

The fuel cell plate make with approximate 1/3, 1/3, 1/3 weight fraction of Graphite/Polyanaline/Epoxy shows heavy ammonia emission during the fuel cell test. Unstable cell voltage appears when the electric current increases just slightly causing both cell voltage and current to jump up and down, as shown in Figure 2-31. When the current returns to zero, the cell voltage also returns to the maximum voltage value, indicating no conductance loss during the operation. Indeed, the composite plate does retain good structure and conductivity after fuel cell operation. The SEM microstructure investigation and EDX analysis on the composite showed no noticeable mechanical failure and metallic ionic change after fuel cell test. The emission can only be explained and revealed in the DSC test, caused by the chemical instability. The next step of material modification needs to concentrate on the processing method and weight fraction adjustment of this composition.

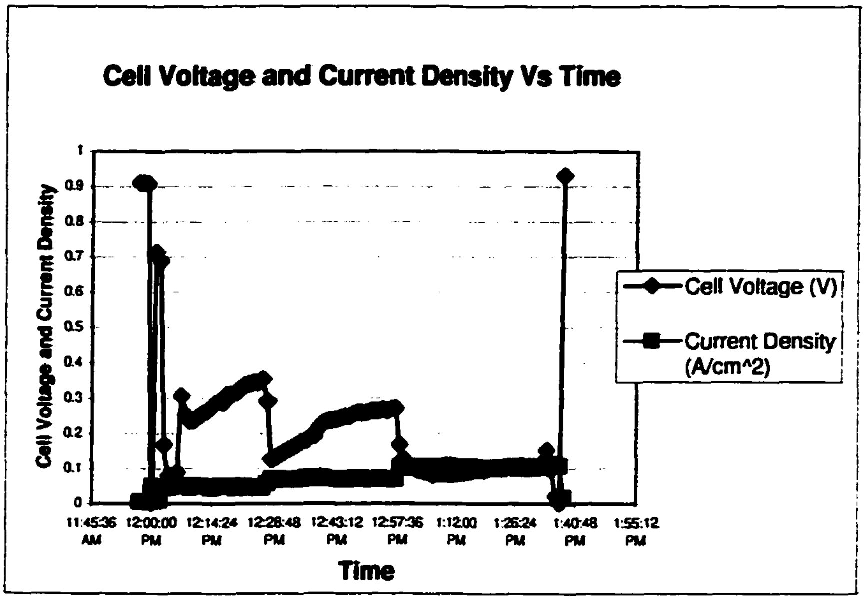

Figure 2-31 Fuel cell, Graphite/Polyanaline/Epoxy plate: Voltage and current density history profile

2.5 Summery on Fuel Cell Plate Composite Material Development

2.5.1 Feasibility of Layer Deposition Technique

The success of using composite ink formed by poster ink and graphite and the screen printing layer deposition method to make fuel cell plates has shown the promise of this alternative manufacturing method. The flaws of the ink material used initially motivated this material development. The feasibility of this 3D layer deposition technique for making fuel cell plates further relies on the feasibility of layer deposition materials. As for all other application, material development dominates manufacturing success.

2.5.2 Feasibility of Conductive Polymer Composites for Fuel Cell Plates

At present, no standard method and published criterion exist on composite material development for fuel cell plates. This study considers conductivity, mechanical performance, stability and manufacturability to produce the optimal solution for fuel cell plate material following the proposed methodology shown in Figure 2-3. As an optimization procedure to develop the three phase composite materials, there is no guarantee that an optimal solution within certain composition category can be achieved. A large number of ingredient compositions of binder, modifier and reinforcement need be considered.

The poster ink diluted composition can easily produce good conductivity, but the ratio of the composite material needs to be fine controlled to get the optimal structure bonding. The epoxy binder is strong on the structure, mechanical, and chemical performance, but its conductivity needs to be modified.

During the development of conductive polymer composites, the mechanical properties of the composite can be monitored through its microstructure using SEM. The stability of the composite in fuel cell operation can be monitored with DSC and EDX tests. The monitoring methods further guide material development. The final success of the composite development will be determined by finding out certain composition of all acceptable components, to reach the balance between fuel cell electrochemistry stability, mechanical performance, and electrical conductivity.

2.6 Suggestions to Full Scale Development

The screen printing based, fuel cell gas delivery plate manufacturing method has many advantage, including low process and equipment cost, scalable from single prototype to batch production, low initial cost for small batch, and superb capability to handle complex flow field geometry.

The success on screen printing 3D layer deposition technique development for building fuel cell plates leads to the challenge on conductive polymer composite material development. To extend the success of this low cost and rapid processing layer deposition method, a parallel material development method for the conductive polymer composite was introduced in this research.

The research demonstrated the material development process through the testing and development of the three phase Graphite/Polyanaline/Epoxy composite, and showed promising results. This approach, if followed through, can eventually identify the ideal composite for the fuel cell plate and the ink for screen printing. However, due to the vast possibilities of the material composition and process selections, the final specific composition of the composite is beyond the scope of this study.

Chapter 3. Flow Field Design and Virtual Prototyping of PEM Fuel Cell Gas Delivery Plates

The primary function of the fuel cell plates is to deliver reactant gases, hydrogen and oxidant air, to the MEA of the PEM fuel cell through the flow fields on the plates. The flow field also provides the exit pass for the by-product water.

The design of the flow field has strong influence to the performance of a PEM fuel cell. These can be classified as:

- The flow field of the air delivery plate provides oxygen to the cathode of the fuel cell. Since air only contains about 21 percent of oxygen, the oxygen in the air can be easily consumed near the MEA boundary. Improper flow field design can cause a depleted oxygen layer at the air stream to MEA interface, thus leading to poor fuel cell performance. Optimal flow field is aimed at eliminating this problem and considerably improve fuel cell performance.

- The by-product water of fuel cell operation needs to be brought out by the oxidant air stream. Improper design of the flow field will cause inadequate pressure drop and form liquid water blocking the flow channels. This type of flooding is often the cause of fuel cell performance drop.

In addition, both of the electric current produced by the fuel cell is conducted by, and the load applied to the fuel cell is supported by the channel walls of the flow field of the fuel cell plates. Electric conductivity and mechanical strength are key influencing factors to flow field and fuel cell plate design. For the screen-printed plates, the material of the solid substrate, the printed channels and their interface are considered. Electrochemistry stability is another key consideration due to the strict performance conditions of a PEM fuel cell. Meanwhile, thermal performance is also significant because the thermal conductivity of the plates strongly influences the cooling efficiency and the overall fuel cell efficiency.

The major design issues of fuel cell flow field is briefly discussed in this chapter through the example fuel cell plates and flow fields illustrated in Figure 3-1.

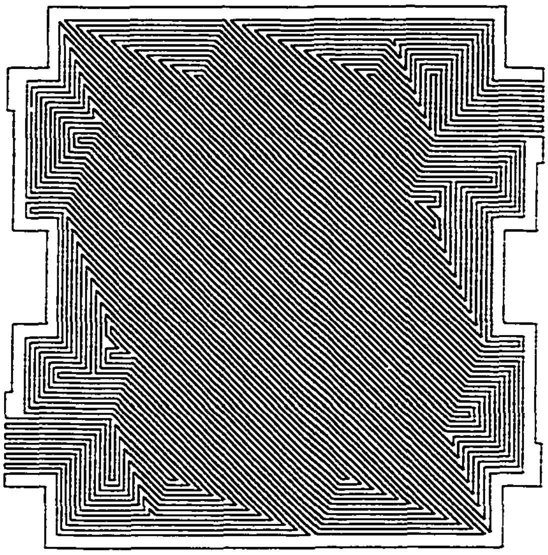

(a) Oxidant air flow field [Dong 1999b]

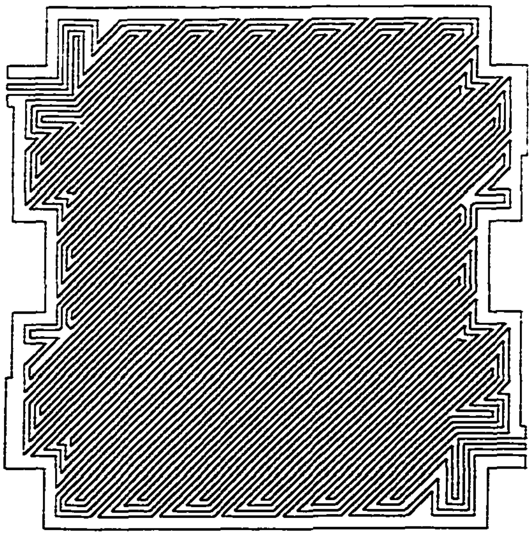

(b) Hydrogen fuel flow field [Dong 1999b]

Figure 3-1 PEM Fuel cell plate and flow fields

3.1 Oxidant Air Flow Field and Plate Design

3.1.1 Basic Principles

Both hydrogen fuel plate and oxidant air plate can use either one continues serpentine channel or multiple serpentine channels, as shown in Figure 3-1. During the fuel cell electrochemical reaction, hydrogen fuel delivered in by hydrogen flow field is consumed as proton transporting across the polymer electrolyte membrane. The hydrogen pressure thus decreases along the channel. Because pure hydrogen is the only component in the flow channel, one continuous serpentine channel plate is acceptable. On the other hand, the oxidant air plate delivers air, which contains only 21% of oxygen, and this reactant is consumed. One single long oxidant air channel will cause much lower oxygen concentration at the latter part of the flow channel. This ultra non-uniformity of oxygen distribution heavily influences the fuel cell performance. Therefore, short multiple serpentine channels are more suitable to the oxidant air flow field.

Both one and multiple channel plates require a balanced ratio between the channel area and wall area. Large channel area with thin channel walls provides more fuel gas active area. However, the thinner channel walls have lower structure strength, impose higher stress on the MEA and lead to higher internal electrical resistance. On the other hand, thicker channel walls reduce the structure strength and resistance problem, but smaller electrochemistry active area. At present, channel area is selected to be larger than the channel wall area to achieve fuel cell performance.

The pressure difference between the adjacent channels along the serpentine channel could cause the gas to pass over the channel wall. This is called "by-pass", which causes uneven pressure drop and gas distribution along the flow channel and influences the fuel cell performance. The by-pass can be minimized by properly laying the flow field, adjusting the channel wall width the stack compression pressure. These design principles are reflected in the flow field design shown in Figure 3-1.

The surface flatness of the flow field plates ensures even contact across the plate and appropriate sealing, as well as reducing the by-pass problem mentioned. Since the contact resistance between the plate and MEA dominates the internal resistance, the surface flatness of plate heavily influences the plate conductivity. Good surface flatness also provides even stress distribution across the plate, reducing premature structure failure of the MEA and the solid plate.

Today, these issues are addressed at the early stage of flow field and fuel cell plate design.

3.1.2 Detailed Performance Consideration

Except the one or multiple channel consideration, the pressure drop along the flow channels, especially for the oxidant air delivery plate is also a key aspect in fuel cell plate design. The water formed at the cathode accumulates in the channels adjacent to the cathode, leading to low and unstable fuel cell voltage when running for a long time. The water droplets also tend to form large ones and cling to the bottoms and sides of the channels, in which little or no gas is passing. A force, which increases with the size and number of the droplets, is required to move the droplets through the channel. The technique is patented by Ballard Power Systems by controlling the channel pressure drops [Watkins 1992].

The oxidant air delivery flow channel also faces the oxygen depletion problem. This phenomenon is caused by the laminate flow of the air stream inside the flow channel, and oxygen consumption at the cathode. The non-uniformity of oxygen distribution in the channel cross-section can only be compensated through the diffusion effect between the layers of the laminate flow. When the laminate flow is replaced with turbulent flow or local turbulent flow, the uniformity of oxygen distribution can be much improved, and enhanced oxygen concentration along MEA cathode side can be produced.

The desired turbulent flow can be introduced by changing the uniform cross-section of channels to non-uniform dimension. Various geometries that can change the channel cross-section have been introduced and tested in Fuel Cell Lab at University of Victoria [Dong 2000]. One of these options is discussed in this dissertation. These new designs can be easily fabricated using the layer deposition flow channel building technique. The application of layer deposition technique as well as the plate material development has been discussed previously in Chapter 2.

3.1.3 Oxygen Enhancement

The objective of oxygen enhancement is to improve fuel cell performance by increasing the current density through new flow field geometry of the fuel cell air delivery plate. The current density is increased by raising the overall current density distribution. This is accomplished by improving the oxygen concentration at the MEA interface within the air channel. The theoretical model for the fuel cell current density distribution presents: [Yi 1999]

$$i=i_0\frac{C_{O_2}}{C_{O_2,ref}}\exp(\frac{4kF}{RT}\eta) \qquad (3\text{-}1)$$

where, the i_0 is the exchange current density, C_{O2} is the molar concentration of oxygen gas at the MEA interface, $C_{O2,ref}$ is the reference concentration of oxygen at 1 *atm*, F is the Faraday constant and k is the transfer coefficient. The Equation 3-1 indicates that for a given potential η, the current density is proportional to oxygen concentration. Therefore improved oxygen concentration at the MEA interface leads to an increase in power density [Oldham 1994].

The oxygen concentration at the MEA cathode interface can be enhanced. through many means, including adding blocks and steps to the flow channel, changing flowing surface texture, alternating flow channel shapes and cross-sections, etc. These innovative flow channel features are discussed in details in the invention of [Dong 2000]. The improved fuel cell performance is observed through the measured polarization curve with increased current density.

In this dissertation, we will chose one of the added flow channel features, the steps, to demonstrate its function in improving the oxygen concentration at the MEA interface, and increasing fuel cell power output. The step feature is illustrated in Figure 3-2.

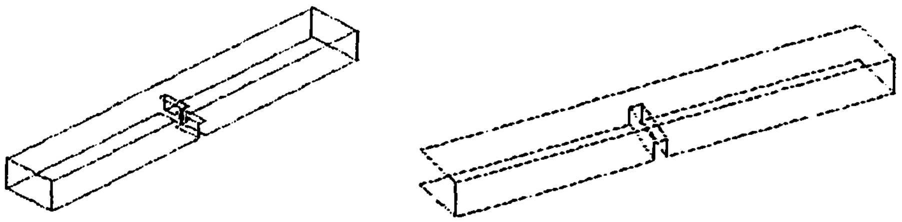

(a) Offset steps (b) Single step

Figure 3-2 Added step feature in the flow channel [Dong 2000]

3.1.4 Test of Prototype Plates

The oxygen enhancement prediction from blocked flow channel is verified through comparative cell tests using a modified Ballard MK-5 fuel cell plate with insert blocks. The experiment setup is shown in Figure 3-3. In this experiment, a cross slot is added to a standard Ballard Mark-5 oxidant air delivery plate. A slotted stainless bar is inserted into the slot. By sliding the stainless bar in the slot of the plate, the flow field channel will either have no step, a full step or a corner block of varying size.

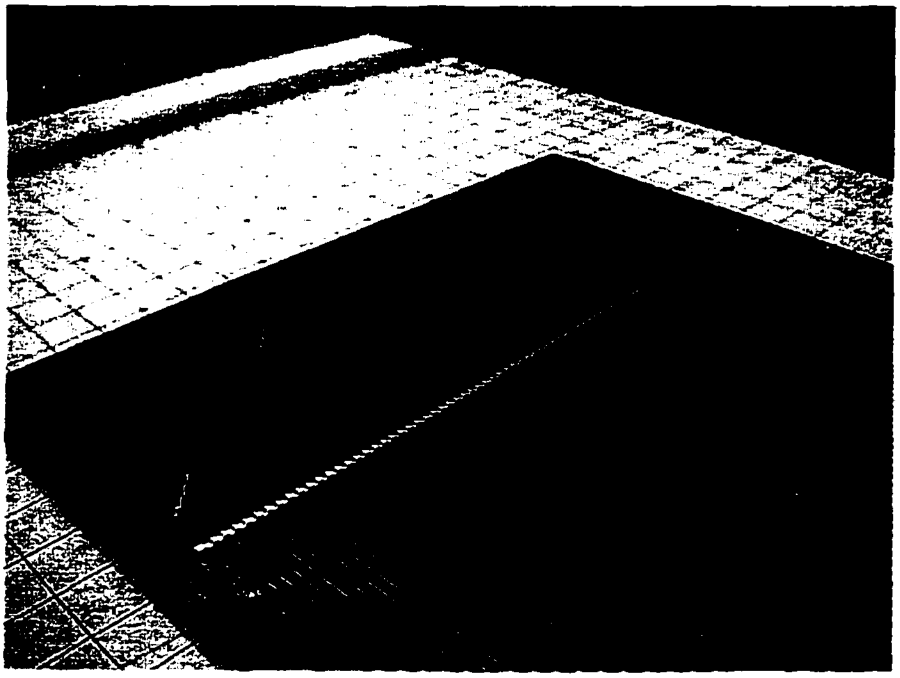

Figure 3-3 Stepped channel experiment plates [Mackie 1999]

Baseline test was conducted by using no-block insert for comparison with the effect of block insert. An increase in cell voltage with the oxygen enhancement blocks was observed, as shown by the polarization curve in Figure 3-4. The voltage gain also increases with the current densities of the cell. A 35% cell voltage increase was recorded at the current density of 0.8 A/cm^2. The significant oxygen content increase 112% in the air stream at the MEA interface, later predicted by the CFD simulation, is indirectly verified. The intent of the flow field feature design is validated.

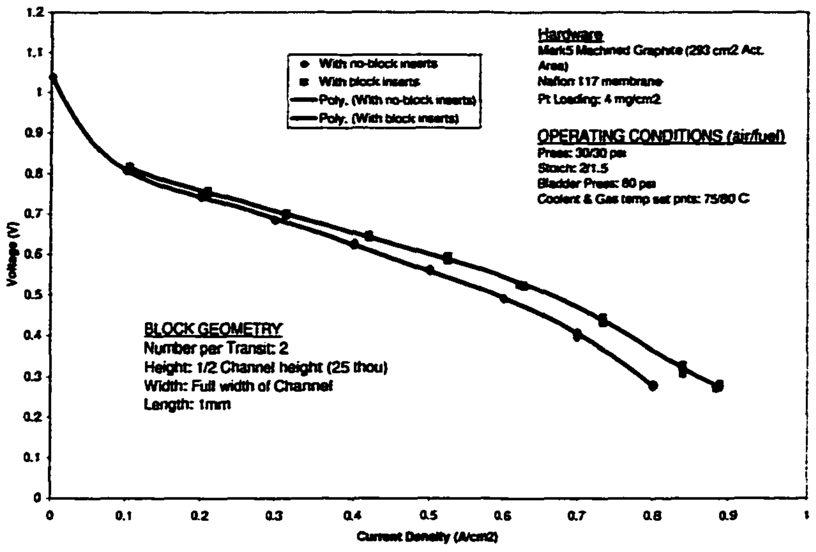

Figure 3-4 Polarization with inserts and non-insert in air delivery plates

3.2 Objective of Virtual Prototyping Research

As discussed in the previous section, the design of fuel cell plates and flow fields is a very complex task involving many considerations and far beyond human intuition. To avoid a lengthy trial-and-error design-testing-redesign procedure, some early feedbacks of fuel cell performance for a given design become essential. The methods of virtual prototyping fuel cell gas delivery plate are introduced in this work to solve the stated design problem, with a focus on the more demanding oxidant air flow field and plate design. The study also concentrates on the flow fields and plates that are produced using the screen-printing layer deposition method.

3.3 Computer Visualization

Virtual prototyping of PEM fuel cell gas delivery plate includes flow field, thermal and structure designs. The parametric CAD tool, Pro/ENGINEER, is used to model the layered structure of the flow channel. The plate is formed using the screen-printing layer deposition process with a solid substrate and a building layer, which is reflected in the computer model.

The general shape of a PEM fuel cell hydrogen fuel delivery plate, oxidant air delivery plate, and membrane exchange assembly (MEA), is shown previously in Figure 1-1 (a) of Chapter 1. The simplified flow field of a fuel cell plate is illustrated in Figure 3-5. This plate is attached to one side of the MEA. The linked parallel channels are connected to an air inlet and an air outlet at each end, to continuously feed compressed air/oxygen to the current generating MEA.

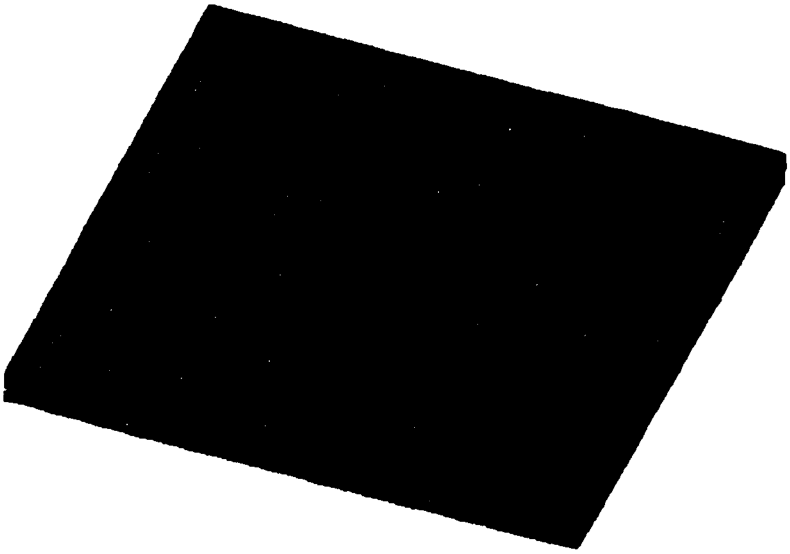

Figure 3-5 A simplified PEM fuel cell plate model

In this study, the solid plate model is used for structure integrity analysis and heat transfer thermal analysis using finite elements method. The flow channel geometry model is used to form computational fluid dynamics (CFD) codes for gas flow condition analysis, especially the oxygen level of the compressed air within the air channel at the MEA interface. These parametric models support performance analysis and allow design optimization on plate structure and flow field geometry to be carried out. The analysis provides quick feedbacks and optimized configurations to a new fuel cell fuel and oxidant delivery plate.

3.4 Fuel Cell Performance Prediction Through CFD

The CFD is used in this research to simulate the oxidant air flow and oxygen concentration in the flow field, thus predicting the performance of the fuel cell. The simulation associates heat transfer and interaction with solid using nonlinear differential equations and channel boundary conditions. Previous CFD studies on simple flow channels showed potential improvements on heat transfer with appropriate rib geometry [Zapach 1993]. Related issues including turbulence modeling, numerical accuracy and computational efficiency have been investigated on flows over bluff obstacles [Zeidan 1995].

This research focuses on the air flow field conditions within the flow field of the fuel cell plates. The air flow behavior simulation is used as an indirect fuel cell performance measure in the design optimization of the fuel cell plates. Due to the 3-D nature of the air flow problem, 2-D simplification cannot be used, leading to intensive computation. The CFD modeling of this study is only used to set up the air flow simulation. After the model is verified with experimental results, the model is applied directly in the design study.

3.4.1 Surface Mounted Rib Flow Channel

A regular rectangular cross sectional air delivery channel is surrounded by three solid wall surfaces and one surface of the MEA. Fresh air with 21% oxygen concentration enters the channel inlet with the oxygen gradually consumed by the fuel cell at the MEA cathode side surface. The continuous oxygen depletion considerably reduces the oxygen concentration at the air-to-MEA interface. The higher oxygen concentration air away from the MEA can only diffuse to the low oxygen concentration air area at the MEA interface. This sharply reduced oxygen distribution along MEA causes poor fuel cell reaction, and significant non-uniformity in current density distribution. On the other hand, the quickly decreased oxygen along MEA cathode side surface also affects the oxygen efficiency available in the flow channel.

The objective of new fuel cell flow field design is to improve the fuel cell performance through new geometry of fuel cell air delivery plate. The fuel cell performance, or current density can be improved by enhancing the oxygen concentration of the oxidant air stream at the MEA cathode side surface within the air channel. Therefore, oxygen concentration is used in the simulation to predict and access the fuel cell performance for a given new geometry design.

From the plate physical prototype experiment discussed in previous section, the added rib structure in the fuel cell air flow channel can improve the fuel cell efficiency. The mechanism for this improvement can be grouped to two aspects: (1) the rib produces the eddy in the flow channel, which induces the depleted oxygen distribution rearranged, so that the reaction MEA interface can have higher oxygen concentration compared to non rib structure; (2) improved oxygen concentration in the otherwise oxygen depleted area of the flow field generates higher current and better current distribution, making the overall current density increase.

3.4.2 Mathematical Model for the CFD Simulation

The air and hydrogen transports in the flow channel are considered as non-isothermal (heat transfer) flow. The mass transfer model is used to simulate the gas consumption from the fuel cell reaction, which is related to the current density of the fuel cell. Navier Stokes equations are used for simulating laminar flows in the channel duct. The simulation is subject to the temperature and velocity boundary conditions. These models are based upon the following equations.

Navier Stokes equations used in the CFD model include:

Continuity equation:

$$\frac{\partial \rho}{\partial t} + \nabla \cdot (\rho U) = 0 \tag{3-2}$$

Momentum equation:

$$\frac{\partial \rho U}{\partial t} + \nabla \cdot (\rho U \otimes U) = B + \nabla \cdot \sigma \tag{3-3}$$

where, velocity $U=U(\mathrm{u, v, w})$, and stress tensor

$$\sigma = -p\delta + (\zeta - \frac{2}{3}\mu)\nabla \cdot U\delta + \mu(\nabla U + (\nabla U)^T)$$

Compressible non-isothermal (heat transfer) energy equation:

$$\frac{\partial \rho H}{\partial t} + \nabla \cdot (\rho U H) - \nabla \cdot (\lambda \nabla T) = \frac{\partial p}{\partial t} \tag{3-4}$$

where, $H = h + \frac{1}{2}U^2$, plus $\rho = \rho(T, p)$, and the constitutive equation $h = h(T, p)$.

This model is completed by adding the following state equation for perfect gas A (oxygen) $\rho_A = \frac{pW_A}{RT}$ and $h_A = C_{pA}(T - T_{ref})$, where W_A and C_{pA} are mole weight and specific heat, respectively.

The mathematical model used in the computational fluid dynamics (CFD) to simulate oxygen reaction in fuel cell operation is the mass convection-diffusion equation:

$$\frac{\partial \rho Y_A}{\partial t} + \nabla \cdot (\rho U Y_A) - \nabla \cdot (\Gamma_A \nabla Y_A) = Source \tag{3-5}$$

where, the Y_A is mass fraction of species A (here represents oxygen) in a given fluid mixture; the mixture is considered as oxygen and all other union. The velocity U is obtained from the solution of the Navier Stokes equations, which refer to Equations 3-2 to 3-4; the *Source* is the mass sink term, representing the oxygen reaction and consumption in MEA:

$$\dot{M} = -\frac{iA_{MEA}}{4F} \times (32 \times 10^{-3}\ kg/mol) \tag{3-6}$$

The inlet velocity is calculated with:

$$u_{in} = \dot{V}/A_{in} \text{ and } \dot{V} = \xi_{O_2,in} \frac{iA_{MEA}}{4F} \times \frac{RT}{x_{O_2,in} p} \tag{3-7}$$

where, $\xi_{O2,in}$ is the stoichiometric flow ratio, A_{in} is the cross section area of channel inlet, A_{MEA} is the interfacial area between channel and MEA, F is the Faraday constant, i is the current density, $\dot{M}$ is the mass consumption rate of oxygen due to reaction in MEA, R is the universal gas constant, T represents temperature, $x_{O_2,in}$ is the oxygen mole fraction at channel inlet, p represents fluid pressure, and ρ is the mass density of the fluid air.

A powerful CFD code, CFX is used to carry out the model simulation, based upon Equations 3-2 to 3-5. The CFD model covers: (a) compressible laminar flow, (b) non-isothermal effects reflecting heat transfer between flow fluid and solid wall, and (c) mass transfer on the channel-MEA interface.

3.4.3 CFD Simulation Result and Discussion

The CFD simulation deals with multi-component airflow. The stylized two ribs geometry model used in CFD simulation is illustrated in Figure 3-6.

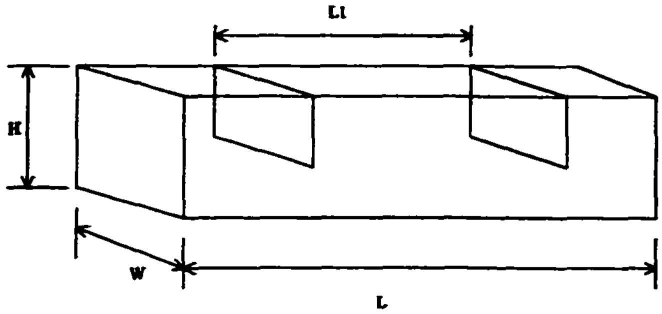

Figure 3-6 Flow channel geometry model

In this model, the chosen dimensions and model parameters are shown in Table 3-1.

Table 3-1 CFD model dimensions and related parameters

Name	Value
Rib spacing, L_l	50 *mm*
Model length, L	100 *mm*
Model width, w	1.5 *mm*
Model height, H	0.8 *mm*
Initial inlet pressure, P_{in}	3 *atm*
Initial inlet temperature, T_{in}	90 ^oC
Initial wall temperature, T_{wall}	80 ^oC
Current density, i	1 A/cm^2
Stoichiometric flow ratio at channel inlet, $\xi_{O2.in}$	2
Inlet oxygen fraction, $y_{O2.in}$	0.218
Constant specific heat for oxygen, C_{pA}	942 J/kg^oC
Mass transfer coefficient of oxygen, Γ_A	2.82e-6 $kg/m\cdot s$

The other dimensions, which do not appear in the Figure 3-6, include rib thickness, t, rib angle to the wall, θ, and rib height, h. additional design configurations [Dong 1999] of different rib geometry (t, θ, h) can be considered. In this study, we choose $t = 1$ *mm*, $\theta = 90^o$, and $h = 0.4$ *mm*.

The oxygen concentration monitoring point is set under the first rib on the left. The result on oxygen mass fraction is listed and compared with the results of smooth flow channel, as given in Table 3-2.

Table 3-2 Oxygen enhancement comparison

	Oxygen mass fraction y_{O2}	**Oxygen enhancement** (%)
Uniform duct	0.08494	0
One rib duct	0.1064	25.3
Two ribs duct	0.1778	112

The added rib structure has considerably improved the oxygen concentration at MEA interface. The two rib structure has more improvement on oxygen concentration, compared to the one rib. This result suggests add additional ribs along the flow channel to enhance the oxygen concentration for improving the fuel cell performance.

Chapter 4. Fuel Cell Plate Strength Analysis and Verification

In the previous chapter, physical and numerical or virtual prototype has showed that the fuel cell plates with rib added flow channels have better fuel cell performance. The new design can be easily manufactured using the screen-printing layer deposition process. This chapter will discuss the structure issues of the fuel cell plates and their design and strength analysis using finite element numerical method.

The finite element structure analysis in this study plays key roles on both virtual prototyping and physical prototyping. On virtual prototyping aspect, the finite element analysis provides the functional performance on the geometry design through the design optimization. On the materials issue of physical prototyping, the finite element stress analysis provides mechanical performance standard in materials development.

The common usage of finite element analysis on material mechanics and structure mechanics concentrates on the prediction and verification. These include performance and reliability of materials or structure. The finite element analysis in this study covers prediction and verification, as well as design optimization.

4.1 Three Dimensional Channel Layer Structure Model

The added structure layer fuel cell channel suffers the similar issues as the application of surface mounting and thin film in the electronic industries. These include structure stress, strain and thermal stress field. The stress or strain induced failure directly affects the reliability of structure and the performance of the system. Structure analysis plays a key role in structure design.

The finite element analysis model is used to calculate the stress and strain in the printed channel wall with the assumption of a good adhesion between the building layer and the substrate. The model consists of a solid substrate (graphite or coated metal) with a "printed" flow-field channel wall layer (polymer-based composites). A uniform steady temperature distribution is assumed at any temperature step. The zero stress state or the initial condition for the calculation is at room temperature. The temperature of the entire plate is raised up to 80°C to simulate the working condition of the PEM fuel cell. Meanwhile the fuel cell plate structure is also subject to inner channel pressure and top assembly structure loads.

Thermal stress is induced by the heating process due to the mismatch of the substrate and the printed channels with different thermal expansion coefficients. Since the polymer and polymer composites are quite thermal sensitive within the stated temperature range, nonlinear finite element analysis might be needed. The calculation is carried out by first using a linear finite element model, then to determine whether geometry non-linearity and/or materials non-linearity needs to be applied, and to calculate again if a nonlinear model is needed. For the fuel cell application, the plate has to undertake repeated temperature loads and structure loads. Both linear and nonlinear analyses are thus based on the elasticity assumption.

One significant issue in the structure model is that the composite material used in this study itself is also being developed. Due to the rigorous chemical stability and conductivity requirements of the plate, graphite and carbon are major ingredient materials for the substrate and the flow channels with different binders, leading to different thermal expansion rates and thermal stress. The structure is subject to the similar issues faced by surface mounting and thin film deposition in the electronic industries [Pirondi 1998]. The stress or strain will induce failures that directly affect the reliability of the printed plates [Shi 1995] and its ability to delivery fuel and oxidant gas in fuel cell operation. The unknown composite material during the design determines that the structure design has to follow a special procedure used in this study.

Linear stress-strain relation is expressed as:

$$\{\sigma\} = [D]\,\{\varepsilon^{el}\} \qquad (4\text{-}1)$$

where, $\{\sigma\}$ is the stress vector = $[\sigma_x\ \sigma_y\ \sigma_z\ \sigma_{xy}\ \sigma_{yz}\ \sigma_{xz}]^T$, [D] represents elasticity matrix, $\{\varepsilon^{el}\} = \{\varepsilon\} - \{\varepsilon^{th}\}$ is the elastic strain vector, $\{\varepsilon\} = [\varepsilon_x\ \varepsilon_y\ \varepsilon_z\ \varepsilon_{xy}\ \varepsilon_{yz}\ \varepsilon_{xz}]^T$ is the total strain vector, $\{\varepsilon^{th}\} = \Delta T\ [\alpha_x\ \alpha_y\ \alpha_z\ 0\ 0\ 0]^T$ is the thermal strain vector, and α_x is the thermal coefficient of expansion in the *X* direction.

$$\Delta T = T - T_{REF} \tag{4-2}$$

where, T is the current temperature at the point in question, and T_{REF} is the reference (strain-free) temperature.

The nonlinear elastic materials are modeled with multi-linear, stress-strain relation. The nonlinear simulation is performed with gradually increasing load from initial value to final value. The load step and sub-steps are defined associated with the nonlinear analysis to ensure the convergence of the simulation. The finite element codes ANSYS and Pro/MECHANICA are used for the structure analysis.

4.2 Solid Modeling of Printed Plates

The parametric solid model of the printed flow channels of the gas delivery plate, generated using Pro/ENGINEER, is constructed as a rectangle-shaped building layer structure, as shown in Figure 4-1. The key design parameters of this solid model include: thickness of the printed layer, *H*, channel wall thickness *W*, and channel length, *D*. These parameters are used later as variables in the design optimization. A Pro/ENGINEER model of a prototype fuel cell gas delivery plate, including building layer and substrate, is illustrated previously in Figure 3-5. These CAD models are used to generate the mesh for finite element analysis program ANSYS or Pro/MECHANICA for structure analysis.

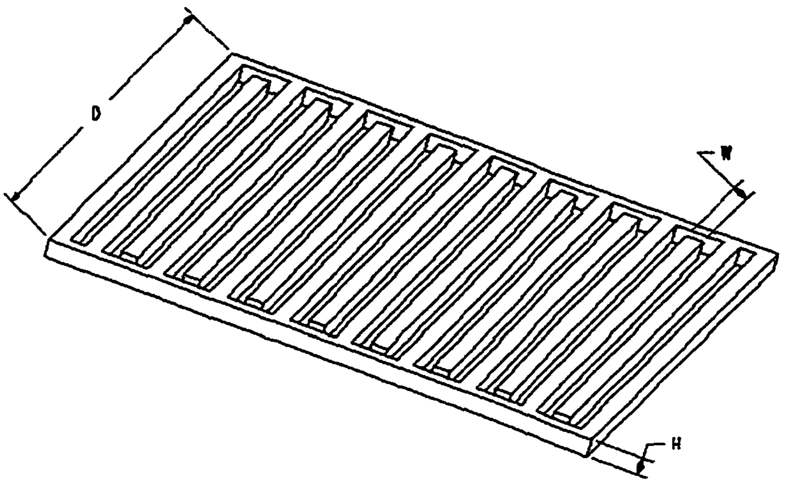

Figure 4-1 Parametric solid model of the printed fuel cell flow field layer

Solid model generation using Pro/ENGINEER CAD system has considerable advantage compared to direct modeling using finite element tool ANSYS. Pro/ENGINEER allows a user to generate a more complex geometry within a short time. The solid models, shown in Figure 3-5 and Figure 4-1, are quite simple for Pro/ENGINEER. In ANSYS, dozens of steps of graphical definition or dozens of coding sentences would be needed to specify the part geometry.

Transformation from the Pro/ENGINEER solid model to finite element model can be performed through the integrated Pro/MECHANICA finite element analysis function module. The model can then be used to define loads and boundary conditions. When transferring to ANSYS finite element model, an external package, called Pro/MESH, is needed to complete this procedure. Additional modification might be needed before the analysis is carried out using ANSYS finite element program.

The advantage of using Pro/MECHANICA lies on its full integration with Pro/ENGINEER. The finite element analysis with Pro/MECHANICA, including design optimization, can be carried out and the design can be modified within Pro/ENGINEER. The drawback of Pro/MECHANICA is its limitation to only linear analysis and its slow computation due to the need of certain CPU time and RAM to support its CAD system. The Pro/MESH program transfers a Pro/ENGINEER model to an ANSYS model only in one direction without capability to transform back. This is very inconvenient for the modification of the design model. However, the fast computation allows ANSYS to analyze much more complex model.

At present, finite element codes combining with CAD model, such as ANSYS with Pro/ENGINEER, present one of the most convenient virtual prototyping tools.

4.3 Linear and Nonlinear Structure Analysis

The geometry models in Figures 3-5 and 4-1 generated with Pro/ENGINEER, are transferred to Pro/MECHANICA and ANSYS for finite element structure analysis. The model is used on both linear and nonlinear materials elasticity analysis. The simulation is subject to load of gas pressure applied to the inner channel, the uniform stack compression pressure from the end plates, and the thermal load from temperature field.

The design parameters come from two areas. For the epoxy-type composite building layer, $D = 0.055626$ *m*, $W = 0.001651$ *m*, $H = 0.001778$ *m*; mass density $\rho = 1299.52$ kg/m^3, Young's modulus $E = 3$ *GPa*, Poisson's ratio 0.37, and coefficient of thermal expansion 6e-5 m/m^oK. For stainless steel substrate in Figure 3-5: side length $D_s = 0.055626$ *m*, thickness $H_s = 0.001778$ *m*, Young's modulus $E_s = 193$ *GPa*, Poisson's ratio 0.37, and thermal expansion coefficient 1.728e-5 m/m^oK.

The automated meshing of Pro/MECHANICA produces 801 and 1260 four node tetrahedral elements for the models shown in Figures 4-1 and Figure 3-5, respectively. Three sets of simulation are performed using linear analysis with Pro/MECHANICA:

(1) Layer model only, fixed bottom boundary condition, 204 *kPa* inner channel pressure and 544 *kPa* uniform top pressure, without temperature field.

(2) Layer model only, fixed bottom boundary condition, 204 *kPa* inner channel pressure and 544 *kPa* uniform top pressure, with 80°C temperature field.

(3) Layer embedded on solid stainless steel substrate, fixed bottom boundary condition on substrate, 204 *kPa* inner channel pressure and 544 *kPa* uniform top pressure on layer, with 80°C temperature field.

The simulation results are shown in Table 4-1. The simulation costs about 4 to 6 minutes to converge on a PII 450 MHz PC.

Table 4-1 Results from linear structure analysis using Pro/MECHANICA

FEA Model test	Max Stress (*MPa*)	Max displacement (*μm*)	Comment
(1)	1.4 (epoxy)	0.62 (epoxy)	Safe
(2)	47.9 (epoxy)	14.7 (epoxy)	Unsafe on stress
(3)	<20 (epoxy) 560 (steel)	17.8 (epoxy)	Safe on epoxy stress Unsafe on steel stress

The influence of temperature field plays a key role on the stress level of the structure comparing tests (1) and (2). In test (2), the epoxy material is working at a high stress level close to its ultimate stress range (50-60 *MPa*), which will cause creep at this high temperature. The test (3) shows that the maximum Von Mises stress on the whole structure, including layer and substrate, is 560 *MPa* at the fixed bottom area of the substrate. This stress is within the ultimate stress range of stainless steel, 500~600 *MPa*. This calculation results are not consistent with our experiments, in which the fuel cell flow field plate has never shown any signs of failure in the substrate (either steel or graphite) under the elevated temperature range, while some damages appeared on the building layer. The calculated max stress of 48 *MPa* for epoxy in test (2) and 560 *MPa* for steel in test (3) indicates that high stresses and the fixed bottom constraint design should be avoided. In addition, the temperature field effect generates a relatively high maximum displacement on the epoxy. Material deformation needs to be closely monitored in the design and manufacturing of the epoxy layer. The stress distribution and displacement profile from test (2) are shown in Figures 4-2 and 4-3.

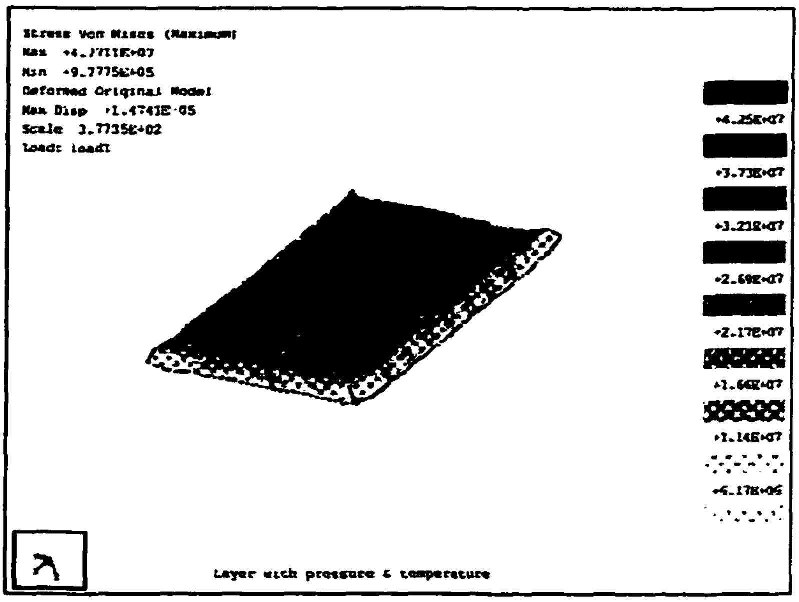

Figure 4-2 Stress distribution of building epoxy layer from test model (2)

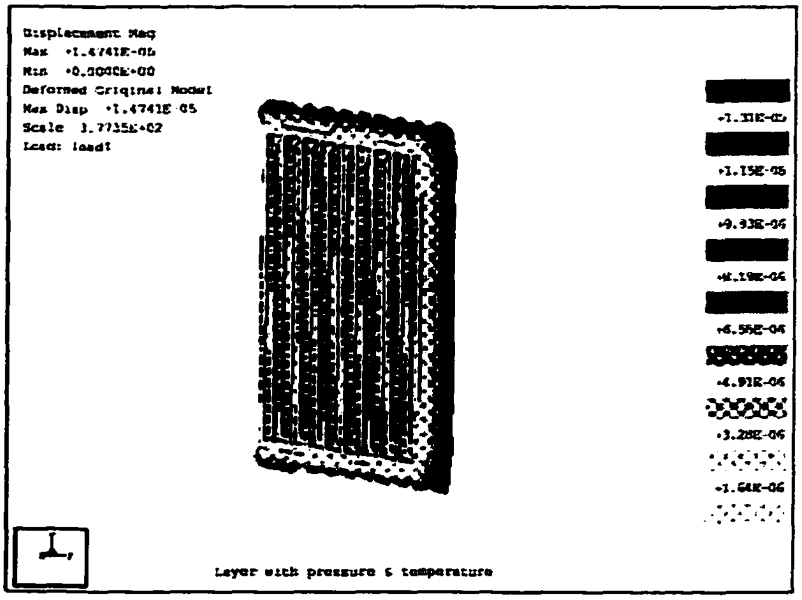

Figure 4-3 Displacement profile of building epoxy layer from test model (2)

The geometry model in Figure 4-1, generated using Pro/ENGINEER, is transferred to ANSYS to form the finite element analysis model for both linear and nonlinear structure analysis. In addition to the given design parameters, quadratic 10 node tetrahedral elements, called SOLID92, are used in the model. The element division along the longer and shorter wall sides are 16 and 6 respectively, and the spacing ratio is –2. A total of 13469 elements are generated with higher element density in the end and corner areas.

The finite element model based on elasticity is a conservative system, assuming not influenced by the loading history. Due to the complex geometry of the plate, the FEA model needs 12400 to 13600 elements under the three geometry variables, *D*, *W*, *and H*, used in the design optimization to be discussed later. Moreover, some of these elements have high aspect ratio and large element edge angle (e.g. >165°), and the model is subject to joint temperature and structure loads. Therefore different load steps and substeps are necessary to achieve good convergence. In the analysis, 5 or 10 substeps are needed for each load step. The equilibrium iteration is automatically determined by the ANSYS program.

The calculation is first carried out using linear material elasticity analysis. The simulated plate is subject to inner channel pressure load, uniform stack compression pressure from top, and thermal load from temperature field. The result using different data sets of the analysis is shown in Table 4-2. Test (4) of this linear analysis is carried out with pure structure loads, including the fixed bottom boundary condition, 204 *kPa* inner channel gas pressure, and 544 *kPa* uniform stack compressing pressure, without a temperature field. Test (5) of the linear analysis covers only temperature load with the fixed bottom boundary condition, and an 80°C temperature field increased from the room temperature at 20°C, without any structure loads. Test (6) includes both structure and temperature loads: fixed bottom boundary condition, 204 *kPa* inner channel pressure, 544 *kPa* uniform compressing pressure, and a thermal load from 80°C temperature field increased from 20°C room temperature.

Table 4-2 Linear and nonlinear structure analysis with ANSYS

FEM Model Test	Max von Mises Stress (*MPa*)	1st Principal Strain ($\mu\varepsilon$)	Max Displacement (μm)	Comment
(4) Structure loads only	1.24	271	0.495	Safe
(5) Temperature load only	45.5	11344	13.1	Unsafe
(6) Structure and temp. loads	48.7	12049	15.8	Unsafe
(7) Temperature pre-stress	46.7	11605	13.3	Unsafe
(8) Nonlinear	17.74	9127	13.5	Safe

According to the results from tests (4) and (5) of Table 4-2, the temperature induced thermal stress is much higher than that of the structure loads. In test (5), the epoxy-based composite material is working at a high stress level quite close to the material strength of 50-60 *MPa*. This will cause creep at the elevated temperature. In addition, the temperature field also generates relatively high maximum displacement and strain. Tests (4)~(6) show that the temperature field plays a key role on the induced maximum stress and strain within the structure, which are same as those results from Pro/MECHANICA.

During fuel cell operation, there is no fixed order in which temperature load is applied or structure loads are increased. In general, a higher loading stress has much more influence on the subsequent loading, compared to a lower loading stress. Thus, the temperature field is first applied to generate temperature pre-stress, followed by the structure loads to simulate the worst-case working condition, as model test (7).

The temperature pre-stress simulated by test (7) is carried out through two load steps. The first temperature-loading step is applied gradually from room temperature of 20°C to 80°C. Then the second structure-loading step is performed by gradually increasing the inner channel pressure and uniform compressing pressure from zero to 204 *kPa* and 544 *kPa*, respectively. Both load steps use 10 substeps to simulate the gradually increasing loads.

According to the results from test (6), the maximum strain level is 12049 $\mu\varepsilon$, less than 2%. The maximum displacement is 15.8 μm, which is only 0.96% of the shortest dimension, wall thickness W. Thus, no geometry nonlinearity needs to be considered in the model. However, the fix bottom boundary condition provides a strong constraint. Therefore the stress stiffness effect, associated with nonlinear geometry, is considered at temperature pre-stress simulation in the model test (7) for more accurate analysis. The results show that the temperature pre-stress effect has 4.1% and 3.7% decrease on the maximum stress and strain, respectively, compared to the results from model test (6). Based upon these analyses, tests (1) to (7), the high stress predicted by the linear model, or introduced by the selected plate structure and/or material, is undesirable.

One of significant issues for epoxy-based materials operating at 80^oC is the nonlinear stress-strain relation. The elasticity analysis of the nonlinear material focuses on nonlinear stress-strain relation instead of a single Young's modulus. The stress-strain relation, as a material performance characteristics input, is constructed using multiple linear segments, with the initial slope equal to the Young's modulus, and the rest segments following a series of line segments with decreasing slopes. For generality, the ratio of the original and following slopes of these line segments are 100%, 98%, 94%, 90%, 85%, 80%, etc. of the Young's modulus of 3 *GPa*. The nonlinear materials elasticity simulation of model test (8) follows the same boundary and loading conditions as the model test (6) that has been previously discussed.

The simulation applies one load step with several substeps. The nonlinear material simulation is constructed with a series of converged, linear analysis. The numbers of equilibrium iterations and load substeps are balanced to achieve the best accuracy within a short computation time. Additional load substeps will generate more accurate result, but requiring longer computation time. Less load substeps may also need more computation time, because each substep has a larger load change, and requires a lengthy equilibrium iteration for the step to converge. Ten load substeps are used in this simulation.

The nonlinear materials elasticity analysis of model test (8) in Table 4-2 produces a maximum von Mises stress 17.74 *MPa*, a 1st principal total strain 9127 με, and a maximum displacement 13.5 μm. These are within the working range for epoxy materials. The simulation also indicates that both of the maximum stress and maximum strain occurs at the fix corner and channel/wall ends, for all loading conditions. The stress and strain distribution from nonlinear analysis of model test (8) is shown in Figures 4-4 and 4-5.

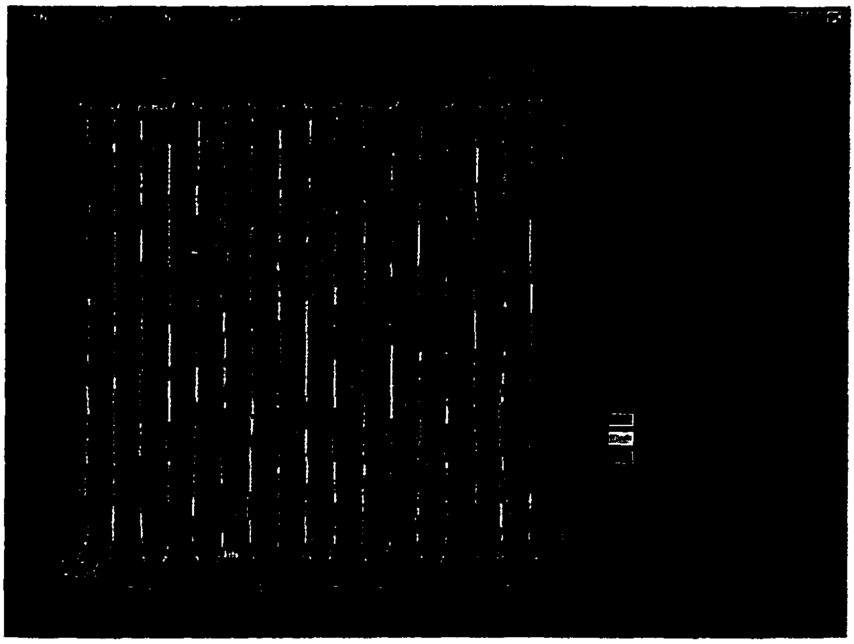

Figure 4-4 Stress distribution of nonlinear model test (8)

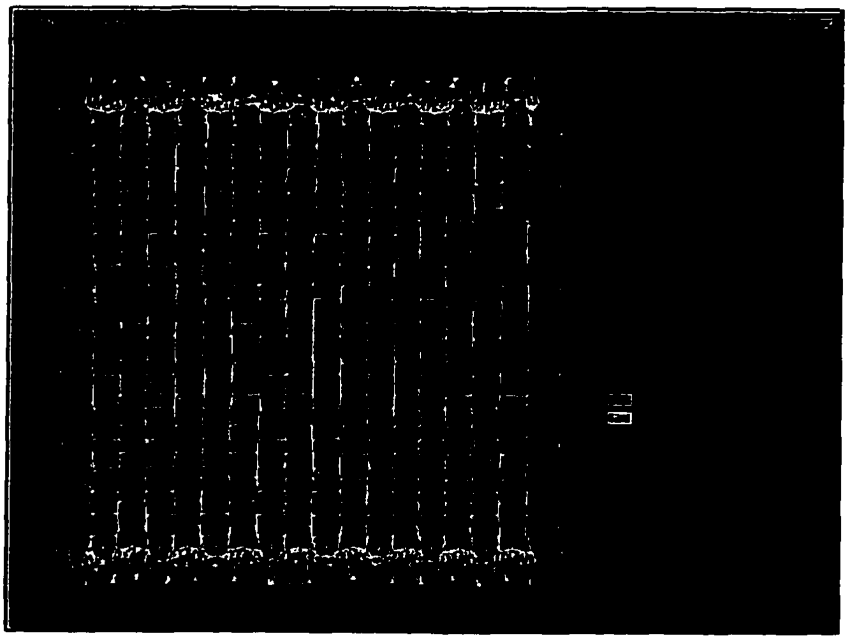

Figure 4-5 Strain distribution of nonlinear model test (8)

In summery, the finite element analysis models illustrate that high stress is induced by the temperature load. Material nonlinearity needs to be considered in the structure design. In addition, the corner effect of maximum stress and strain is also important for the geometry design consideration.

Chapter 5. Thermal Analysis of Printed Plates

The science of thermodynamics deals with the relation between heat and other forms of energy, while the science of heat transfer concerns with the analysis of the rate of heat transfer taking place in a system. Since energy transfer by heat flow cannot be measured directly, the related physical quantity, temperature, is measured to access the energy flow. Once the temperature distribution in a system is obtained, the heat flux can be determined from the law relating the heat flux to the temperature gradient.

When fluid flows over a solid body or inside a channel made of a solid material and the temperature of the fluid and the solid surface are different, convection heat transfer between the fluid and the solid interface will influence the fluid motion relative to the surface. The forced convection of flowing fluid is maintained under the forces induced by a pump or a fan.

5.1 Heat balance of PEM fuel cell

Fuel cell reaction can be expressed as

$$H_{2\,(g)} + \tfrac{1}{2}\, O_{2\,(g)} \longrightarrow H_2O_{\,(l)} \tag{5-1}$$

A fuel cell operates on gaseous phase hydrogen and oxygen, and produces liquid phase water. The total energy produced in a fuel cell, E_{total}, includes the electric power, P_v and absorbed heat Q.

$$E_{total} = \dot{Q} - P_v \tag{5-2}$$

This total energy can be expressed as

$$E_{total} = r \cdot \Delta H \tag{5-3}$$

where, ΔH is the enthalpy change caused by the electrochemical reaction, and r is the reaction rate of the cell. With current density, i, the reaction rate can be expressed as

$$r = \left|\frac{i}{ZF}\right| \tag{5-4}$$

where, the Z is charge number, which can be positive or negative; F is the Faraday constant $F = 96486\ C/mol$.

The rate at which heat is produced can thus be calculated as

$$\dot{q} = \left|\frac{i}{ZF}\right| \Delta H + p_v \tag{5-5}$$

where, $p_v = P_v/A$, and $\dot{q} = \dot{Q}/A$, represents the electric power density of the fuel cell and heat flux from MEA reaction area respectively.

Using the power density for the reversible process [Lampinen 1993] as:

$$p_v = \left|\frac{i}{ZF}\right|(-\Delta G) = \left|\frac{i}{ZF}\right|\varepsilon \tag{5-6}$$

and for the irreversible (real) process [Lampinen 1993] as:

$$p_v = \left|\frac{i}{ZF}\right|(-\Delta G) - |i||\eta| = \left|\frac{i}{ZF}\right|\varepsilon - |i||\eta| \tag{5-7}$$

where, the ε is the half cell electrical work and the η is the voltage drop due to ohmic losses and reaction resistances.

Using the relation of

$$\Delta H - \varepsilon = \Delta H - \Delta G = T \cdot \Delta S \tag{5-8}$$

the Equation 5-6 for reversible process is expressed as:

$$q = \left|\frac{i}{ZF}\right|(\Delta H - \Delta G) = \left|\frac{i}{ZF}\right| T\Delta S \qquad (5\text{-}9)$$

and the Equation 5-7 for irreversible (real) process as:

$$q = \left|\frac{i}{ZF}\right|(\Delta H - \Delta G) = \left|\frac{i}{ZF}\right| T\Delta S - |i||\eta| \qquad (5\text{-}10)$$

Equation 5-10 is used to calculate the heat generated during real fuel cell operation. The thermal analysis of fuel cell plates are based on the heat generated from this source.

The heat flux from fuel cell reaction based on the cathode reaction can be expressed as

$$O_2 + 4H^+ + 4e^- \Leftrightarrow 2H_2O \qquad (5\text{-}11)$$

For this reaction, the charge number $Z = 4$, the fuel cell operates at temperature 80 ^oC (353 ^oK), the entropy change ΔS is -326.36 $J/mol\cdot{}^oK$, and enthalpy change ΔH is -6229.6×10^3 J/mol [Lampinen 1993].

The power produced by a single fuel cell at cathode is obtained from several points of the polarization curve, and these points have the operating voltage and current density of: (0.82*v*, 0.08A/cm^2), (0.75*v*, 0.27A/cm^2), (0.7*v*, 0.5A/cm^2), (0.6*v*, 0.75A/cm^2) and (0.5*v*, 0.93A/cm^2) [Kratschmar 2001]. The real heat flux generated based on the Equation 5-10 is calculated and shown in Table 5-1, including the calculation results based on the reversible process consideration of Equation 5-9 and the voltage drop η based on the reversible electrical cell potential of 1.23 *V* [Kratschmar 2001]. The negative sign of heat flux indicates heat flow from MEA cathode reaction surface to the neighboring plate. The relations of heat flux vs. operating voltage and current density is shown as Figures 5-1 and 5-2, respectively. More heat is generated with higher current density and lower operating voltage. The power density vs. current density is shown in Figure 5-3.

Table 5-1 Heat flux result for a half single cell

Operating voltage, (*V*)	0.82	0.75	0.7	0.6	0.5
Current density (A/cm^2)	0.08	0.27	0.5	0.75	0.93
Voltage drop η (*V*)	0.41	0.48	0.53	0.63	0.73
Reversible heat flux ($J/s{\cdot}cm^2$)	-0.0234	-0.0788	-0.146	-0.219	-0.2716
Real heat flux ($J/s{\cdot}cm^2$), q	-0.0562	-0.2084	-0.411	-0.6915	-0.9505
Power density (w/cm^2), p_v	0.0656	0.2025	0.36	0.45	0.465

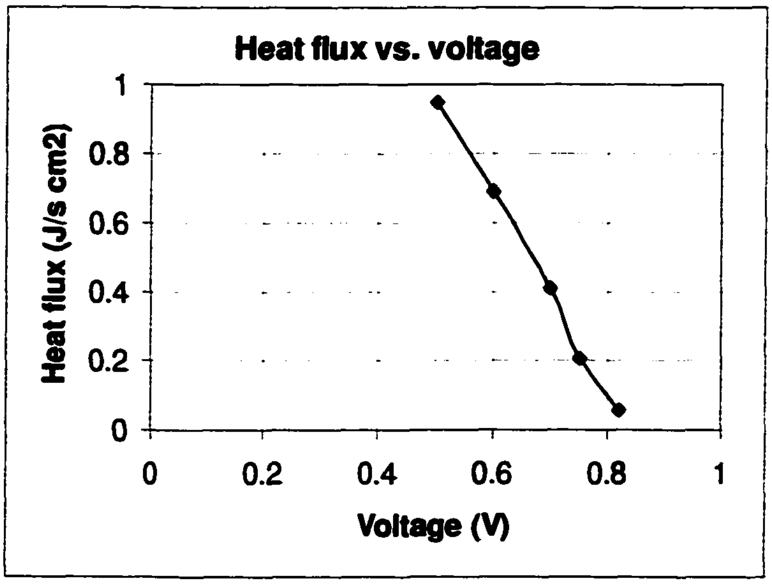

Figure 5-1 Heat flux from MEA vs. voltage output

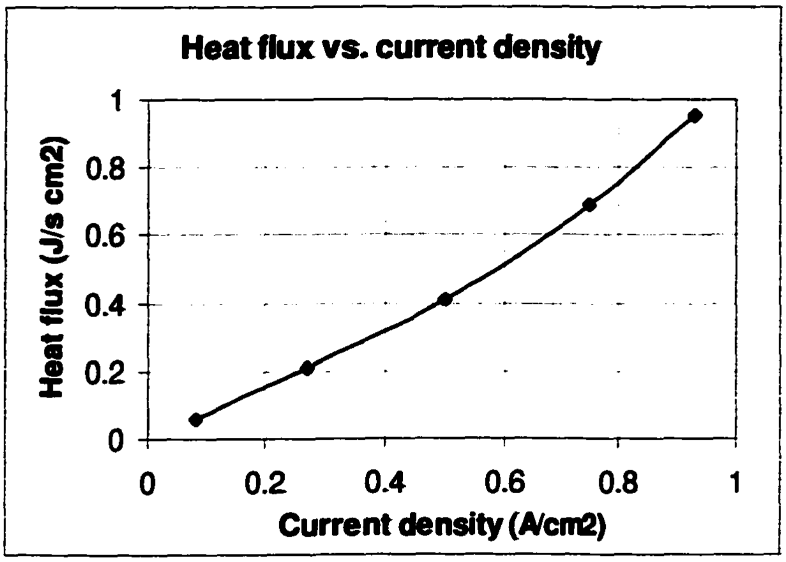

Figure 5-2 Heat flux from MEA vs. current density

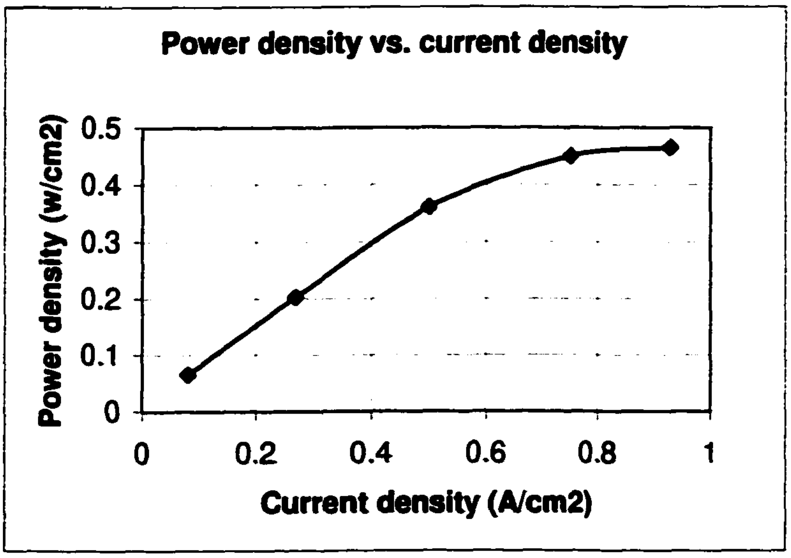

Figure 5-3 Power density vs. current density

In summary, for the fuel cell plate thermal balance consideration, the waste heat generated by the fuel cells will increase at the rates indicated by Figures 5-1 and 5-2, with the increase of current density or decrease of cell/stack operating voltage, as the operating point moves from left to the right in the polarization curve. The two figures are correlated by the polarization curve, increased current density and decreased voltage reduces the fuel cell efficiency and increases heat generation. The cell or stack power density also increases as current density increasing according to Figure 5-3 to certain level where it starts to decrease. The later region is not included in the curve. The difference between power density curve and heat flux curve produce the power density curve that shows a convex shape with a peak value, while the heat flux curve has a concave shape with its value increase faster and faster. These are qualitatively considered in designing the entire fuel cell system, including cooling.

From the fuel cell system point of view, when the current density is low and the voltage is high, the fuel cell system generates a modest amount of power. The system has low efficiency, due to the small power produced. When the current density is high and the voltage is low, the system power output increases slower than the heat generate. The ancillary devices will consume a large amount of energy to get rid of the large amount of heat. The system efficiency is still low. Therefore, an optimal operating point exist for a given fuel cell system. For fuel cell plate thermal consideration, both heat generation from MEA reaction and heat taken off through cooling should be considered.

5.2 Thermal Model of Fuel Cell Plate

The thermal analysis of fuel cell plate considers all three modes of heat transfer: conduction, convection and radiation. Based on the Stefan-Boltmann Law [Ozisik 1985], the radiation energy is proportional to area and $(T^4_{source} - T^4_{surronding})$, the temperature of the heat source and the surrounding environment. A PEM fuel cell operates at a relatively low temperature, 353 ^oK (80 ^oC), and the thermal radiation is mainly considered on the outer periphery of the plate (Figure 1-1) with small surface area. Due to the small surface area and temperature difference between the fuel cell stack and the surrounding atmosphere, the amount of heat rejected by the fuel cell through the plates is limited. Either a small portion, such as 10 percent of the waste heat is considered be rejected through radiation, or simply omitted. The later approach was adapted in this work for simplification.

The heat flow within the fuel cell plates comes in three forms. This can be illustrated using the hydrogen fuel plate shown in Figure 1-1 (a). The heat generated from the electrochemical reaction on the MEA transfers to the plate from the top surface, to which the heat flux surface load is applied. Inside of the flow field channels on the plates, heat is transferred from the solid channel wall of the plate to the passing gas through convection. Heat convection surface load is applied to the gas-wall interface. The bottom surface of plate connects to the cooling plate, which passes the excessive heat from the fuel cell to the cooling plate to be carried out by the cooling air to keep the fuel cell operate at the desired constant temperature 80 ^{o}C. Two assumptions are made when the boundary conditions on this bottom surface of the plate. The first assumes a constant temperature of 80 ^{o}C on the surface. The second uses a negative heat flux to reflect the rejection of heat from the plate. The geometric model of the fuel cell plate remains identical to the one used in structure analysis.

To predict the temperature distribution in the fuel cell plate, the accurate energy equation is written as:

$$\rho c\frac{\partial T}{\partial t}+\rho cV\cdot\nabla T=\nabla\cdot(K\nabla T)+\dddot{q} \tag{5-12}$$

where, the two terms on the left side of the equation represents the transient and advection factors, and the $\dddot{q}$ is the energy generation rate per unit volume. In this proposed model for the fuel cell plate, the chemical species and electronic charges are assumed to be in thermal equilibrium, the left two terms are thus neglected. The energy equation is then reduced to the three dimensional steady state conduction form of the Fourier's law:

$$\frac{\partial}{\partial x}(K_x\frac{\partial T}{\partial x})+\frac{\partial}{\partial y}(K_y\frac{\partial T}{\partial y})+\frac{\partial}{\partial z}(K_z\frac{\partial T}{\partial z})+\dddot{q}=0 \tag{5-13}$$

where, temperature, T, is an independent variable and is a function of the location of the point of interest, (x, y, z), and K_x, K_x, K_x are thermal conductivities along x, y, z directions.

The boundary conditions of the plate model include convection surface and temperature surface. The inner channel wall surface specifies the convection as:

$$\ddot{q}=h(T-T_b) \tag{5-14}$$

where, h is convection coefficient and T_b is the bulk temperature of the flow gas. The periphery surface of the plate is assumed to be adiabatic. The heat source term includes a constant heat flux from top surface, corresponding to the real heat flux discussed in Section 5.1.

The boundary conditions for the bottom surface consist of two parts, which consider the 80 ^oC operating temperature and the cooling heat sink separately. The first model assumes that the bottom surface of the plate has a constant temperature of 80 ^oC and the cooling effect is neglected. The second model assumes a negative heat flux from bottom to simulate the cooling effect. Thermal analysis using these two models is carried out using finite element codes ANSYS through the Pro/ENGINEER plate geometry model.

5.3 Thermal Simulation Results and Discussion

The heat transfer finite element analysis with ANSYS code, which deals with thermal effect of flow fluid or channel structure under convective load, temperature load and heat source is applied on the geometry model shown in Figure 4-1.

The flow channel plate dimensions include: D = 0.055626 m, W = 0.00153 m, H = 0.00158 m. A quadratic ten node tetrahedral thermal element with one degree of freedom temperature at each node, called SOLID87, is used for the model. SOLID87 is well suited to models of irregular meshes, produced from various CAD systems. The element is applicable to a three-dimensional, steady-state or transient thermal analysis. This SOLID87 element has the same feature as its equivalent structural element, SOLID92, with different element matrices. The element division along the long wall side is 16, along all other parts are 6, and spacing ratio is –2. Based on the given geometry, a total 12471 of elements is generated with higher mesh density at the end and corner areas.

The loading and boundary conditions used in the analysis comes from several areas. The heat generated from the electrochemical reaction in the MEA surface is represented by heat flux $q = 1200\ J/s{\cdot}m^2$ from the top surface of the plate corresponding to a high voltage and low current density working point as shown in Figures 5-1 and 5-2. Fluid convection in the flow channel is carried out with the bulk temperature $T_{bulk} = 90\ ^oC$. All periphery side boundaries of the plate are assumed to be insulated, which omitted the 10 to 15% heat released due to the radiation. The load is performed with one load step including 10 substeps. Other material coefficients of the printed plate include: specific heat $c = 1047.6\ J/kg{\cdot}\ ^oC$; mass density $\rho = 1299.52\ kg/m^3$; convective coefficient $h = 80\ J/s{\cdot}m^2{\cdot}^oC$; and thermal conductivity $k = 0.187599\ J/s{\cdot}m{\cdot}^oC$. Here, the value of the convective coefficient, h, depends on many influencing factors, including the material and geometry of the heat exchanger and the flow conditions of the cooling fluid. The determination of its value is beyond the scope of this research. The selected value is based on previous research to demonstrate this work.

The boundary condition on the bottom is considered with two cases separately in order to maintain the fuel cell operation at 80 ^oC. In the first case, the constant temperature, $T = 80\ ^oC$, is used, which ignore the dynamic cooling effect for the cooling plate. In the second case, a constant heat flux of negative value is applied to represent cooling effect. The maximum temperature from thermal analysis is monitored in order to avoid overheat in the fuel cell operation.

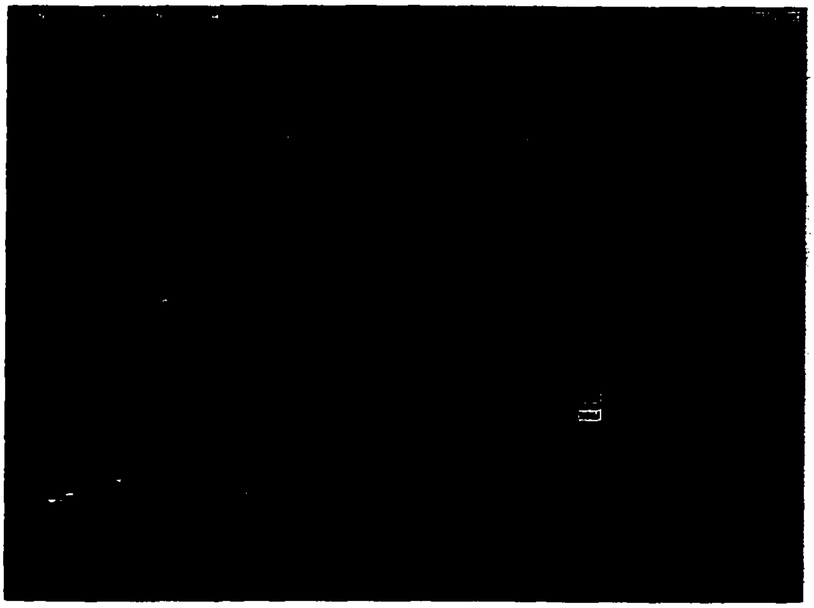

Figure 5-4 Temperature distribution with the bottom temperature 80 ^{o}C

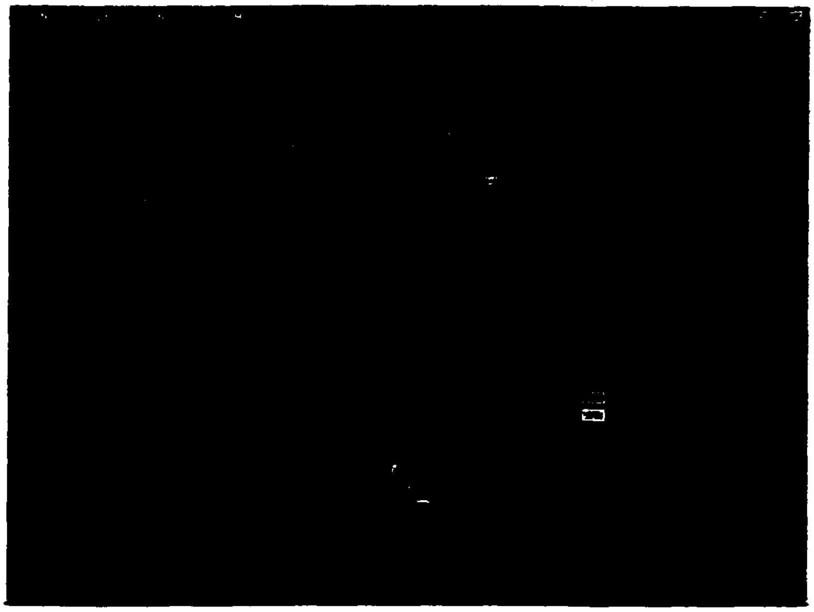

(a) Total heat flux

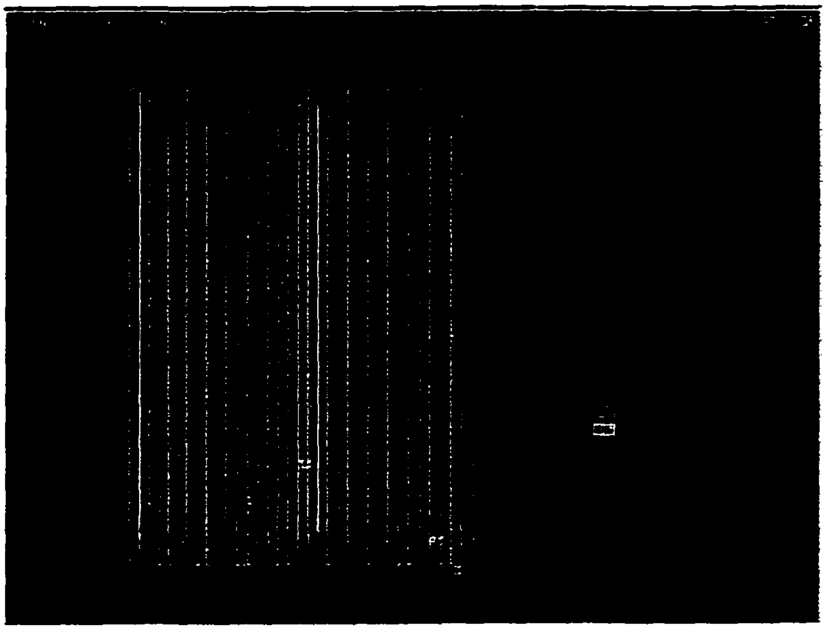

(b) Vector heat flux in *z* (thickness) direction

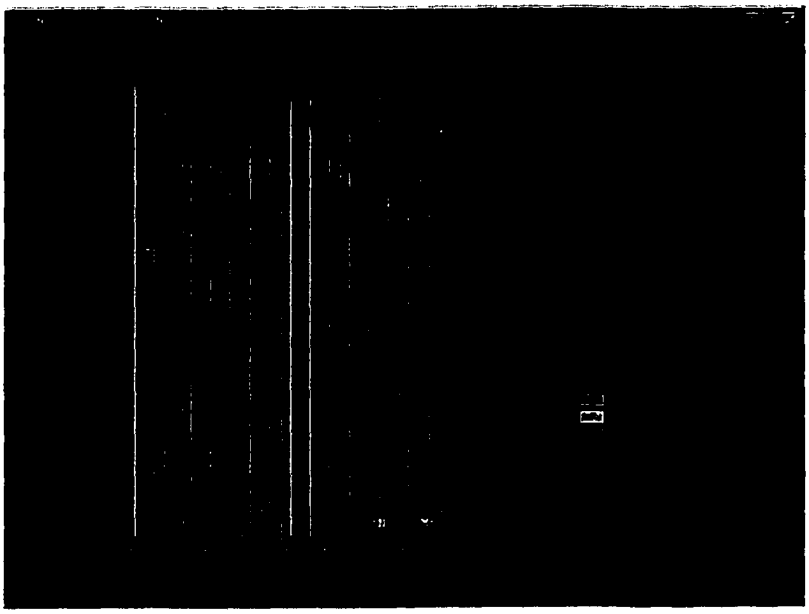

(c) Vector heat flux in *x* (cross-channel) direction

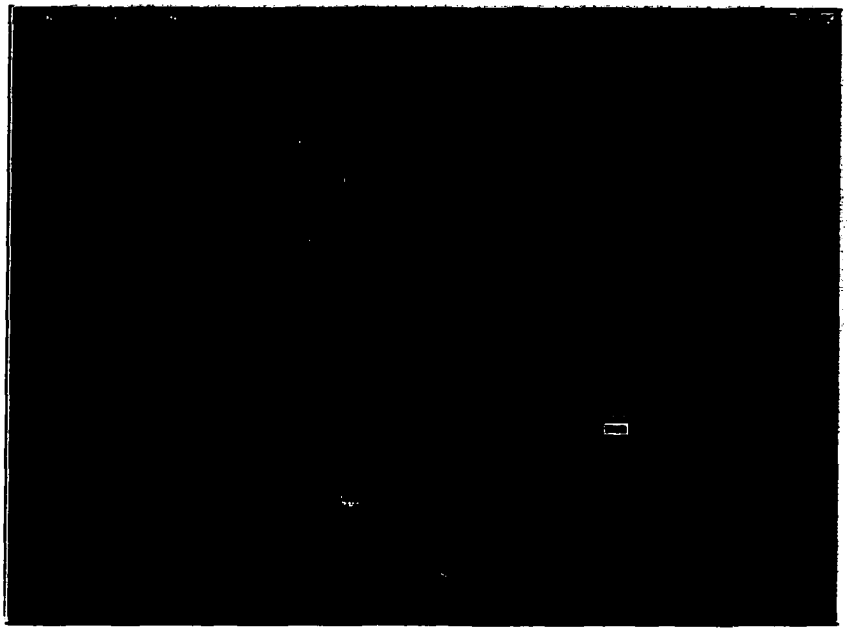

(d) Vector heat flux in *y* (channel) direction

Figure 5-5 Heat flux distribution with bottom temperature 80 ^oC

For the case of constant temperature, $T = 80\ ^oC$, at bottom, the temperature profile of Figure 5-4 shows that the maximum temperature appears at the top surface neighboring the MEA area (face up) reaches the maximum of 92.2 ^oC (365.2 ^oK) with uniform distribution. This is an overheated temperature, which may cause the polymer membrane aging, and needs to be avoided. The total heat flux profile in Figure 5-5 shows summation heat flux and vector heat flux along *x, y, z* directions. The value of heat flux along *z* (thickness) direction is much higher than *x* (cross-channel), *y* (channel) directions, which indicates good cooling effect to remove the extra heat from the plate. For all heat flux profiles shown in Figures 5-5 (a), (b), (c), and (d), higher heat values appear at the end of the channels.

For the first model with constant temperature $T = 80\ ^oC$ at the bottom, the *z* direction heat flux reaches its maximum to 3451 J/sm^2 at the bottom of the end of the channel walls.

Based on this result, the second model applies a constant heat flux of negative value at 3400 J/sm^2 to simulate the cooling effect.

The result of temperature distribution shown in Figure 5-6 represents a uniform temperature of about 340 ^oK at bottom and around room temperature 286 ~ 311 ^oK on plate periphery sides and corners. The maximum temperature still reaches to 87.5 ^oC (360.5 ^oK). The Figure 5-7 shows that x, y heat flux is higher on the periphery side area because they have relatively low temperature. The z direction still dominates the heat flux, which represents the cooling effect.

The simulation not only predicts the temperature distribution but also associates cooling to fuel cell plate in fuel cell stack and systems design. Since the heat removing is conducted with the help of active cooling, the heat flux cooling is more practical even the maximum temperature is still at 87.5 ^oC (360.5 ^oK) for the given geometry.

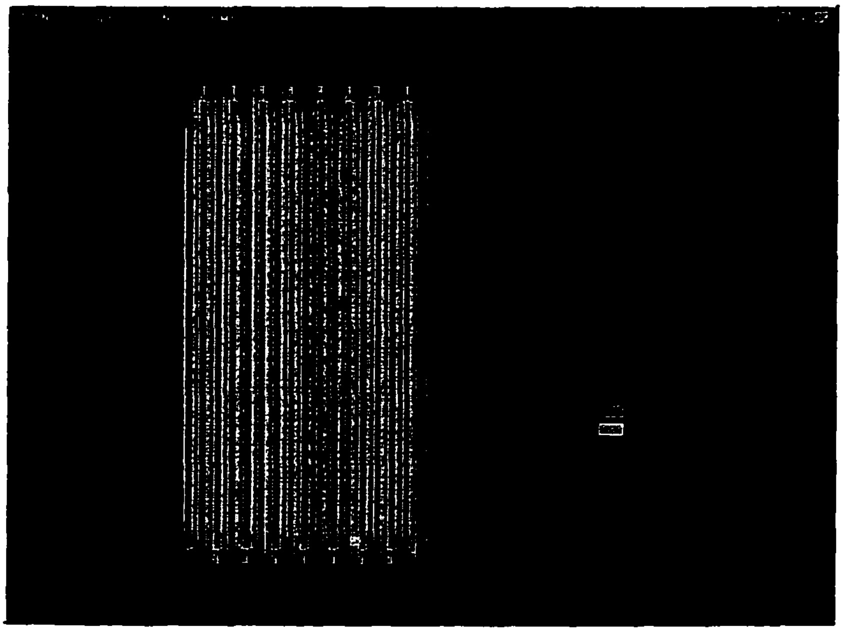

Figure 5-6 Temperature distribution with constant heat flux 3400 $J/s{\cdot}m^2$

(a) Total heat flux

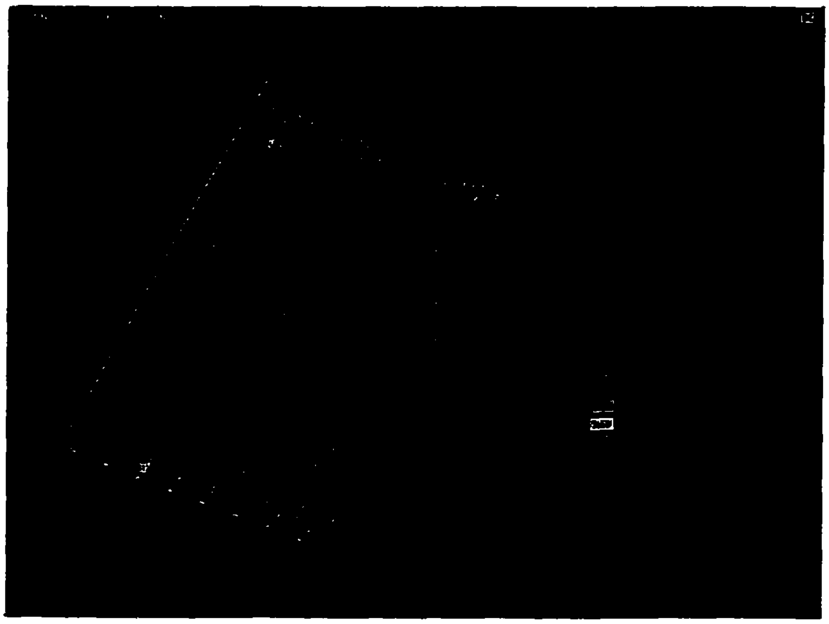

(b) Vector heat flux in *z* (thickness) direction

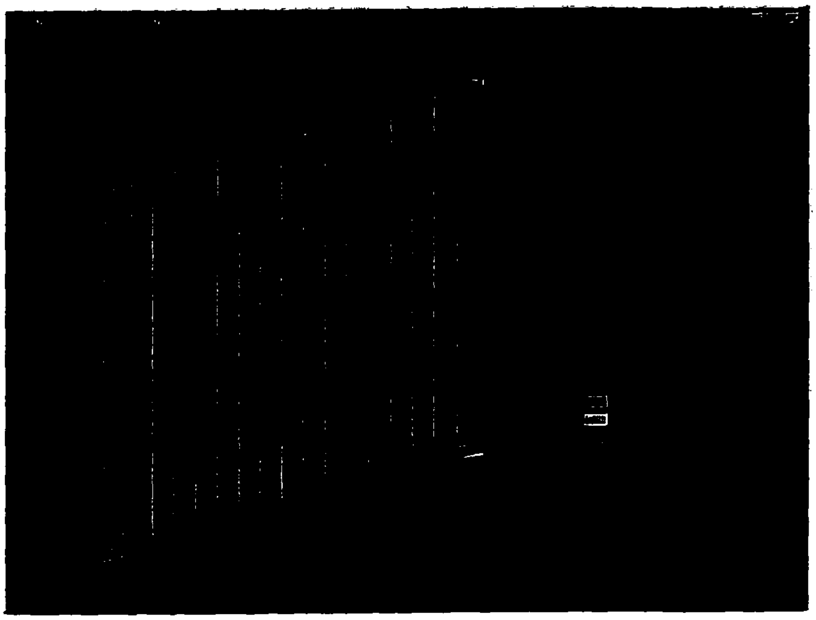

(c) Vector heat flux in *x* (cross-channel) direction

(d) Vector heat flux in *y* (channel) direction

Figure 5-7 Heat flux distribution with constant heat flux 3400 $J/s{\cdot}m^2$

5.4 Significance of Thermal Models

Most thermal parameters cannot be measured directly, while temperature can be. As those in the structure analysis case these thermal parameters are material properties and mostly remains unknown at present. The loading and boundary conditions, such as the one at the bottom surface of the plate, are also not confirmed. From the two discussed cases, both constant temperature and heat flux are controllable. Although there is no easy way to validate the thermal model, the analysis still provides information to the plate thermal design and generates useful quantitative result.

Chapter 6. Design Optimization of PEM Fuel Cell Gas Delivery Plate and Its Flow Field

The design objectives of fuel cell plate optimization include: obtaining maximum fuel cell active area; minimizing the potential of by-pass of the delivery gas; achieving ideal pressure drop; delivering maximum amount of oxygen to the MEA surface; and minimizing through stack internal resistance, thus to achieve the best fuel cell performance. Based on these requirements, the design optimization of fuel cell plate is a truly multidisciplinary optimization issue, which needs global consideration. This global interdisciplinary optimization is to be discussed in next chapter. This chapter focuses on the single disciplinary optimization.

6.1 Formulation of the Optimization Problem

The optimization in this study focuses on flow field, plate structure and thermal performance. The general form of optimization problem is formulated as:

$$\begin{aligned} &\min_{X} f(X) \\ &\textit{subject to}:\ g_j(X) \le 0 \qquad j = 1,\ldots,p \\ &\qquad\qquad X = [x_1,\ldots,x_N] \end{aligned} \tag{6-1}$$

In this design optimization, a number of issues need to be addressed. These include the specification of the objective function, $f(X)$, and the constraints, $g_j(X)$ ($j = 1,\ldots,p$); the selection of design variables, X; sensitivity analysis on the optimization problem; and the solution method.

The main design objective is to maximize fuel cell efficiency. Based on the discussion of chapter 3, the performance of the fuel cell is measured indirectly through the oxygen content at the MEA interface of the flow channel, and carried out using the airflow CFD simulation. Many design considerations can be considered as constraints to the optimization based upon the worst-case conditions. These include structure performance such as maximum stress level and displacement, as well as thermal performance such as temperature distribution in the flow channel and the plate. Some other fuel cell performance issues such as electric resistance of the building layer and manufacturability measured by costs and printability are not included.

Key dimensions and physical parameters of the flow field and fuel cell plate are defined as design variables in the optimization. These include building layer wall thickness, layer thickness, channel height, channel width, rib spacing in the channel, mechanical performance, and thermal boundary conditions. Some other important geometries such as rib geometry (height, angle, thickness), and physical parameters like stoichiometric flow ratio, mass density, convection coefficient, etc. are considered as fix parameters instead of design variables. In addition, geometry constraints that ensure the consistency of fuel cell geometry are also included.

The inclusion of the design constraints is subject to their linearity and through variable sensitivity study. Tests using optimization routines on CFD and finite element structure analysis are carried out to understand the sensitivity of each constraint and design variable. These studies are essential to the formulation of the problem and the selection of an efficient optimization algorithm.

The optimization functions, both objective and constraints, are evaluated using finite element and finite volume analyses using engineering codes CFX, Pro/MECHANICA and ANSYS. The built-in optimization functions of Pro/MECHANICA and ANSYS are used for structure and thermal analysis, while the external design optimization code Recursive Quadratic Programming Routine (REQPAL) is embedded into the CFX code in this work to perform the design optimization through CFD simulation.

One significant aspect needs to be emphasized on this virtual prototyping based design optimization is the selection of design objective, constraints and design variables for the single disciplinary optimizations discussed in this chapter. Traditionally mechanical design relies on several acceptable physical prototypes to pursue the new design goal. The design optimization accomplishes the ideal goal using certain performance restriction as constraints and changeable parameters as design variables. This traditional and straightforward method is not suitable for the optimal design on the fuel cell plate because there is not enough information for the designer to use, even mature structure materials.

Virtual prototyping technique using CAD/CAE tools can quantify all parameters, performances and conditions. This advantage allows the virtual prototyping based design optimization to select unknown parameters and conditions as design objective and design variables. The idea is applied on structure design optimization and thermal design optimization to provide information for the material development and cooling effect study.

6.2 Flow Channel Design Considerations for Oxygen Enhancement

Fuel cell flow channel design optimization is carried out to enhance the oxygen concentration at the channel-MEA interface. CFD performance simulation is made using the CFX code and is operated based on mathematical model used, which is same as those in Section 3.4.

As a part of global multidisciplinary design optimization, the ideal method to implement the CFD simulation as a single disciplinary optimization is to use a single program that balances function and performance for all fluid dynamic, solid mechanics, and heat transfer issues. But this type of program is far away from mature.

ANSYS has good structure and thermal analysis function with powerful design optimization tool. But the CFD function in ANSYS, FLOTRAN, can only solve Equations 3-2 to 3-4, with Equation 3-5 as zero source term (refer to Subsection 3.4.2). Therefore the ANSYS code cannot be directly combined with CFD analysis for structure and thermal analysis as well as design optimization.

As many other powerful CFD codes, the commercial CFX code does not include design optimization function. A traditional method is to directly use an external optimization program to link the CFX code. This method normally needs program development to combine both optimization code and CFX code. A few user routines (in CFX called User Fortran) must be used for the connection. The advantage of this direct method is straightforward. But the approach suffers the disadvantage that involves lengthy programming work and multiple program interfaces. Meanwhile, the method does not combine the CFD simulation to structure and thermal analysis. Further work is still needed for their combination.

Before automated design optimization using virtual prototype considered, the detailed simulation model used for the automated design optimization is discussed. A trial and error approach is applied to determine the geometric model for the automated design optimization. This trial and error study provides the information on the model accuracy and geometry parameter selection.

6.2.1 Trial and Error Analysis Using CFX

The geometry model shown as Figure 3-6 was generated using preprocessor, Mesh Builder in CFX code. The Mesh Builder is a graphical programming program to allow building non-uniform grid with appropriate aspect ratio with graphical interface. The generated ASCII file is used as geometry input, which is called by the CFX main program, control file. The advantage of using Mesh Builder is the non-uniform grad generation, which saves computation time and ensures certain accuracy. The drawback is that changing geometric dimension and grid definition can only be made through manually modification to the geometry ASCII file under graphical programming, making the automation of optimization impossible. To overcome this disadvantage, defining the geometry information in the control file or user routine, which can be called by control file, is needed.

The geometry information is defined through >>MODEL TOPOLOGY and >>CREAT GRID functions in the control file. The integer block dimension of the geometry model is set under >>MODEL TOPOLOGY command, while the real dimension value for each grid is assigned with sub command >>SIMPLE GRID under >>CREAT GRID. The inconvenience of this definition method is that only uniform grid can be applied, which using unnecessarily long computation time. The advantage is that the geometry definition can be performed by adjusting one or a small number of variables in the control file.

To allow the geometry dimension to change with certain accuracy, fine grid should be used. In the case of using 1 *mm* level geometry, the maximum grid dimension should not be over 0.1 *mm*. In this case, for a 70 × 0.8 × 1.5 *mm* block geometry with 0.1 × 0.04 × 0.075 *mm* grid, the total number of grid is 280,000. Meanwhile, other parameters and boundary conditions are defined in the same way as those used in Chapter 3.

The CFD model used in the analysis is similar to that in Figure 4-2, with unchanged parameters include initial inlet pressure, $P_{in} = 3$ *atm*, initial inlet temperature, $T_{in} = 90\ ^oC$, initial wall temperature, $T_{wall} = 80\ ^oC$, current density, $i = 1A/cm^2$, stoichiometric flow ratio at channel inlet, $\xi_{O2,in} = 2$, inlet oxygen fraction, $y_{O2,in} = 0.218$, constant specific heat for oxygen, $C_{pA} = 942\ J/kg^oC$, and mass transfer coefficient of oxygen, $\Gamma_A = 2.82e\text{-}6$ *kg/m·s*. The changing parameters are mainly geometric dimensions that include model height H, model width w, first rib position L_1, first rib thickness t_1, second rib position L_2, second rib thickness t_2, and model length L, as shown in Figure 6-1 and in Table 6-1.

When considering the geometry change on the channel width, w, and length, L, the Equation 3-6 with the reaction area, $A_{MEA} = (w \times L)_{MEA}$, leads to the expression:

$$\dot{M} = -\frac{i \times (w \times L)_{MEA}}{4F} \times (32 \times 10^{-3}) \qquad (6\text{-}2)$$

The Equation 6-2 presents the relation between current density, i, and oxygen consumption rate, $\dot{M}$. The simulation discussed in Chapter 3 selects the average values of i and $\dot{M}$ based on this relation. The exact expression for current density, i, is formulated in Equation 3-1, relating to the oxygen concentration:

$$i = i_0 \frac{C_{O_2}}{C_{O_2,ref}} \exp\left(\frac{4kF}{RT}\eta\right) \tag{6-3}$$

This relation shows that the current density, i, is a function of oxygen concentration on the MEA reaction surface. Both Equations 6-2 and 6-3 can be used for the expression of either local or global phenomena. The local oxygen consumption rate $\dot{M}$ is a function of local oxygen concentration. The exact global reaction is determined by the current density distribution expressed as Equation 6-3.

This study concentrates on the oxygen concentration related to the oxygen consumption. For simplicity, the oxygen consumption rate, $\dot{M}$, is only determined using Equation 6-2 based on the average value for current density, for calculating the oxygen concentration distribution, although $\dot{M}$ itself is still a function of oxygen concentration.

The simulation calculated in Chapter 3 monitored the oxygen concentration under the first rib, while the analysis in this chapter considers the average oxygen concentration along the bottom surface, as shown in Figure 6-1, which is the MEA reaction area. The results are shown in Table 6-1.

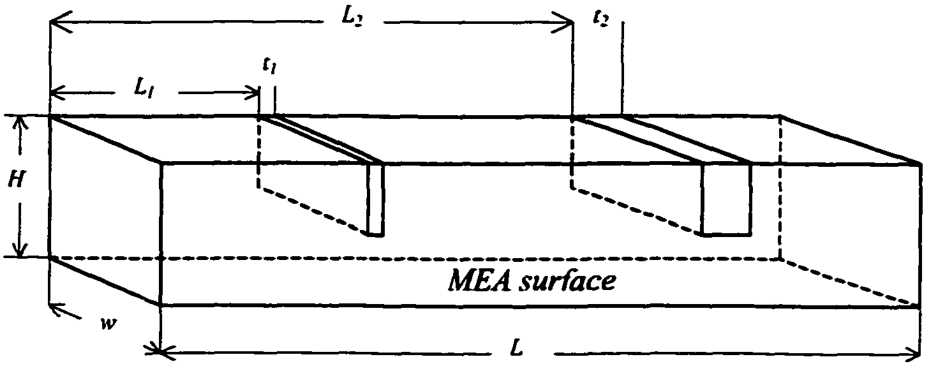

Figure 6-1 CFD geometry model used for design optimization

Model geometry heavily influences the oxygen level at the MEA interface, as shown by Models 1-m03 and 1-m06. However, the model assumed a constant oxygen consumption rate at the MEA surface, causing negative oxygen concentration after a certain length of dimension, which is untrue as shown by the computation result of Model 2-m17 with a small negative value at the right bottom corner, as shown in Figure 6-2. To avoid this inaccuracy, the simulation in this Chapter is limited to a length of 70 *mm* as used in Table 6-1.

Table 6-1 Trial and error analysis on flow channel simulation

Model	$H(mm)$	$w(mm)$	$L_1(mm)$	$t_1(mm)$	$L_2(mm)$	$t_2(mm)$	$L(mm)$	O_2 (%)
1-m02	0.8	1.5	25	1	0	0	70	6.341
1-m03	0.8	1.5	0	0	0	0	70	6.112
1-m04	0.8	1.5	24	1	0	0	70	6.340
1-m05	0.8	1.5	24	5	0	0	70	6.619
1-m06	0.8	1.5	0	0	0	0	50	8.560
1-m07	0.8	1.5	29	5	0	0	70	6.624
1-m08	0.8	1.5	24	2	54	2	70	6.690
1-m09	0.8	1.5	24	2	61	2	70	6.646
1-m10	0.8	1.5	24	5	61	5	70	6.999
1-m11	0.8	1.5	24	2	61	5	70	6.749
1-m12	0.8	1.5	24	3	61	5	70	6.864
1-m13	0.8	1.5	24	4	61	5	70	6.932
1-m14	0.8	1.5	25	3	61	5	70	6.865
1-m15	0.8	1.5	26	2	61	5	70	6.796
1-m16	0.8	1.5	27	1	61	5	70	6.723
1-m17	0.8	1.5	25	1	61	5	70	6.722
1-m18	0.8	1.5	25	2	61	5	70	6.795
1-m19	0.8	1.5	25	4	61	5	70	6.934
2-m02	0.8	1.5	26	1	61	5	70	6.722
2-m03	0.8	1.5	26	3	61	5	70	6.866

2-m04	0.8	1.5	26	4	61	5	70	6.934
2-m05	0.8	1.5	27	2	61	5	70	6.796
2-m06	0.8	1.5	27	3	61	5	70	6.867
2-m07	0.8	1.5	27	4	61	5	70	6.935
2-m08	0.8	1.5	27	5	61	5	70	7.002
2-m09	0.8	1.5	28	1	61	5	70	6.724
2-m10	0.8	1.5	28	2	61	5	70	6.797
2-m11	0.8	1.5	28	3	61	5	70	6.867
2-m12	0.8	1.5	28	4	61	5	70	6.936
2-m13	0.8	1.5	28	5	61	5	70	7.002
2-m14	0.8	1.5	29	1	61	5	70	6.724
2-m15	0.8	1.5	29	2	61	5	70	6.797
2-m16	0.8	1.5	29	3	61	5	70	6.868
2-m17	0.8	1.5	29	4	61	5	70	6.936
3-m19	1	2	29	4	61	5	70	7.130
3-m20	2	2	29	4	61	5	70	6.290
3-m22	2	1.5	29	4	61	5	70	6.491
3-m23	2	2.5	29	4	61	5	70	6.187
3-m24	1	2.5	29	4	61	5	70	7.089
3-m25	1	1.5	29	4	61	5	70	7.205
3-m26	1.5	1.5	29	4	61	5	70	6.888
3-m27	1.5	2	29	4	61	5	70	6.768
3-m28	1.5	2.5	29	4	61	5	70	6.691

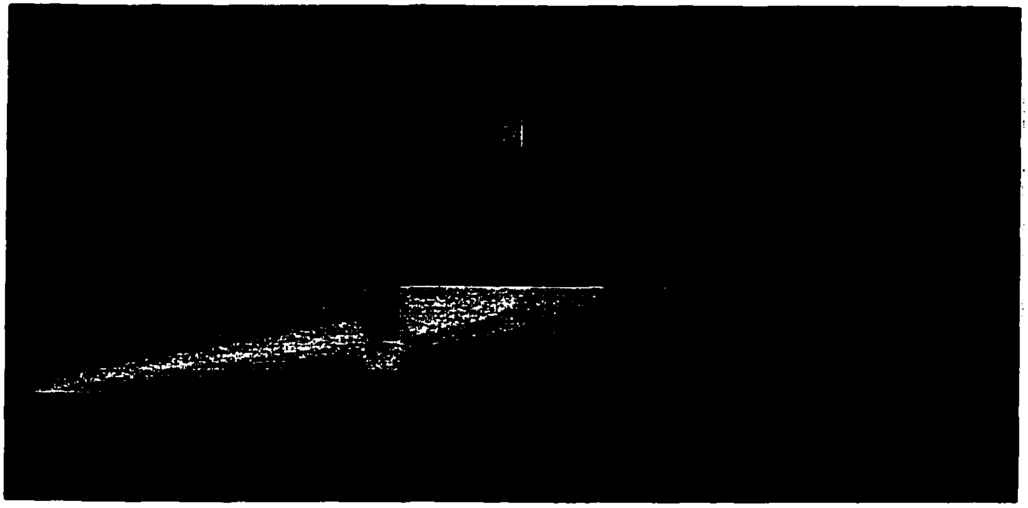

Figure 6-2 Negative oxygen concentration at right bottom corner

Models 1-m09 to 2-m17 in Table 6-1 change only the first rib position L_l and first rib thickness t_l, with all other geometry parameters as constant. The results show that the oxygen concentration is more sensitive to rib thickness than to rib position. Models of 3-m19 to 3-m28 show the relation between oxygen concentration and channel width, w, and height, H. The results are shown in Figure 6-3.

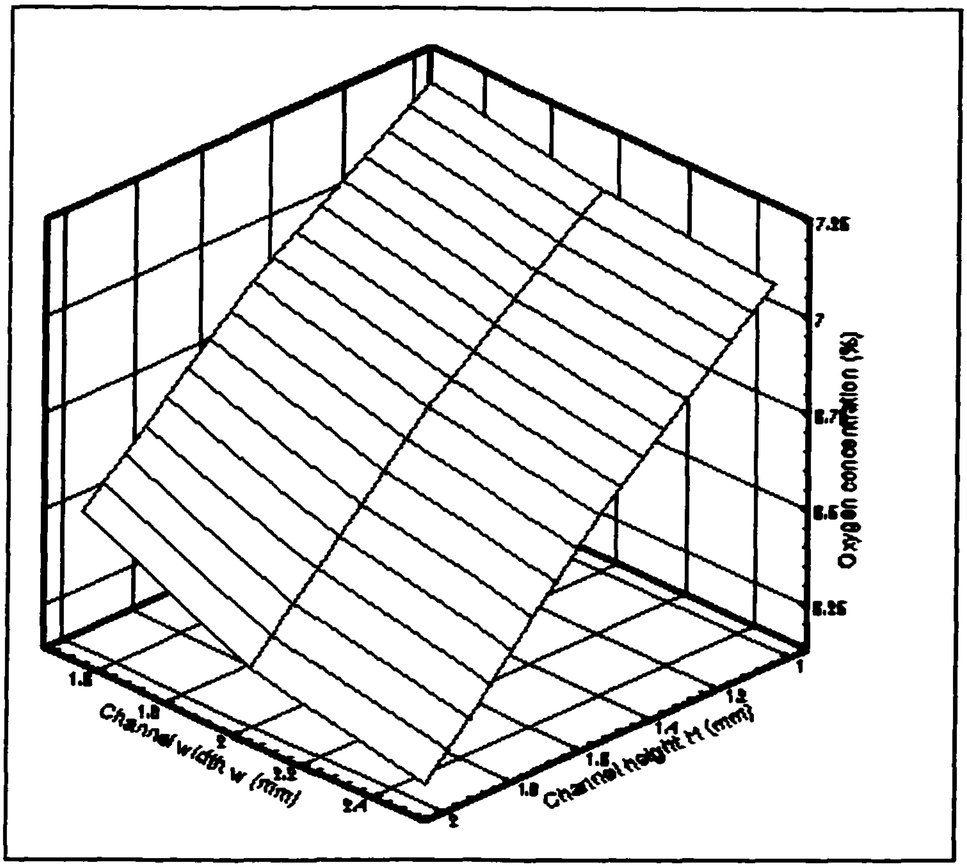

Figure 6-3 Trial and error result: oxygen concentration vs. channel width and height

The trial and error based sensitivity analysis indicates that the decrease of channel height, *H*, and/or the increase of first rib thickness, t_l, play a more impact role than the decrease of channel width, *w*, and/or the increase of first rib position, L_l, in improving oxygen concentration. The trial and error analysis demonstrated that oxygen concentration is not a simple function of any geometry parameters. Identification of the design optimum is going to be quite time consuming if the trial and error method is used. This leads to the design optimization approach to be presented in the following section.

6.2.2 CFD Design Optimization Using CFX

Most CFD study involves mathematical models based on complex differential equations, and simulations for model verification. CFX code is one of the most powerful CFD tools. However the code has no embedded function to perform design optimization, as other powerful commercial CFD codes available today. To overcome this limitation, an optimization routine is added to the commercial CFD code CFX, to carry out the virtual prototyping based design optimization.

The CFX code was built using Fortran programming language. At present, the code can be applied with graphic interface to carry out preprocessing, modeling, solution, and post-processing. As an appropriate product, the source code of program is not provided to a user. However, the code can be run externally, under UNIX and DOS environments.

A mature design optimization code, Recursive Quadratic Programming Routine (REQPAL), is used as the optimization tool for CFX code. REQPAL is an Equality Constrained, Recursive Quadratic Programming program based on the augmented Lagrangian penalty function. The algorithm and program were originally developed by Chen, Kong and Cha [Chen 1989], and later extended by S. Liu [Dong 1994]. REQPAL can serve as a general optimization tool, even though it is particularly suitable to quadratic objective functions. The program has different subroutines to perform initialization, step searching, constraint identification, matrix calculation, convergence calculation, and etc. in both FORTRAN and C.

When merging the REQPAL code to CFX code, several REQPAL subroutines and CFX User Fortran routines must be modified to support data transfer between the two packages. The design objectives, constraints and variables of the optimization determine the data transfer and their control procedure. The procedure for performing design optimization is shown by the flow chart shown in Figure 6-4.

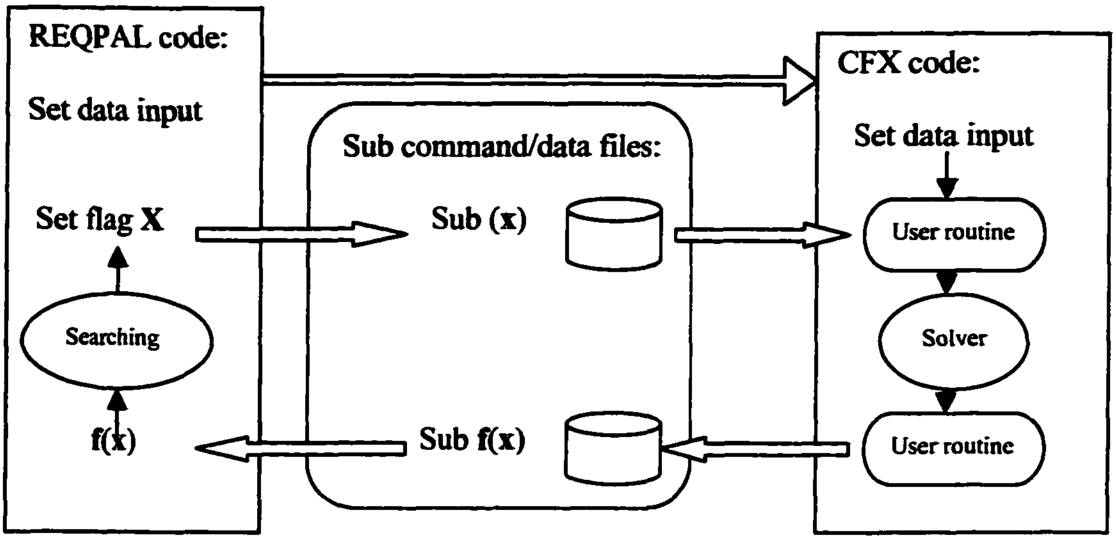

Figure 6-4 Design optimization flow chart using REQPAL and CFX

The CFX code functions as a function subroutine called and initiated by the "main" program through the DOS shell script command in the REQPAL code. All inputs are defined through the initialization subroutine, Start, and the CFX control file. A set of design variables, geometry dimensions, is defined with a modified format and saved in a data file, called Sub (x) before running the CFX program. The data in Sub (x) is read by a user routine USRTPL, that is used for >>MODEL TOPOLOGY definition in the CFX code. The >>MODEL TOPOLOGY definition in CFX code can only accept integer value as block dimension, thus the real value of design variables in the REQPAL are rounded to integer values corresponding to grid definition. Therefore, the Sub (x) is an integer value data file to be read by USRTPL, while the real values of geometry dimension are defined under >>CREAT GRID in CFX code for each grid dimension.

The simulation carried out by the CFX solver is used to evaluate the design objective – the average oxygen concentration along the MEA reaction area. The results from the evaluation is saved to the output file called Sub f(x), using the user routine USRTRN in CFX code. The REQPAL program then reads in the objective function value f(x) from

Sub f(x), and makes the next move in the design optimization. For the newly generated search point, REQPAL will go through the same objective function evaluation using CFX until the convergence criteria are satisfied.

The CFD model used in design optimization is identical to those shown in Figure 6-1, where, the fixed dimensions are: model length $L = 70$ *mm*; model width $w = 1.5$ *mm*; model height $H = 0.8$ *mm*. Other parameters include initial inlet pressure, $P_{in} = 3$ *atm*, initial inlet temperature, $T_{in} = 90$ *°C*, initial wall temperature, $T_{wall} = 80$ *°C*, current density, $i = 1A/cm^2$, stoichiometric flow ratio at channel inlet, $\xi_{O2,in} = 2$, inlet oxygen fraction, $y_{O2,in} = 0.218$, constant specific heat constant for oxygen, $C_{pA} = 942$ *J/kg°C*, and mass transfer coefficient of oxygen, $\Gamma_A = 2.82e\text{-}6$ *kg/m·s*.

Two key channel feature geometry parameters are selected as design variables, the first rib position, L_1, and the thickness of this rib t_2. The optimization is aimed at maximizing the average oxygen concentration along the MEA channel interface:

$$\max_{L_1, t_1} \left[\frac{1}{n}\sum_{i=1}^{n} Y_{O_2}^{MEA}\right] \tag{6-4}$$

$$L_{1,\min} \le L_1 \le L_{1,\max}$$
$$t_{1,\min} \le t_1 \le t_{1,\max}$$

where, $Y_{O_2}^{MEA}$ is average oxygen concentration along the MEA surface as shown in Figure 6-1. The design variables are:

(a) first rib position; $10.0\ mm < L_1 < 35.0\ mm$;

(b) first rib thickness; $0.5\ mm < t_1 < 15.0\ mm$.

The second rib position $L_2 = 61$ *mm* and thickness $t_2 = 5$ *mm* treated as constant, to simplify the problem.

CFX code is defined with 220 iterations to get converged function evaluation. For the 0.1 × 0.04 × 0.075 *mm* grid and the 70 × 0.8 × 1.5 *mm* channel geometry the objective function evaluation requires about 90 ~ 110 *min* on Pentium III 650*Hz* workstation. The initial search point is at $L_l = 2.9$ *mm*, $t_l = 4.0$ *mm*.

While the CFX code needs to read integer data from the REQPAL code, the real value of design variables in REQPAL must be modified before transferred to CFX, as shown in Figure 6-4. The change of L_l and t_l are along the model length direction, L, with a grid size of 0.1 *mm*, which is the minimum length change for the two design variables. To accomplish certain accuracy, the two design variables in REQPAL, X(1) and X(2), corresponding to L_l and t_l respectively, should be set as small as possible. In this case, the unit of 10^2 *mm* is selected as design variable unit in REQPAL, while the integer value of design variables transferred to CFX is assigned through the rounding off as:

$$\begin{aligned} \text{IST} &= \text{INT}\,(\text{X}(1)*1000+0.5\,) \\ \text{IFN} &= \text{INT}\,((\text{X}(1)+\text{X}(2))*1000+0.5\,) \end{aligned} \tag{6-5}$$

where, the IST and IFN are integer values of design variables in CFX, corresponding to L_l and t_l, respectively. The accuracy for calculating the gradient is defined as $sfd = 10^{-3}$, and accuracy for convergence evaluation, $acc = 10^{-8}$.

The design optimization converged after 11 iterations with 111 function evaluations, 111 constraint evaluations and 11 gradient evaluations. The design variables optimum is located at: first rib position, $L_l = 25.15$ *mm*, first rib thickness, $t_l = 15.00$ *mm*; and the objective function: oxygen concentration, $f = 7.626\%$. The relation between the design objective and design variables is shown in Figures 6-5 to 6-7.

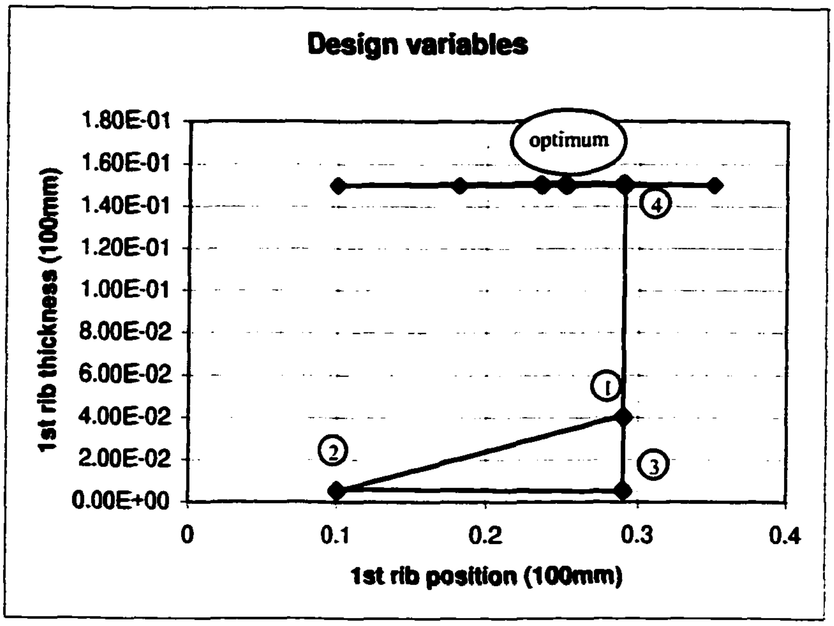

Figure 6-5 Design variable profile for CFD design optimization

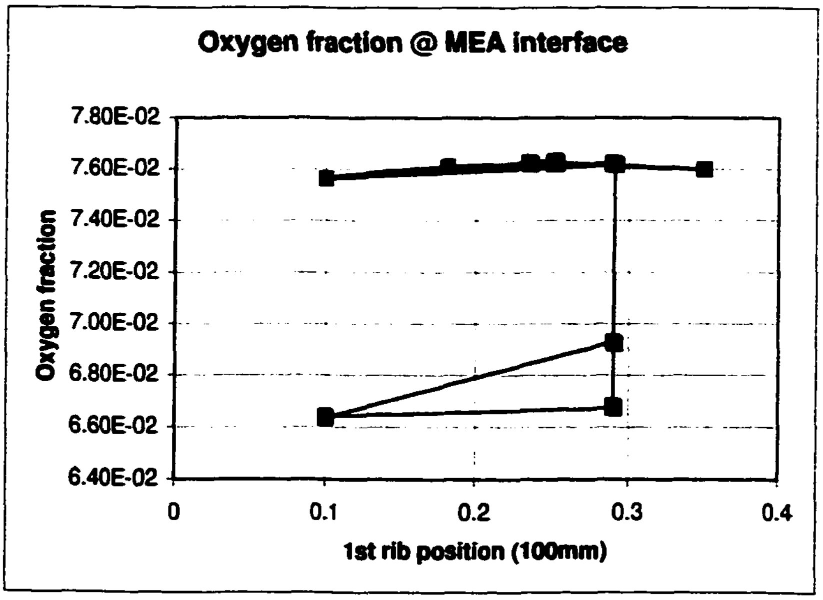

Figure 6-6 Oxygen fraction vs. 1st rib positioning

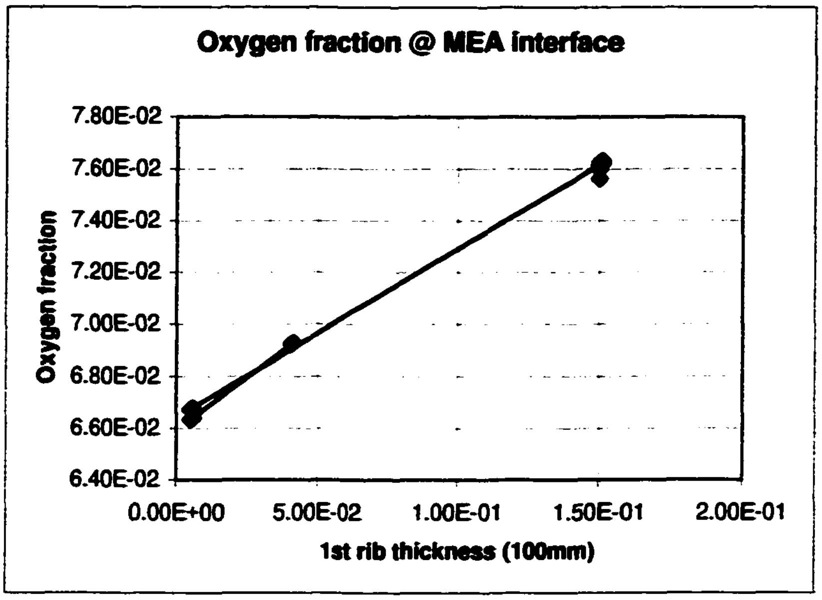

Figure 6-7 Oxygen fraction vs. 1st rib thickness

From the Figure 6-5, the design variables quickly move to the maximum value of first rib thickness, t_I, leading to the high oxygen concentration along the MEA surface. The influence of t_I has more impact than first rib position, L_I. The results are exactly same as those from trial and error analysis discussed in Subsection 6.2.1.

The improvement on average oxygen level, introduced by the design optimization, is illustrated in Table 6-2. The results show that the maximum average oxygen fraction along MEA surface in the model is about 7.62%. This value is 10.12% higher compared to the original design. If compared to the minimum average oxygen fraction value of 6.63%, the optimal design is 14.93% better. This simulation result agrees with the experiment data acquired from fuel cell tests, in both of the benchmark flow-field configuration and in the trends of variations.

Table 6-2 Average oxygen concentration comparisons

	Initial point	Point1 (random)	Point2 (random)	Minimum	Maximum
Average O_2 concentration	6.92%	6.72%	7.00%	6.63%	7.62%
Rel. change	0%	-2.89%	+1.16%	-4.19%	+10.12%

In summery of flow channel design for oxygen concentration, the design optimization provides fast way to get the optimal result, even though the whole calculation needs about 8 days to accomplish due to the large number of grids used.

6.3 Design Consideration Based on Structure Integrity

6.3.1 The Approach of Design Optimization

Design optimization of the oxidant air delivery plate is carried out with key geometric parameters of the plate, some of them were used as design variables in the previous section. These parameters specify the geometry of the printed flow channels of composite material formed by the screen printing layer deposition technique. Material is another variable in the plate optimization. Some of the design variables determine the flow field of the plate and influence the oxidant airflow to be modeled and simulated using the CFD codes. Others determine the strength of the flow channel to be modeled and simulated through FEA analysis. These key variables are included in the design variable of the optimization, *X*:

$$X = \left[w, H, D, D_1, D_2, D_M\right]$$

where, w is the width of the flow channel, from which the width of channel wall thickness, W, can be calculated; H is the height of the flow channel and the deposited layer; D is the length or width of the square plate and is related to the length of the flow channel; D_1 and D_2 are the two channel feature parameters, first rib position, L_1, and first rib thickness, t_1; and D_M represents the material selection for the deposited layer.

The width of the flow channel, w, indirectly determines the width of the flow channel, W. When the side wall of the plate is selected to be 1.2 time of channel wall, the two parameters, channel width, w, used in CFD and, channel wall width, W, used in FEA become related:

$$18.4W + 17w = D. \tag{6-6}$$

These key design variables are used in an iterative design process involving two design optimizations. Each design optimization is carried out using a subset of all of the design variables. Due to the potential conflicts between the two separated design optimizations, the following iterative process is proposed:

Step 1: Maximizing the oxygen concentration level in the flow channel using CFD simulation to get the average oxygen concentration.

Given w_0 and H_0 in the design vector, X, to carry out the optimization with respect to channel feature parameters D_1 and D_2. Other design variables are considered constant in this modeling. The optimization leads to

$$X_1^* = \left[w^{0,1}, H^{0,1}, D^{0,1}, D_1^{1,*}, D_2^{1,*}, D_M^0 \right]$$

Step 2: Minimizing the maximum stress within the printed channel using FEA analysis to consider structure loads and thermal stress.

Verifying whether the calculated maximum stress and strain using FEA analysis are within the values allowable by the material.

To carry out the optimization with respect to channel/layer height, H, channel wall width, W, and plate width, D. The optimization provides ideal materials properties for material design, including Young's modulus or stiffness, yield stress, ultimate strength, etc. For simplicity, all of the material parameters are represented using a single materials parameter, D_M. *The result of the optimization is recorded as:*

$$X_2^* = \left[w^{2,*}, H^{2,*}, D^{0,1}, D_1^{1,*}, D_2^{1,*}, D_M^{2,*} \right]$$

Step 3: If $|X_2^* - X_1^*| \leq \delta$, δ *is a predefined small value. The approach converged, go to Step 4. Otherwise, chose a different* D_M, *set* $X_0 = X_2^*$ *, and go back to Step 1.*

Step 4: Find appropriate composite material following the suggested material property, D_M.

The CFD design optimization conducted previously led to improved fuel cell performance with channel width ($w^* = 1.5\ mm$) and height ($H^* = 0.8\ mm$). These correspond to the wall width, W, and layer thickness, H, in Figure 4-1, respectively. These values are then used as geometry constraints to the structure design optimization:

$$\begin{gathered} W_0 - \varepsilon_1 \leq W \leq W_0 - \varepsilon_1 \\ 2H_0 - \varepsilon_2 \leq H \leq 2H_0 - \varepsilon_2 \end{gathered} \qquad (6\text{-}7)$$

where, ε_1 and ε_2 are small deviation for defining the ranges of the variable.

The design optimization defined in *Step 2* is to be carried out in following sections.

6.3.2 Formulation of the Design Optimization

In this work, design optimization is carried out for both plate geometry and material. Two different design objectives and two different sets of design variables are used in tandem.

The most challenging issues facing the fuel cell plate material development are good conductivity, excellent electro-chemistry stability, sound structure integrity and low cost. Three key material properties: maximum stress, maximum strain, and stiffness, are directly related to the structure design requirement. For composite material development, minimum yield stress, minimum failure strain, and minimum young's modulus will support a broader selection of composite material composition.

The maximum von Mises stress relates to the lifetime of the structure. By selecting the minimum maximum von Mises stress, σ_{vm}, as the objective function, the optimal design will provide lowest material strength requirement, which the newly developed composite material needs to satisfy. Another material performance, maximum 1st principal strain, ε^{I}, is defined as a constraint for the optimization to satisfy material deformation restriction. The selections of design variables are based upon two different considerations, plate geometry and plate materials, as discussed in the following.

(a) Geometry Design

In the plate geometry design optimization, traditional geometry parameters are used as design variables. The material parameters are assumed to be constants with their values determined from similar materials. The optimization considers the worst-case condition, minimizes the maximum von Mises stress, σ_{vm}, of the structure, subject to the constraint of the maximum strain level, $[\varepsilon]$, for the maximum allowed 1st principal strain ε^{I}. These stress and strain are evaluated using the ANSYS® finite element analysis model.

The optimization is carried out using two key variables for the plate geometry: the channel wall thickness, W, and the height of the printed layer, H, as shown in Figure 4-1. The optimization is defined as:

$$\begin{aligned} &\min_{W.H} \sigma_{vm} \\ &\textit{subject to:} \quad \varepsilon^{I} \le [\varepsilon] \end{aligned} \tag{6-8}$$

where, the design variables, $X = [W, H]^T$.

(b) Material Design

In the plate material design optimization, both geometry parameters and the material performance parameter of the plate are treated as design variables. By adding the material stiffness as design variable, the optimization will find the ideal value of the stiffness (or the Young's Modulus) of the composite material. The optimization shares the same objective and constraint functions as the plate geometry optimization. The optimization is carried out using three key variables for the plate geometry and material: the channel wall thickness, *W*, and the height of the printed layer, *H*, and the material stiffness (or Young's Modulus), *E*. The optimization is defined as:

$$\min_{W,H,E} \sigma_{vm} \qquad (6\text{-}9)$$

$$\textit{subject to:} \quad \varepsilon^{I} \leq [\varepsilon]$$

where, the design variables, $X=[W, H, E]^T$.

6.3.3 Optimal Design on Linear and Nonlinear Structure Analysis

The structure optimization on the plate includes both geometry and material considerations. One of the built-in optimization functions of ANSYS, advanced zero order method or sub-problem method, was used in the plate structure optimization. The routine applies a search approach, in which a few sets of objective and constraint functions are approximated by several fitted surfaces. The optimization routine searches through the fitted surface, instead of the original function surfaces, to improve search efficiency. The fitting controls use quadratic functions for the objective and constraint functions.

Design optimization is applied to both linear and nonlinear material analysis, based on the model test sets (6) and (8) of Table 4-2, discussed previously. Based on the geometric design consideration of linear analysis test set (6), the geometry parameters wall thickness, *W*, and layer thickness, *H*, in the structure model (Figure 4-1) are chosen as design variables of the Design Set (1), in which *W* varies from 0.5 *mm* to 1.8 *mm*; and *H* varies from 1 *mm* to 2 *mm*. The chosen starting point is at $W = 0.001651$ *m*, and $H = 0.001778$ *m*. The 1st principal strain is used as the design constraint with an upper limit of 12000 $\mu\varepsilon$. The objective function, von Mises stress, is minimized.

In this optimization, all other parameters, i.e. Young's modulus $E = 3$ *GPa*, are fixed as the previous linear analysis simulation set (6) of Table 4-2. The search often ends prematurely at local optima. Many restarts are tested at different start points, including the identified true global minimum at $W = 0.00153$ *m* and $H = 0.00158$ *m*. The minimum stress of Design Set (1) is 45.7*MPa*, which is still very high for the epoxy based composite material, working around 80°C (refer to Table 6-3). No acceptable geometry design for the fuel cell plate can be achieved for this selected materials. Modification on the material is thus considered.

The material Design Set (2) applies both geometry parameters and material's Young's modulus *E* as design variables. The *E* is allowed to vary from 1 *GPa* to 10 *GPa*, while *W* and *H* can change over the same range as in Design Set (1). For the ease of comparison, the optimization starts from the design optimum of the Design Set (1). The optimization converged to a minimum stress of 16.13 *MPa* with the geometry parameters $W = 0.00179$ *m*, $H = 0.00199$ *m*, and material parameter $E = 1.02$ *GPa*, respectively. This result has acceptable stress/strain levels and geometry parameters. The lower Young's modulus of 1.02 *GPa* still provides a reasonable strain value 11885 $\mu\varepsilon$. Both minimum stress and Young's modulus value are used to identify (or develop) the new composite material.

Table 6-3 Design optimization of linear and nonlinear analysis

Design Test & Variables	**Starting Point (*m*)**	**Optimum (*m*)**	**Minimal Stress (*MPa*)**
(1) Linear geometry design W, H	($W = 0.001651$, $H = 0.001778$) ($W = 0.00153$, $H = 0.00158$) etc	$W = 0.00153$ $H = 0.00158$	45.7
(2) Linear material design W, H, E	($W = 0.00153$, $H = 0.00158$, E=3 *GPa*)	W=0.00179 H=0.00199 E=1.02 *GPa*	16.13
(3) Nonlinear geometry design W, H	($W = 0.00153$ *m*, $H = 0.00158$ *m*)	W=0.000525 *m* H=0.00101 *m*	16.17

When applying design optimization through nonlinear finite element analysis, the material doesn't have to be changed, since the stress on the model test set (8) of Table 4-2 is only 17.74 *MPa*. Nonlinear geometry Design Set (3) uses the same geometry parameters of the Design Set (1) as design variables and same range. The starting point of the search uses the same optimum of Design Set (1) ($W = 0.00153$ *m*, and $H = 0.00158$ *m*) for the ease of comparison.

The optimization converged after 21 iterations with the optimal design found at: wall thickness, 0.525 *mm*, and layer thickness, 1.01 *mm*, which are at almost the lower bounds of the two design variables and the design constraint – 1st principal strain of 7615 $\mu\varepsilon$. The minimized objective function, von Mises stress, has been lowered to 16.17 *MPa*. All values at this design optimum are ideal for the fuel cell plate structure.

Figure 6-8 shows a plot of the Maximum von Mises stress vs. Layer Thickness in the optimization search. Alternative structure design can be selected based on this plot. The optimal design, at 16.17 *MPa*, has 8.85% improvement compared to the original structure analysis of 17.74 *MPa*. Detailed comparison of the optimization results are listed in Table 6-4. The ratio between H and W is approximately 2, which is acceptable for the printing process.

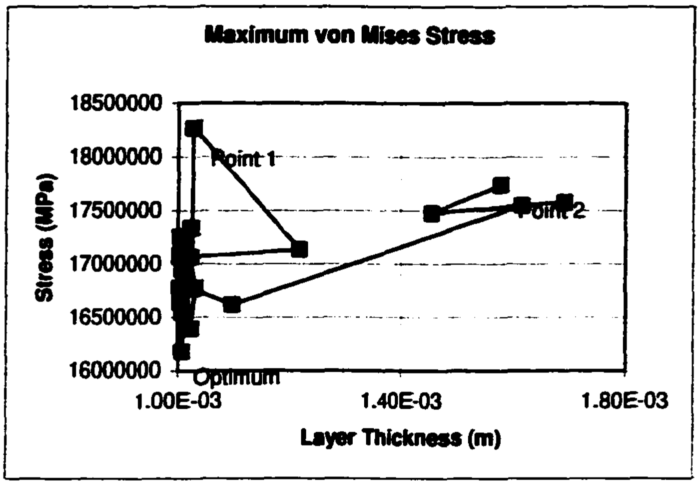

Figure 6-8. Maximum von Mises stress vs. Layer Thickness

Table 6-4 Alternative structure design comparison (nonlinear)

	Starting point	**Point1 (MaxStress)**	**Point2 (Converged)**	**Design optimum**
W (*m*)	0.00153	0.00138	0.000507	0.000525
H (*m*)	0.00158	0.00103	0.001003	0.001007
1st Principal strain ($\mu\varepsilon$)	9127	9582	7696	7615
Von Mises stress (*MPa*)	17.74	18.27	17.09	16.17
Improvements on stress	-	+ 2.99%	- 3.66%	- 8.85%

In summery, the optimal structure design of the fuel cell plates, which includes both geometry design and material design, provides abundant information on the selection of plate geometry and corresponding material. Design test set (2) shows that the minimum stress level can be achieved with larger geometric dimensions and lower Young's modulus material, given the linear material consideration. Design test set (3) indicates that acceptable stress values can also be obtained with smaller geometry dimensions under the assumption that the composite material possesses a nonlinear material property. The material does not have to be altered and an unchanged Young's modulus can be used.

The optimal structure design of the printed plate identifies the minimum maximum stress that can be used for the composite material, ensures that the maximum stress and strain are within the allowed range, and specifies the optimal plate geometry and material. These optimizations provide a broader scope to the feasible composite material, by identifying the lowest acceptable strength of the plate, in the channel material development. The optimizations also specify the corresponding stiffness relating to the Young's modulus of the composite material to be developed.

The proposed iterative plate design method of *Step 1 ~ Step 4* involves two different optimization problems of different nature. The first optimization problem seeks the best fuel cell performance determined by the oxygen concentration, while the second tries to obtain guidelines for composite material development. The potential conflicts between these two optimizations are addressed through an iterative process to identify the best compromise. However, this iterative process may not converge, especially when considering more optimization problems, e.g. thermal performance. A global optimization scheme that integrates the two or more sub-optimizations may provide the solution, which is to be discussed in Chapter 7.

6.4 Design Considerations Based on Thermal Analysis

The design optimization on thermal analysis deals with the temperature distribution and the corresponding parameters. The design parameters include geometry parameters and physical parameters similar as those in flow field and structure analysis. The key geometry parameters of the solid model include: thickness of the printed layer, H, channel wall thickness W, and channel length D, as shown in Figure 4-1. The physical parameters are specific heat, mass density, thermal conductivity and thermal convection coefficient.

6.4.1 Formulation of the Design Optimization

The purpose of thermal design on fuel cell plate is to monitor the temperature distribution to avoid the over heat especially on the MEA surface. Normally, a higher MEA temperature can deliver a higher power density, but will also cause quicker aging of the polymer membrane. The currently used PEM fuel cell is normally operated around 80 ^oC. Thus the objective function is selected to minimize the difference between maximum cell temperature and 80 ^oC. The design variables are selected based on two different cases: geometry parameter only or heat flux cooling effect only. The optimization is formulated as:

$$\min_{X} \; |MaxTemp - 80^oC|$$

where, the design variable $X = [W, H]$ with geometry consideration; or $X = [HeatCoo]$ with cooling effect consideration. The optimization has no constraints.

6.4.2 Solution of Optimal Thermal Design

The thermal design optimization of the plate include both geometry and heat flux cooling effect considerations. One of the built-in optimization functions of ANSYS, advanced zero order method or sub-problem method, is used for the plate thermal design optimization. Based on the geometry consideration, the geometry parameters wall thickness, W, and layer thickness, H, in the thermal model (Figure 4-1) are chosen as design variables. W may vary from 0.5 mm to 1.8 mm, and H may vary from 1 mm to 2 mm. The objective function, $|MaxTemp\text{-}80^oC|$, is minimized. The starting point is $W = 0.00153\ m$, and $H = 0.00158\ m$, with a fixed side length, $D = 0.055626\ m$.

The boundary conditions include: a temperature on the bottom surface is at 80 ^oC and a heat flux $q = 1200\ J/s{\cdot}m^2$ at the top surface, corresponding to the low current density and high voltage operating point shown in Figure 5-1 and 5-2; fluid convection in the channel with the bulk temperature $T_{bulk} = 90\ ^oC$; and all periphery side boundaries are insulated. Other coefficients are specific heat $c = 1047.6\ J/kg\cdot{}^oC$; density $\rho = 1299.52\ kg/m^3$; convective coefficient $h = 80\ J/s{\cdot}m^2{\cdot}{}^oC$; thermal conductivity $k = 0.187599\ J/s{\cdot}m{\cdot}{}^oC$. The load is performed with one load step with 10 substeps.

The optimization converged after 9 iterations with the maximum temperature dropped from 366.9 ^oK (93.9 ^oC) to 361.8 ^oK (88.8 ^oC). The relation between maximum temperature and design variables is shown as Figures 6-9 and 6-10. This results shows that the influence of the channel geometry to the maximum temperature is limited, which is ideal to the thermal design of the plate. On the other hand, the converged temperature of 88.8 ^oC on the MEA surface is still 8.8 ^oC higher than the ideal 80 ^oC. This indicates that the fix temperature boundary condition of 80 ^oC at the channel bottom is not appropriate, and in reality, impossible. Therefore, a negative heat flux on the channel bottom to simulate the cooling effect should be included.

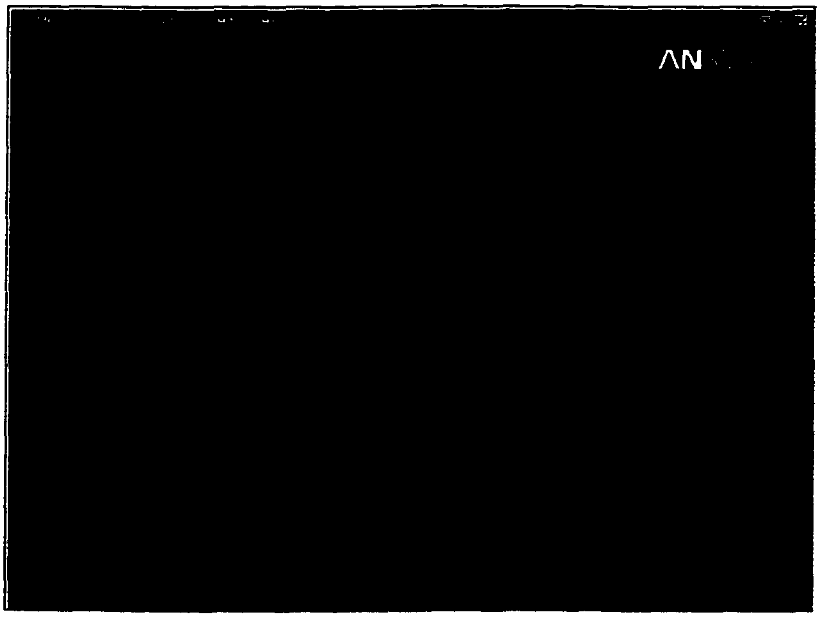

Figure 6-9 Maximum temperature vs. wall width

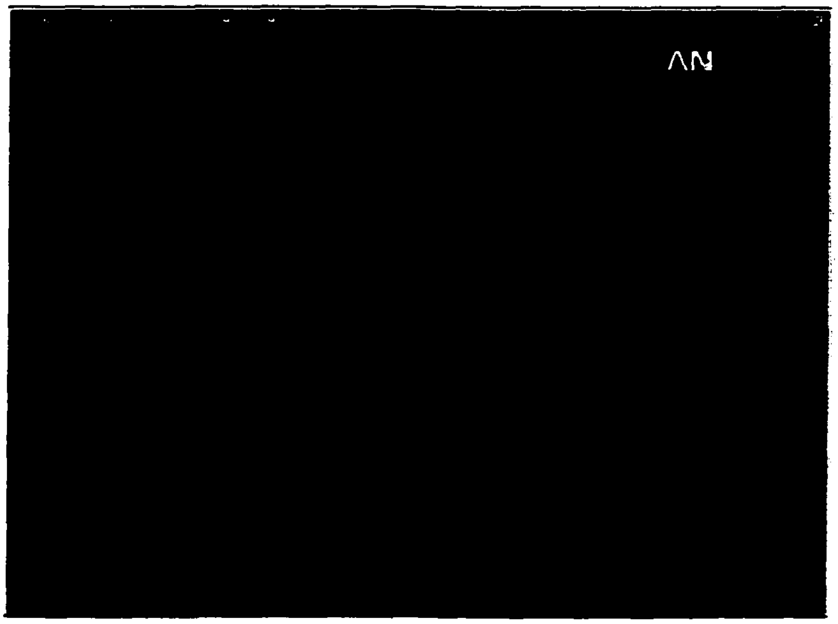

Figure 6-10 Maximum temperature vs. layer thickness

The cooling effect consideration applies a new boundary condition to the bottom of the channel to replace the 80 ^oC with a negative heat flux as design variable. The model is the same as the one introduced in Chapter 5.3 with the results shown in Figures 5-6 and 5-7. The heat flux representing the heat generated from the MEA reaction area is a constant, $q = 1200$ $J/s{\cdot}m^2$, applied to the top of the channel as shown in the geometric model in Figure 4-1. A constant heat flux of negative value at 3400 J/sm^2 simulates the cooling effect. Other geometry parameter includes the fixed $D = 0.055626$ m. The initial value of the design variables are $W = 0.00153$ m and $H = 0.00158$ m, with a range of 0.0005 m to 0.0018 m, and 0.001 m to 0.002 m, respectively. The stopping tolerance is 10^{-6}. The optimization is converged after 8 iterations with a maximum temperature at 352.75 ^oK (79.75 ^oC), which is ideal for safe PEM fuel cell operation.

Using the constant top heat flux $q = 1200$ $J/s{\cdot}m^2$, a fixed $D = 0.055626$ m, same starting point of $W = 0.00153$ m and $H = 0.00158$ m, with same variable range and tolerance, a number of different negative heat flux values for cooling are selected: 1,000 $J/s{\cdot}m^2$, 2,000 $J/s{\cdot}m^2$, 3,000 $J/s{\cdot}m^2$, ..., 20,000 $J/s{\cdot}m^2$. The max temperature at starting point, optimal geometry, and optimal max temperature are shown in Table 6-5. The max temperature, optimal max temperature, and objective function vs. cooling flux relations are shown as in Figures 6-11 (a) ~ (c). For comparison, the optimization results using both geometry design variables W, H and cooling as the third design variable (which starts from 3400 $J/s\cdot m^2$, with a range from 100 to 10,000, and a tolerance value of 1) is also shown in Table 6-5.

Table 6-5 Thermal optimization of different cooling for heat flux source at 1200 $J/s\times m^2$

Therm. Opt. Model (Neg. Heat Flux, J/sm^2)	Max Temp. (^oK) @ starting points	Optimal geometry (*mm*)	Opt. Max Temp. (^oK)
1000	373.70	W=0.50267, H=1.0032	368.23
2000	364.55	W=1.7971, H=1.0023	360.84
3000	361.69	W=1.7971, H=1.0023	354.72
3400	360.54	W=1.7836, H=1.0232	352.75
4000	358.82	W=1.4952, H=1.1208	353.33
5000	355.96	W=1.5710, H=1.3903	353.05
6000	352.08	Starting point	No change from starting
7000	350.23	W=1.3078, H=1.6217	353.39
8000	347.36	W=1.2352, H=1.6883	353.08
9000	344.50	W=0.99057, H=1.5911	353.09
10000	341.63	W=1.0044, H=1.6924	352.86
11000	338.77	W=1.1887, H=1.9895	353.15
12000	335.90	W=0.96277, H=1.7928	352.39
15000	327.31	W=0.84458, H=1.8605	352.46
20000	312.98	W=0.68682, H=1.9129	353.05
D.V. using W, H, and *Cooling* together	360.54	W=1.4001, H=1.5376, *Cooling*=6217 $J/s\times m^2$	353.07

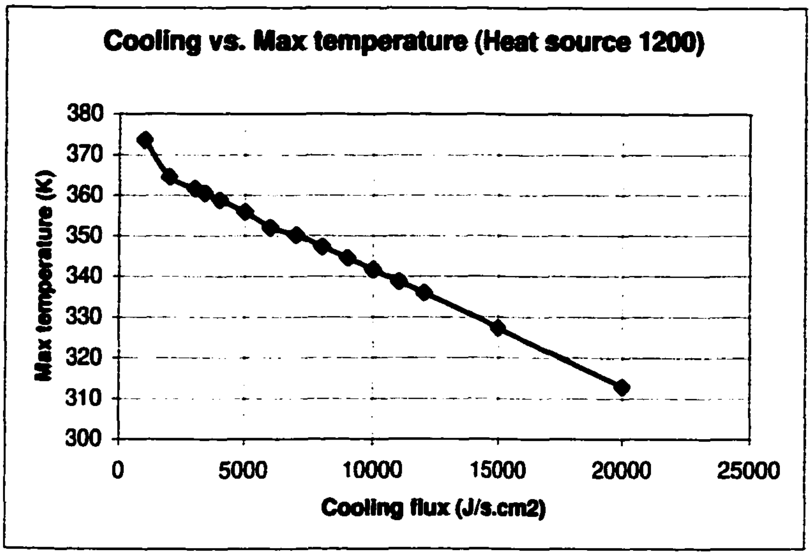

(a) Maximum temperature vs. cooling

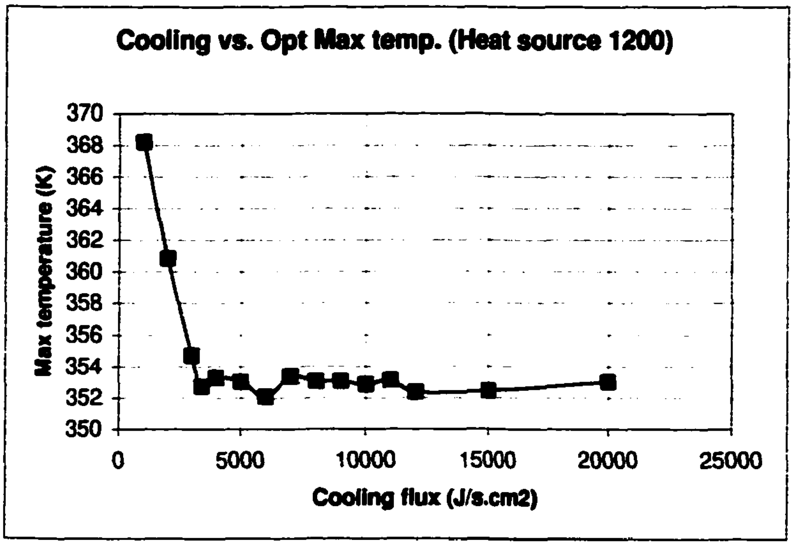

(b) Optimal maximum temperature vs. cooling

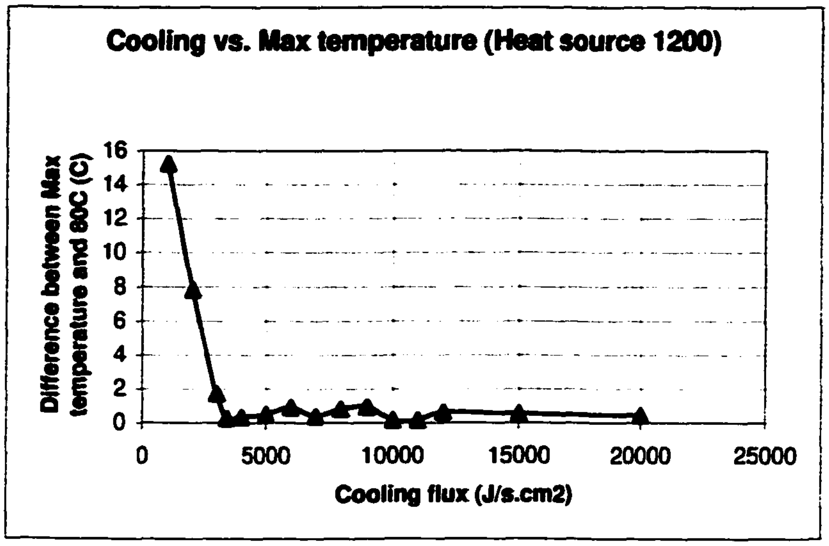

(c) Minimized temperature difference vs. cooling

Figure 6-11 Maximum temperature and cooling for heat flux 1200 $J/s\times m^2$

Table 6-5 shows that the optimal cooling flux value reaches 6,217 $J/s\times m^2$, when considering both geometric parameters *W* and *H*, and cooling as the third design variable. The optimization for 6,000 $J/s\times m^2$ has no noticeable change because it is very close to the optimal temperature. Even though the values of optimal geometry are different, the plate can maintain ideal optimal temperature for a broad range of cooling conditions, as shown in Figures 6-11 (a), (b), and (c).

Figure 6-11 (a) indicates that the maximum temperature has almost a linear relation to the cooling flux, while increased cooling leads to decreased maximum temperature. Figure 6-11 (b) shows that the minimum cooling of 3,000 $J/s\times m^2$ is required to achieve the ideal operating temperature 353 ^oK (80 ^oC), with various flow channel geometry. Obviously, when the cooling flux increases, the range of the optimal channel geometry becomes broader. Figure 6-11 (c) further presents the same relation of Figure 6-11 (b) using the minimized temperature difference $|MaxTemp\text{-}80^oC|$.

Figures 6-12 (a) ~ (c) present the same relations as Figures 6-11 (a) ~ (c), using heat source flux of 9,500 $J/s\times m^2$, corresponding to the low voltage and high current density fuel cell operating point shown in Figures 5-1 and 5-2, respectively. The minimum cooling flux of 15,000 $J/s\times m^2$ is needed to ensure that the plate be able to operate at the temperature around 353 ^oK (80 ^oC), as in Figure 6-12 (b).

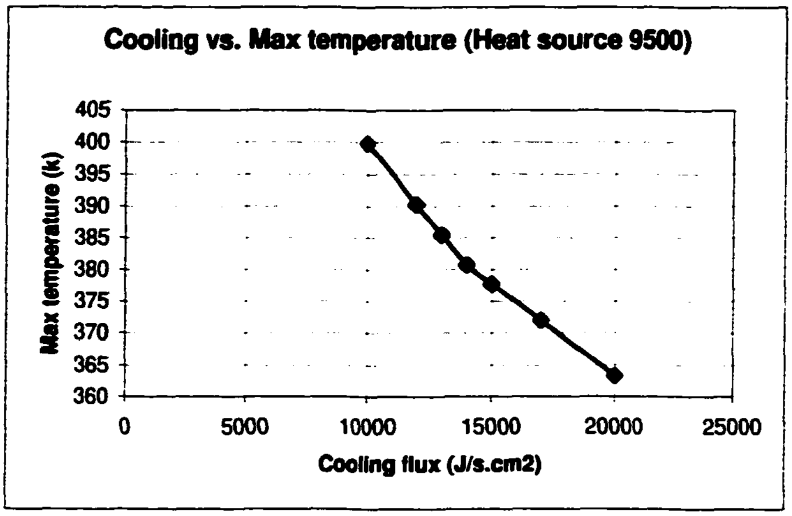

(a) Maximum temperature vs. cooling

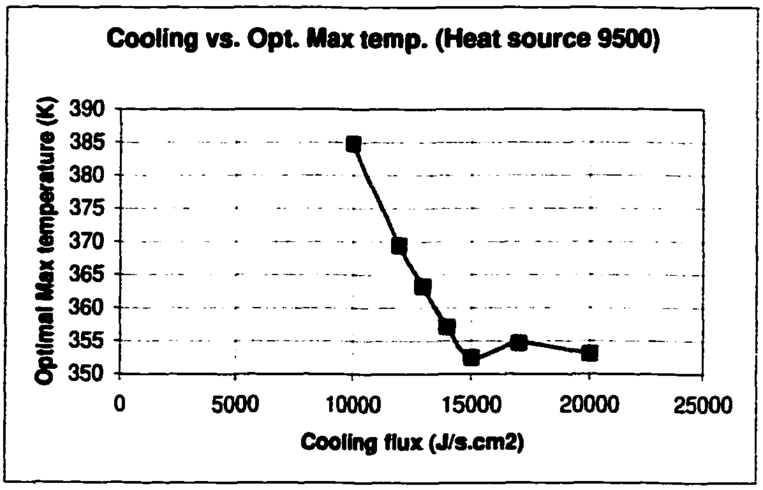

(b) Optimal maximum temperature vs. cooling

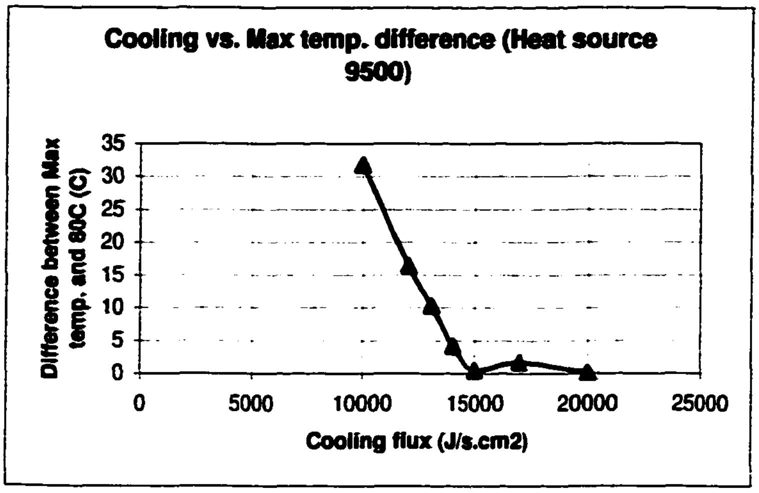

(c) Minimized temperature difference vs. cooling

Figure 6-12 Maximum temperature and cooling for heat flux 9500 $J/s\times m^2$

Comparing Figures 6-11 (a) ~ (c) and Figures 6-12 (a) ~ (c), heat source flux increased 8 times, while the cooling flux need increased only 5 times (15,000 over 3,000 $J/s\times m^2$). This allows a broader range of possibility for plate design. The corresponding relation in Figures 5-2 and 5-3 shows that the heat flux increases faster than the power density increases during the fuel cell current density increasing. The needed cooling flux does not increase as fast as the heat source flux. This compensates the "slower" power density increase when using high current density. The discussion we have on cooling only deals with the required minimum cooling flux for fuel cell plate operating at a temperature around 353 ^oK (80 ^oC), while the optimization of flow field geometry and its robustness have not been considered. This optimization is very important to the design of the fuel cell plate.

In summery, in the thermal design optimization of a fuel cell plate, the minimum cooling flux value for a functional fuel cell plate is identified. This method of study is very similar to that in the structure integrity, while the unknown mechanical performance is used. The only difference between structure and thermal studies is that in structure design the unknowns are both design objective and design variables, while in thermal design the unknowns are both boundary condition and design variables.

Chapter 7. Global Design Optimization and Its Solution

The design of fuel cell plate involves considerations from many related disciplines, ranging from fuel cell performance, manufacturability, structure integrity, and thermal consideration, to material development. The ideal method for identifying the design optimum is to formulate a design optimization problem globally to incorporate all of these considerations, through a combination of analytical models and computer analyses/simulations. However, this ideal method is far from mature, and tremendous amount of research involving a huge amount of experimental and theoretical work needs to be done.

Some simulation methods consider fluid-structure interaction between structure aspect and fluid performance. This coupling effect applies large geometry deformation from the fluid analysis to the nonlinear geometry structure consideration. Others consider thermal-structure effect using temperature distribution from the thermal analysis as thermal load on the structure analysis. Both are not suitable to the fuel cell plate due to the fact that no large deformation is allowed and a "fixed" temperature is desired in the study.

The step-by-step optimization method that has been discussed previously in Section 6.3 presents a traditional global optimization method. An iterative process was introduced to connect the CFD-based, flow channel performance design optimization with the FEA-based, flow channel structure design optimization. However, there is no guarantee that the method will converge and deliver a solution to the global optimal design, although the introduced procedure made it possible to automate the design optimization process to replace trial and error tests with efficient optimization search.

In this chapter, two different platforms for carrying out design optimization are presented, the interdisciplinary design optimization method and the multidisciplinary design optimization method. The optimizations are carried either with a focus on a specific aspect of fuel cell plate performance, or based upon the synthesis on several aspects of fuel cell plate performance.

7.1 Interdisciplinary Design Optimization

Interdisciplinary design optimization is formulated to maximize the average oxygen concentration at the MEA interface in the air delivery channel of the fuel cell plate, as shown in Equation 6-4. Structure integrity and operating temperature are used as design constraints. The optimization is formulated as:

$$\max_{D_1,D_2} \left[\frac{1}{n}\sum_{i=1}^{n} Y_{O_2}^{MEA}\right] \tag{7-1}$$

$$\text{subject to} \qquad \sigma_{vm} < [\sigma_{vm}{}^{o}]$$

$$\text{and} \qquad |MaxTemp\text{-}80^{o}C| < [\Delta T^{o}]$$

The first design constraint is defined using the structure integrity requirement discussed previously in Section 6.3. The maximum von Mises stress, σ_{vm}, is controlled. The second design constraint represents the thermal performance consideration discussed previously in Section 6.4. A maximum fuel cell operating temperature around 80 ^{o}C ensures high power output and long operation life.

The design variables considered in the design optimization include those that define the geometry of the plate, while all others are problem specific. The fuel cell operating temperature is desired to have a "fixed" value of $80^{o}C$ and is thus not considered as a design variable.

In this study, sensitivity study was carried out with the shared geometry parameters and design variables. The specific variables that only influence the objective function or one of the two constraints are considered as aspect-specific variables. For simplicity, sensitivity on these aspect-specific variables was omitted in the global optimal design. In sensitivity analysis, the influence of design variables on the constraint functions was first accessed for given constraint limits of $[\sigma_{vm}{}^{o}]$ and $[\Delta T^{o}]$. The stress limit $[\sigma_{vm}{}^{o}]$ represents the minimum maximum stress that the material can bear. A commonly used bottom value of 20 *MPa* for graphite particle reinforced polymer composite material was used.

The limit on allowed temperature variation, $[\Delta T^o]$, was selected to be $5\ ^oC$, according to the common sense on PEM fuel cell operation.

According to the analysis results presented in Figures 6-11 (a) and (b) of Section 6.4.2, for a given heat source of 1,200 $J/s{\cdot}m^2$ in the thermal design, the maximum allowed temperature change of $[\Delta T^o] = 5\ ^oC$ will allow the fuel cell plate geometric parameters to vary over a very broad range. Meanwhile, in the strength oriented single disciplinary optimization (Section 6.3.3), the maximum stress level remains below 20 *MPa*, regardless of the geometry parameters (Figure 6-8). Thus the optimal design using geometry variables has no major influence on the thermal and/or structure design constraints. The global design optimization based on the interdisciplinary formulation in the study can be carried as single disciplinary optimization on the objective function, without considering the constraint functions in Equation 7-1.

7.2 Multidisciplinary Design Optimization

7.2.1 Formulation

Global optimal design based on multiple objective optimization has been growing rapidly to accommodate concurrent engineering research over the past two decades. Optimization is a very effective tool to allow multiple performance measures to be jointly evaluated to reach an optimal design. Xue and Dong [Xue 1998] used the combined measure on performances and costs to formulate the balanced performance and cost design of a PEM fuel cell system, considering several key design parameters:

$$\max_{w.r.t.d} I(d) = \lambda_F I^{(F)}(d) + \lambda_C I^{(C)}(d) \qquad (7\text{-}2)$$

where, $I^{(F)}(d)$ is functional performance and $I^{(C)}(d)$ represents production cost; λ_F and λ_C are weight factors on performance and costs, respectively. Xue's work applied an analytical model to measure fuel cell performance. In this work, numerical virtual models are used without considering costs.

The multiple objective design function is defined in a general vector expression as:

$$F(X) = [f_1(X), f_2(X), f_3(X)] \tag{7-3}$$

Using a preference function in the form of

$$P[F(X)] = w_1 f_1(X) + w_2 f_2(X) + w_3 f_3(X) \tag{7-4}$$

$$0 \leq w_i \leq 1 \qquad i = 1,2,3$$

$$w_1 + w_2 + w_3 = 1$$

The substitute problem under this weighted sum strategy becomes

$$\underset{X \in R^3}{Maximize}\ P[F(X)] = w_1 f_1(X) + w_2 f_2(X) + w_3 f_3(X) \tag{7-5}$$

Since $f_1(X)$, $f_2(X)$, and $f_3(X)$ represents aspect functional performance of different nature, their values are normalized with respect a given design to make them comparable.

$$I_1(X) = \frac{f_1(X) - F_1^{ref}}{|F_1^{ref}|} \tag{7-6}$$

$$I_2(X) = \frac{f_2(X) - F_2^{ref}}{|F_2^{ref}|} \tag{7-7}$$

$$I_3(X) = \frac{f_3(X) - F_3^{ref}}{|F_3^{ref}|} \tag{7-8}$$

The given reference design, represented by F_1^{ref}, F_2^{ref} and F_3^{ref} in three different perspectives, allows the global design optimization to be unified [Xue 1998]. The general global multiple objective optimization problem based on Equation 7-5 is formulated as:

$$\underset{X \in R^3}{Maximize}\ P[I(X)] = w_1 I_1(X) + w_2 I_2(X) + w_3 I_3(X) \tag{7-9}$$

This chapter focuses on the quantitative analyses using CFX and ANSYS for carrying out the global design optimization. The design is based on virtual prototype development, where no specific configuration of the fuel cell plate, even its material, is given. The approach thus requires a more generic understanding on the reference design used to integrate the multiple objective design optimization. In this work, the aspect functional performances of $f_1(X)$, $f_2(X)$, and $f_3(X)$ correlate to oxygen concentration (fluid dynamics), structure and thermal considerations, respectively. The selection of F_1^{ref}, F_2^{ref} and F_3^{ref} is no longer based on a specific physical configuration of the plate. Instead, three equivalent physics states of the plate from the oxygen concentration (fluid dynamics), structure and thermal aspects are selected. These are the minimum average oxygen level state, F_1^{ref}, the maximum allowed stress state, F_2^{ref}, and the minimum operation temperature variation (or targeted operation temperature) state, F_3^{ref}.

The $f_1(X)$ and F_1^{ref} correspond to the average oxygen concentration in the CFD analysis, discussed in Chapters 3 and 6. The objective function $f_1(X)$ has the following form:

$$f_1(X) = \frac{1}{n}\sum_{i=1}^{n} Y_{O_2}^{MEA} \tag{7-10}$$

The term F_1^{ref} represents a specific value of the aspect objective $f_1(X)$. The value is calculated using the fuel cell plate parameters under one particular configuration. In this approach, the value of $F_1^{ref} = 6.187\%$, corresponding to the minimum average oxygen level as discussed previously in Chapter 6.

Similarly, the aspect objective function, $f_2(X)$, and its reference value, F_2^{ref}, for the maximum von Mises stress calculated using finite element structure analysis, discussed in Chapters 4 and 6, are used as the second contributing term of the multi-objective optimization. The aspect objective function, $f_2(X)$, is expressed as:

$$f_2(X) = \sigma_{VM} \tag{7-11}$$

The definition of F_2^{ref} is based on the yield stress value $[\sigma_{vm}^{o}]$, which specifies the maximum stress allowed in the structure. A commonly used value of 20 *MPa*, considered in the previous section for graphite particle reinforced polymer composite material, is used.

Following the same principle, the aspect performance objective, $f_3(X)$, measures the temperature distribution on the fuel cell plate using finite element thermal analysis, similar to the method discussed previously in Chapters 5 and 6:

$$f_3(X) = MaxTemp \tag{7-12}$$

In this case, the maximum temperature, rather than the temperature variation (as in Chapter 6), is used. The ideal fuel cell operating temperature 80 °C is used as the reference design, F_3^{ref}. The formulation of multi-objective function optimization using relative aspect performance reading automatically ensure that the maximum temperature at the MEA surface of fuel cell plate to be as close to 80 °C as possible:

$$I_3(X) = \frac{|f_3(X) - 80^oC|}{80^oC} \tag{7-13}$$

The general multi-objective optimization problem is then formulated as:

$$\underset{X \in R^3}{Maximize}\ \mathrm{P}[\mathbf{I}(X)] = w_1\,[\frac{f_1(X) - 6.187\%}{6.187\%}] -$$

$$- w_2\,[\frac{f_2(X) - 20}{20}] - w_3\,[\frac{|f_3(X) - 80^oC|}{80^oC}] \tag{7-14}$$

where, $f_1(X)$, $f_2(X)$, and $f_3(X)$ are defined through Equations 7-10, 7-11 and 7-12, respectively. The three aspect objectives come from the three disciplinary functional performances, and contribute to the multi-disciplinary optimization problem. In this study, only shared design variables, geometry dimensions, are considered.

The objective of this multi-disciplinary optimization is to identify the optimal fuel plate design that provides the highest level of oxygen concentration along the MEA surface in the oxygen flow channel, requires the lowest performance material for making the flow channels, and ensures the fuel cell to operate at a temperature very close to the desired 80 °C. The approach combines fuel cell performance enhancement through oxygen concentration, material development requirement through the stress level control, as well as stability of fuel cell operating temperature into a single design process.

In this study, the geometry model of the fuel cell plate used in CFD is not the same as those used in structure and thermal analyses. This undesirable mismatch is caused by the limitations of the present commercial CAE codes CFX and ANSYS. Both of these two packages have been discussed in previous chapters.

7.2.2 Approximate Solution of the Formulated Optimization Problem

The multi-disciplinary optimization problem defined by Equation 7-14 is solved using a trial and error approach with the models from Chapters 3, 4 and 5. The fluid dynamics trial and error results are presented in Figure 6-3. The structure integrity analysis is carried out using the nonlinear geometry model (8) from Table 4-2. The thermal analysis is based on the results from MEA reaction heat source of q = 1200 $J/s{\cdot}m^2$ and the negative flux value of 3400 J/sm^2 for cooling, which are discussed previously in Section 5.3.

For the ease of calculation, the preference weighting factors, w_1, w_2, w_3, are assumed to be equal, 1/3, 1/3, 1/3. In practical optimal design, different weighting factors can be used by a designer based on the specific application.

The shared design variables used in the multi-disciplinary optimization are flow channel height, H, and channel width, w, as shown in Figure 6-1 of the CFD analysis. The channel height is same as the layer thickness of solid model given in Figure 4-1 used for structure and thermal integrity. The channel width relates to the channel wall width, W, based on the Equation 6-6, where the square plate side length is selected as $D = 0.055626$ m. The values of H, w and/or W, according to 3-m19 to 3-m28 in Table 6-1 and Figure 6-3, are given in Table 7-1. The corresponding values of $f_1(X)$, $f_2(X)$, $f3(X)$, $w_1I_1(X)$, $w_2I_2(X)$, $w_3I_3(X)$, as well as the objective function $P[I(X)]$ are also given in the Table.

Table 7-1 Results of multi-disciplinary optimization

(H, w) *mm*	**$f_1(X)$, (O_2,%)**	**(H, W) *mm***	**$f_2(X)$, (σ_{vm}, *MPa*)**	**$f_3(X)$, (T_{Max} °C)**	**$w_1I_1(X)$**	**$w_2I_2(X)$**	**$w_3I_3(X)$**	**$P[I(X)]$**
(1, 1.5)	7.205	(1, 1.64)	18.04	80.28	0.0548	-0.0327	0.0012	0.0863
(1, 2)	7.130	(1, 1.18)	17.39	83.48	0.0508	-0.0435	0.0145	0.0798
(1, 2.5)	7.089	(1, 0.71)	16.73	87.13	0.0486	-0.0545	0.0297	0.0734
(1.5, 1.5)	6.888	(1.5, 1.64)	17.60	86.42	0.0378	-0.040	0.0268	0.0510
(1.5, 2)	6.768	(1.5, 1.18)	17.35	88.48	0.0313	-0.0442	0.0353	0.0487
(1.5, 2.5)	6.691	(1.5, 0.71)	16.98	90.69	0.0272	-0.0503	0.0445	0.0330
(2, 1.5)	6.491	(2, 1.64)	17.80	89.83	0.0164	-0.0367	0.0410	0.0121
(2, 2)	6.290	(2, 1.18)	17.92	91.22	0.0055	-0.0347	0.0468	-0.0066
(2, 2.5)	6.187	(2, 0.71)	19.49	93.17	0	-0.0085	0.0549	-0.0464

Figures 7-1 (a), (b) and (c) illustrate the contributions from each disciplinary objective, $w_1I_1(X)$, $w_2I_2(X)$, $w_3I_3(X)$, and their relations to the design variables (H, w). The objective function of the multi-disciplinary optimization problem $P[I(X)]$ is also given in Figure 7-1 (d).

The solution of the multi-disciplinary optimization shows that the oxygen enhancement contributes most among the three disciplinary aspects. The optimal design ends up with small values for both channel height H, and channel width w, leading to higher wall thickness. At this configuration, the structure stress is at the modest level, while the maximum plate temperature is very close to the desired operating 80 °C. The result provides general guidelines for fuel cell plate design.

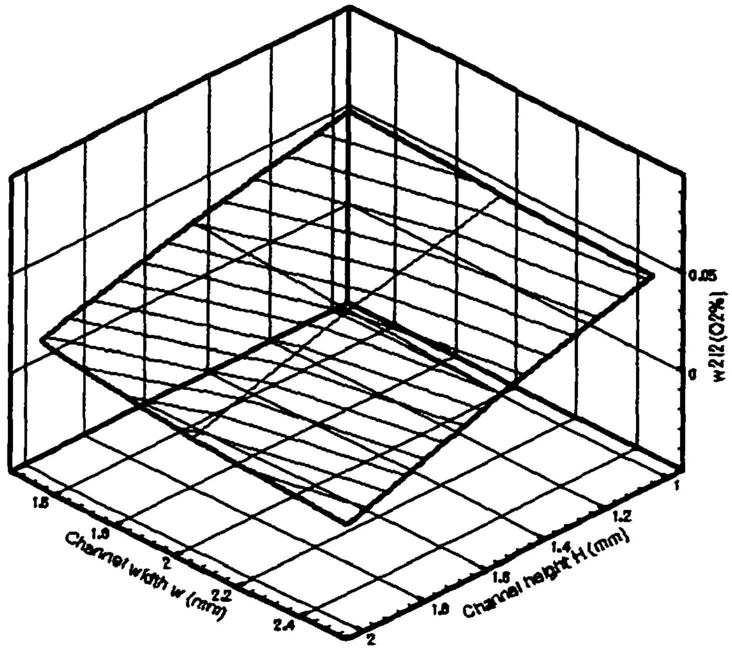

(a) Contribution of oxygen enhancement effect, $w_1I_1(X)$

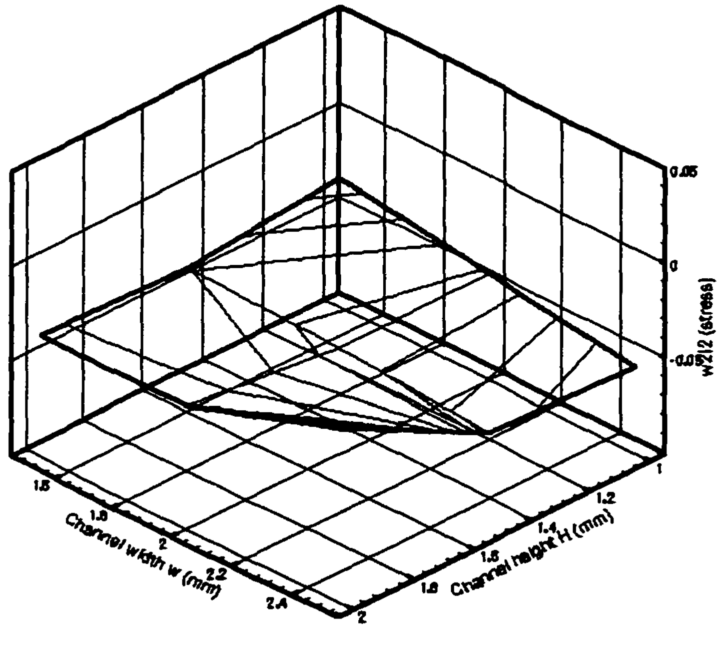

(b) Contribution of structure stress effect, $w_2I_2(X)$

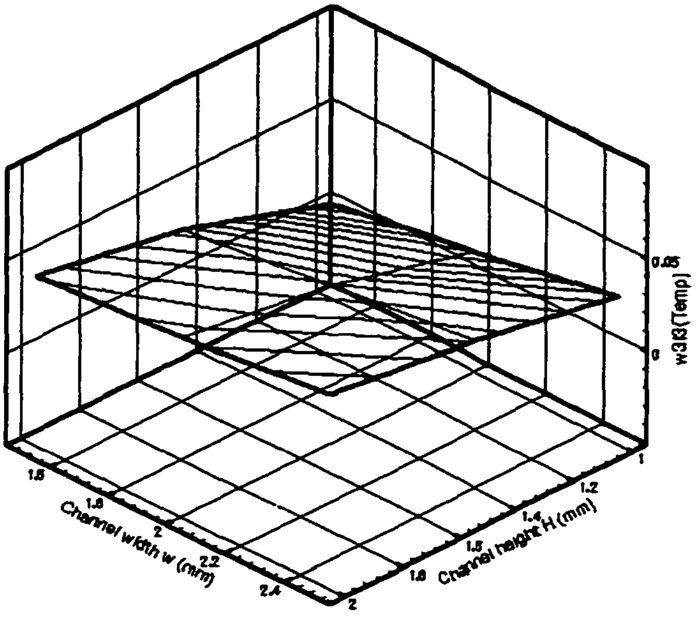

(c) Contribution of thermal temperature effect, $w_3I_3(X)$

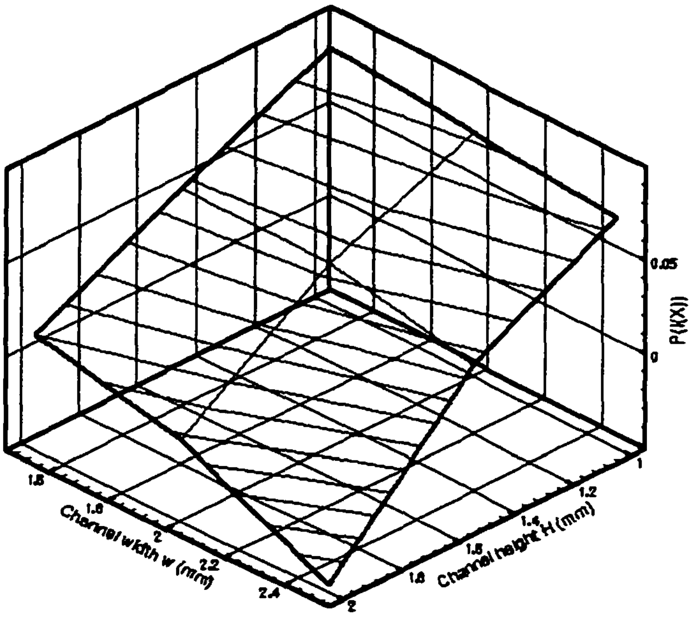

(d) Objective Function $P[I(X)]$

Figure 7-1 Solution of multi-disciplinary optimization problem

Chapter 8. Conclusion

8.1 Summary

This research focuses on the new techniques for the rapid prototype development of PEM fuel cell gas delivery plates. The study addresses several key issues in the design, analysis, and manufacturing of fuel cell plates. The approach combines theoretical modeling, experimental study, physical plate making process, and virtual prototyping to form a new scheme for the rapid prototype development of fuel cell plates. Relations among the contributing aspects and to the rapid prototype development technique are illustrated in Figure 8-1.

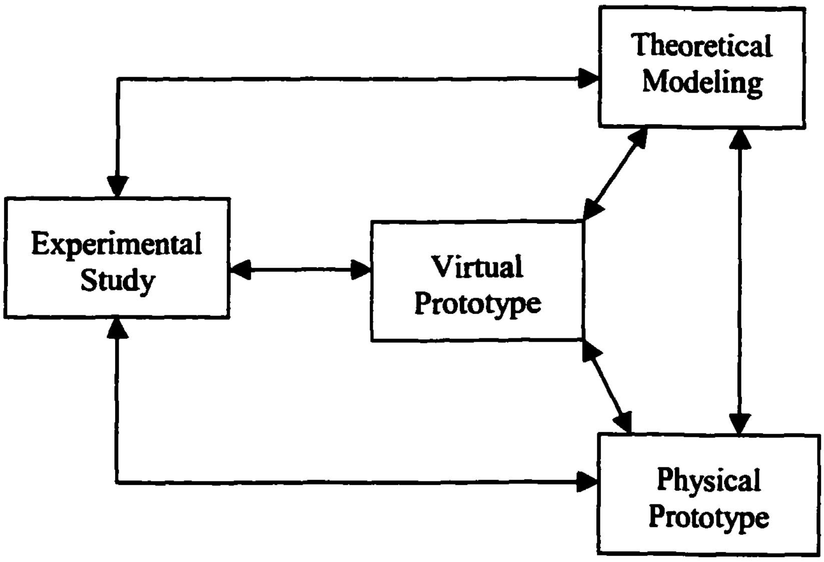

Figure 8-1 Rapid prototype development and its contributing elements

In the traditional product development approach, activities are limited to the outer circle of Figure 8-1. In the proposed approach, virtual prototyping acts as a bridge to connect all the three aspects, provides more information to accelerate the theoretical modeling and experimental development work, and speeds up (or even substitutes) the physical prototype development. Meanwhile, the research also indicates that rapid prototype development relies on the maturity of theoretical and experimental work, such as CFD models and the stability of conductive materials.

Applying the rapid prototype development approach to PEM fuel cell gas delivery plates, this research applies the concurrent engineering design approach to simultaneously incorporate multidisciplinary performance considerations, including conductive polymer composite material development, flow channel plate computational design, and thermal consideration. This product development method avoids mistakes made by conflict aspect designs and reduces design iterations.

8.2 Research Contributions

The presented research contributes to both of the new technology for PEM fuel cell gas delivery plate development, and the generic, virtual prototyping and rapid prototyping based concurrent engineering design methodology, especially for products made of composite materials. Specifically, the research contributions can be summarized into the following aspects:

- Development of promising composite materials for producing fuel cell gas delivery plates through screen-printing layer deposition method

  The study has identified the cause of the problem with the poster-ink based screen-print ink material, explored various alternative composite ink materials, and narrowed down to the promising "conductive polymer ~ epoxy ~ graphite power" composite. A new, concurrent approach for developing new composite materials through various experiments and material tests has been introduced, and demonstrated through the development of one particular ink composite with promising results.

- Performance evaluation through virtual prototyping

In this research, the method for virtual prototyping fuel cell gas delivery plate using advanced CAD/CAE commercial software, including Pro/ENGINEER parametric design modeling tool, CFX computational fluid dynamics analysis tool, Pro/MECHANICA Structure and ANASYS finite element analysis tools, is introduced. The method allows a "virtual prototype" of the fuel cell plate to be constructed and the performance of the plate to be evaluated through various analyses as "virtual prototype tests." These include the prediction of fuel cell performance, given the plate and flow field geometry, through the CFD calculation on the average oxygen concentration level at the MEA interface; as well as the assessments of the maximum stress and the largest, undesirable temperature variation on the printed fuel cell plate, given plate geometry and material composition. These new virtual prototype making and testing methods integrate the advanced CAD/CAE tools to form a systematic approach for designing and analyzing a new fuel cell plate design.

- Disciplinary design optimization

The presented research on virtual prototyping not only serves as design performance evaluation tools. They also form the foundation for disciplinary design optimizations for maximum fuel cell power output, broadest range for composite material properties, and minimum deviation from the desired fuel cell operation temperature. Three separated design optimization problems have been formed and solved using virtual prototyping tools to evaluate the design objectives and constraints. These evaluations include CFX based calculation on the average oxygen concentration level at the MEA interface for given plate and flow field geometry, FEA based structure analysis to assess the maximum stress, and FEA based thermal analysis to calculate the temperature variation on the printed fuel cell plate. In addition to the full utilization of the build-in capabilities of the FEA software, integration of optimization research codes into the CFX package to implement the design optimization has been carried out and achieved satisfactory results.

- New fuel cell flow field and gas delivery plate design method

  The computer modeling and CFD analysis of the fuel cell flow field and gas delivery plate allows the fuel cell performance to be quantitatively predicted through the calculation on the average oxygen concentration at the MEA interface, and the fuel cell flow field features to be optimized to achieve best fuel cell performance. This study supported the introduction of a new fuel cell flow field design principle and associated structures, and contributed to a new invention filed as a US patent.

- Multidisciplinary design optimization

  Integrating the newly introduced disciplinary design optimizations based on the three aspects of the fuel cell gas delivery plate design, the virtual prototyping based, multi-disciplinary global design optimization problem for fuel cell gas delivery plate is introduced. Detailed implementations on the formulation of the design objective and constraints are presented. Solution to the complex global design optimization problem through step-by-step analysis is discussed. This research forms the foundation for future work in the global design optimization for key fuel cell components.

The newly introduced approach for the rapid development of fuel cell plates has a great potential to be applied to the development of other mechanical parts. The technique is particularly suitable for multiple functional components, such as smart structure. The study also extends the general methodology of computational design and rapid prototyping.

8.3 Potential Industry Impact

Gas delivery plates contribute to a large proportion of the cost for a PEM fuel cell stack, and forms a major obstacle to the commercialization of this promising, zero-emission power plant technology. The cost of traditional graphite plate production method is hard to reduce. Application of composites is a promising alternative to considerably lower the cost of fuel cell plates, combining with an appropriate manufacturing technique such as screen-printing. This research provides new methods for developing conductive polymer composites as the ink materials for screen-printed fuel cell plates, as well as material performance evaluation methods. As an early stage of the composites study, the research provides a feasible development direction to this materials series. A concurrent method for optimizing fuel cell plates through material design for optimal material composition is provided.

After decades of research and development, the performance of PEM fuel cell has been much improved. At present, most development task concentrates on the cost reduction of materials and manufacturing process. The rapid prototype development approach presented in this work supports the "rapid" progress on the experimental and theoretical developments, and reduces physical prototype work. Application of this technique has the potential to accelerate the commercialization of fuel cells.

8.4 Future Work

This study addresses an array of very complex and multi-disciplinary research topics, covering parametric solid modeling, computational fluid mechanics simulation, structure and thermal analyses, single and multiple disciplinary design optimization, as well as composite material development and testing. Much of the research can be extended and carried out in a greater depth.

First, the material development for the fuel cell gas delivery plates is a very challenge task. More conductive polymer materials used as modifier need to be examined and tested. More mature material testing technique should also be applied on the concurrent method for composite material development.

Secondly, the multi-disciplinary design optimization presented in this study followed a trial and error method. A fully integrated and automated optimization process is needed to identify the true global design optimum. This requires the integration of the CFD, structure and thermal analyses codes into one software package, as well as the ability to introduce a shared set of design variables that unites the CFD, structure and thermal models. These integrations will support further study on the global design optimization and sensitivity analysis on various design attributes. Many theoretical and implementation issues need to be addressed.

Bibliography

[Aarts 1989] Aarts, E. and Korst, J., *Simulated Annealing and Boltzmann Machines*, Wiley, 1989.

[Abou khachfe 2001] Abou khachfe, R., and Jarny, Y., Determination of Heat Sources and Heat Coefficient for Two-dimensional Heat Flow – Numerical and Experimental Study, International Journal of Heat and Mass Transfer v44, p1309-1322, 2001.

[Akin 1990] Akin, J. Ed, *Computer-Assisted Mechanical Design*, Prentice Hall, 1990.

[Amphlett 1995] Amphlett, J. C., Baumert, R. W., Mann, R. F., Peppley, B. A., and Roberge, P. R., Performance Modeling of the Ballard Mark IV Solid Polymer Electrolyte Fuel Cell, - I. Mechanistic Model Development, Journal of the Electrochemical Society, v142, n1, p1-8, January 1995.

[Amphlett 1995] Amphlett, J. C., Baumert, R. W., Mann, R. F., Peppley, B. A., and Roberge, P. R., Performance Modeling of the Ballard Mark IV Solid Polymer Electrolyte Fuel Cell, - II. Empirical Model Development, Journal of the Electrochemical Society, v142, n1, p9-15, January 1995.

[ANSYS] ANSYS Manual.

[Armi 1999] Armi, R. K. and Gupta, S. K., Manufacturability analysis for solid freeform fabrication, *Proceedings of 1999 ASME design engineering technical conferences*, Las Vegas, NV, DETC99/DFM-8903.

[Ashley 1995] Ashley, S., Rapid Prototyping is Coming of Age, *Mechanical Engineering*, pp. 62-68, July 1995.

[Ashley 1997] Ashley, S., From CAD Art to Rapid Metal Tools, *Mechanical Engineering*, p82-87, March 1997.

[Ashley 1998] Ashley, S., RP Industry's Growing Pains, *Mechanical Engineering*, p64-67, July 1998.

[Ashby 1992] Ashby, M.F., *Materials Selection in mechanical Design*, Pergamon Press, 1992.

[ASM International] ASM International, Engineered Materials Handbook, TheMaterials Information Society.

[Baxter 1999] Baxter, S. F., Battaglia, V. S., and White, R. E., Methanol Fuel Cell Model: Anode, Journal of the Electrochemical Society, v146, n2, p437-447, 1999.

[Bell] Bell labs net library, //netlib.bell-labs.com/netlib/

[Benjeddou 1999] Benjeddou, A., Trindade, M. A., and Ohayon, R., New Shear Actuated Smart Structure Bean Finite Element, AIAA Journal, v37, n3, p378-383, March 1999.

[Binder 1998] Binder, M., Status of U.S. stationary power plant development, *Proceedings of 1998 Fuel Cell Seminar*, p5-8

[Blomen 1993] Blomen, L. J. M. J., Mugerwa, M. N., Fuel Cell Systems, Plenum Press, 1993.

[Boyer 1998] Boyer, C. C., Anthony, R. G. and Appleby, A. J., An analytical model for single cell PEMFC performance and its use in the evaluation of oxygen enrichment, *Proceedings of 1998 Fuel Cell Seminar*, p422-425.

[Brombacher 1992] Brombacher, A. C., *Reliability by Design*, Wiley Publisher, 1992.

[Busick 1998] Busick, D. N., and Wilson, M. S., Low-cost Composite Materials for PEFC Bipolar Plates, Proceedings of 1998 Fuel Cell Seminar, *Proceedings of 1998 Fuel Cell Seminar*, p632-635.

[Cham 1999] Cham, J. G., Pruitt, B. L., Cutkosky, M. R., Binnard, M., Weiss, L. E. and Neplotnik, G., Layered manufacturing with embedded components: process planning considerations, *Proceedings of 1999 ASME design engineering technical conferences*, Las Vegas, NV, DETC99/DFM-8910

[Chang 1999] Chang, K. H., Silva, J. and Bryant, I., Concurrent design and manufacturing for mechanical systems, *Proceedings of 1999 ASME design engineering technical conferences*, Las Vegas, NV, DETC99/DFM-8911.

[Chen 1989] Chen, C., Kong, W. C., and Cha, J. Z., "An Equality Constrained RQP Algorithm Based on the Augmented Lagrangian Penalty Function", ASME Journal of Mechanisms, Transmissions, and Automation in Design, v111, pp368-375, 1989.

[Chua 1997] Chua Chee Kai and Leong Keh Fai, *Rapid Prototyping: Principles and Applications in Manufacturing*, John Wiley & Sons, Inc., 1997.

[Chung 1994] Chung, D. L., *Carbon Fiber Composites*, Butterworth-Heinemann, 1994.

[Chandrupatla 1998] Chandrupatla, T. R., An efficient quadratic fit-Sectioning algorithm for minimization without derivatives, *Comput. Methods Appl. Mech. Engrg.* 152, (1998) 211-217.

[Chalk 1998] Chalk, S. G., and Venkateswaran, S. R., Is there a continuing role for the federal government in fuel cell R&D for transportation? *Proceedings of 1998 Fuel Cell Seminar*, p222-225

[Dong 2001] Dong, W., Beale, S. B., and Boersma, R. J., Computational Modeling of Solid Oxide Fuel Cells, Proceedings of the 9th Annual Conference of the CFD Society of Canada, Waterloo, Ontario, May 27-29, 2001.

[Dong 1994] Dong, Z., "Engineering Optimization and Its Application", Laboratory Manual, Department of Mechanical Engineering, University of Victoria, 1994.

[Dong 1998] Dong, Z. et al, "Oxygen enhancing flow-field design, principle and structures", NGFT Invention Memo, June 1998

[Dong 1999a] Dong, Z., "Fuel Cell Flow-Field Structure Formed by Layer Deposition," UK Patent GB 2 336 712 A, October 27, 1999.

[Dong 1999b] Dong, Z., "Fuel Cell Stack Assembly," Patent Cooperation Treaty Patent WO 99/57781, November 11, 1999.

[Dong 1999c] Dong, Z., Wang, G., Zheng, R., and Mackie, R., "Rapid Prototype Development for Fuel Cell Components and Stacks," *Abstract in the Proceedings of the 9th Canadian Hydrogen Conference*, Vancouver, BC, Canada, February 7-10, 1999.

[Dong 2000] Dong, Z., Kratschmar, K., Lu, D., Zheng, R., *et al*, "Improved Oxidant Flowfield for Solid Polymer Electrolyte Fuel Cell," US Patent $^{\#}$09-749-495, Filed on December 22, 2000.

[Dutta 2001] Dutta, S., Shimpalee, S., and Van Zee, J. W., Numerical Prediction of Mass-exchange between Cathode and Anode Channels in a PEM Fuel Cell, International Journal of Heat and Mass Transfer, v44, p2029-2042, 2001.

[Ferreira 93] Ferreira, A.G., and Zerovnik, J., *Bounding the probability of success of stochastic methods for global optimization*, 25, No.10/11, p1-8, 1993.

[Fleury 1979] Fleury, C., Structural weight optimization by dual method of convex programming, International *Journal for numerical methods in engineering*, v14, p1761-1783, 1979.

[Fuel Cell Handbook] Fuel Cell Handbook (Fifth Edition), EG&G Services Parsons, Inc. Science Applications International Corporation, U.S. Department of Energy, Office of Fossil Energy, National Energy Technology Laboratory, P.O. Box 880, Morgantown, WV 26507-0880, October 2000.

[Goffe 1994] Goffe, W.L., Ferrier, G.D., and Rogers, J., Global optimization of statistical functions with simulated annealing, *Journal of Econometrics*, 60 p65-99, 1994.

[Gul' 1996] Gul', V. E., *Structure and Properties of Conducting Polymer Composites*, VSP, 1996.

[Hilton 1995] Hilton, P., Making the Leap to Rapid Tool Making, *Mechanical Engineering*, p75-76, July 1995.

[Honig 1995] Honig, J. M., Thermodynamics, 2nd Edition, Academic Press, 1995.

[Hsueh 1991] Hsueh, Y., A program package for global optimization using the simulated annealing, MS thesis, State University of New York at Buffalo, 1991.

[Hummel 1985] Hummel, R. E., *Electronic Properties of Materials*, Springer-Verlag, 1985.

[Kalivas 1989] Kalivas, J.H., Roberts, N. and Sutter J.M., Global optimization by simulated annealing with wavelength selection for ultraviolet-visible spectrophotometry, *Analytical Chemistry*, 61, p2024-2030, 1989.

[Kaskimies 1999] Kaskimies, J., Gas Flow on the Cathod of a Solid Polymer Fuel Cell, Master Thesis, Helsinki University of Technology, 1999.

[Kays 1993] Kays, W. M., Crawford, M. E., Convective Heat and Mass Transfer, McGraw-Hill, 1993.

[Kirkpatrick 1983] Kirkpatrick, S., Gelatt, C.D. and Vecchi, M.P., Optimization by Simulated Annealing, *Science*, 220 13 May 1983, No. 4598, p671-680.

[Kordesch 1996] Kordesch, K., and Simader, G., Fuel Cells and their Applications, VCH, 1996.

[Kratschmar 1997] Kratschmar, K., Conductive Ink Report, NGFT, University of Victoria, July 2, 1997.

[Kratschmar 1998] Kratschmar, K., Screen Printing Summery Report, IESVic, University of Victoria, April 28, 1998.

[Kratschmar 2001] Kratschmar, K., Pastula, M., Wang, G., Merida, W., and Dong, Z., Heat Balance of an Air-cooled Proton Exchange Membrane Fuel Cell: Theoretical Modeling and Experimental Verification, Proceedings of the 11th Canadian Hydrogen Conference, Victoria, BC, Canada, June 2001.

[Lampinen 1993] Lampinen, M. J., and Fomino, M., Analysis of Free Energy and Entropy Changes for Half-Cell Reactions, Journal of the Electrochemical Society, v140, n12, p3537-46, December, 1993.

[Ledjeff-Hey 1998] Ledjeff-Hey, K., Mahlendorf, F., Niemzig, O., and Trautmann, A., Electronically Conducting Composite Materials as Bipolar Plates for PEM Fuel Cells, *Proceedings of 1998 Fuel Cell Seminar*, p570-573.

[Lee 1995] Lee, G., Virtual Prototyping on Personal Computers, *Mechanical Engineering*, p70-73, July 1995.

[Li 1998] Li, K. Y., and Yam, L. H., An optimization design method for large scale structures, *Comput. Methods Appl. Mech. Engrg.* 165 (1998) 273-289.

[Liu 1999] Liu, L., Possible advantage of nonlinear over linear analysis for design, *Proceedings of 1999 ASME design engineering technical conferences*, Las Vegas, NV, DETC99/RSAFP-8857.

[Lombardi 1998] Lombardi, M. and Haftka, R.T., Anti-optimization technique for structural design under load uncertainties, *Computer methods in applied mechanics and engineering*, v157, 1998, p19-31.

[Lu 1998] Lu, Dongming, Progress Report, CFD, 1998.

[Mackie 1999] Mackie, Ryan, NGFT Progress Report, Oxygen Enrichment using Flow Disturbances, 1999.

[Mallant 1994] Mallant, R.K.A.M., etc., Solid Polymer Fuel Cell Research at ECN, *Proceedings of Fuel Cell Seminar*, 1994, p503.

[Menon 1998] Menon, U., Chapter 6: Rapid Prototyping of Hardware and Software, Concurrent Design of Products, *Manufacturing Processes and Systems*, Gordon and Breach Science publishers, p133, 1998.

[Milliken 1998] Milliken, J., The DOE transportation fuel cell program: national laboratory/industry interactions, *Proceedings of 1998 Fuel Cell Seminar*, p246-249.

[Oldham 1994] Oldham, H.B. and Myland, J.C., *Fundamentals of Electrochemical Science*, Academic Press, Inc. 1994.

[Ohsaki 1998] Ohsaki, M., Uetani, K., and Takeuchi, M., Optimization of imperfection-sensitive symmetric systems for specified maximum load factor, *Comput. Methods Appl. Mech. Engrg.* 166 (1998) 349-362.

[Ozisik 1985] Ozisik, M. N., Heat Transfer – A Basic Approach, McGraw-Hill Book Company, 1985.

[Pastula 1997] Pastula, M. E., Radiator Stack PEM Fuel Cell Architecture, System Modeling and Flow Field Design, M. A. Sc. Thesis, University of Victoria, 1997.

[Patnaik 1998] Patnaik, S. N., and Hopkins, D. A., Optimality of a fully stressed design, *Comput. Methods Appl. Mech. Engrg.*, 165 (1998) 215-221.

[Perry 1997] Perry, M. L., Screen Printing of Fuel and Oxidant Delivery Plates: A Low Cost Manufacturing Alternative, M. A. Sc. Thesis, University of Victoria, 1997.

[Plowman 1994] Plowman, K. R., Rehg, T. J., Nandapurkar, P. J., and Door, R. D., Targets and progress toward improved membrane electrode assemblies for PEM fuel cells, *Proceedings of 1994 Fuel Cell Seminar*, p470-473.

[Polycarpou 1997] Polycarpou, A. C., Tirkas, P. A., and Balanis, C. A., The Finite Element Method for Modeling Circuits and Interconnects for Electronic Packaging, IEEE Transactions on Microwave Theory and Techniques, v45, n10, p1868-1874, October 1997.

[Postek 1980] Postek, M. T., Howard, K. S., Johnson, A. H., and McMichael, K. L., *Scanning Electron Microscopy, A Student Handbook*, Ladd Research Ind. Inc., 1980.

[Parametric 1999] Parametric Technology, *Pro/ENGINEER Manuals*.

[Parametric 1999] Parametric Technology, *Pro/MECHANICA Manuals*, 1999.

[Perry 1998] Perry, M. L., Newman, J., and Cairns, E. J., Mass Transport in Gas Diffusion Electrodes: A Diagnostic Tool for Fuel Cell Cathodes, Journal of the Electrochemical Society, v145, n1, p5-15, January, 1998.

[Pirondi 1998] Pirondi, A., Nicoletto, G., Cova, P., Pasqualetti, M., Portesine, M., and Zani, P. E., Thermo-Mechanical Simulation of a Multichip Press-Packed IGBT, Solid-State Electronics, v42, n12, p2303-2307, 1998.

[Qiu 1998] Qiu, Z., and Elishakoff, I., Antioptimization of structures with large uncertain-but non-random parameters via interval analysis, *Comput. Methods Appl. Mech. Engrg.*, 152 (1998) 361-372.

[Ronne 1995] Ronne, J., Cost Reductions of Bipolar Plates for SPFCs, *NGFT*, University of Victoria, August 30, 1995.

[Schaub 1998] Schaub, D, and Chu, K-R., Chapter 7: Rapid Prototyping, Concurrent Design of Products, *Manufacturing Processes and Systems*, Gordon and Breach Science publishers, p153, 1998.

[Scholta 1997] Scholta, J., Rohland, B., and Garche, J., Surface conductivity and stability of bipolar plate materials for polymer membrane fuel cells in contact with Nafion, *New materials for fuel cell and modern battery systems II*, 1997, p330-334.

[Shi 1995] Shi, L. T., and Tu, K. N., Finite Element Stress Analysis of Failure Mechanisms in a Multilevel Metallization Structure, Journal of Applied Physics, v77, n7, p3037-3041, 1 April 1995.

[Singh 1999] Singh, D., Lu, D.M., and Djilali, N., A two-dimensional analysis of mass transport in proton exchange membrane fuel cells, *International Journal of Engineering Science*, 37, (1999) 431-452.

[Tautsher 1991] Tautsher, C. J., *Contamination Effects on Electronic Products*, Marcel Dekker Inc., 1991.

[Thirumalai 1997] Thirumalai, D., and White, R. E., "Mathematical Modeling of Proton Exchange Membrane Fuel Cell Stacks", Journal of the Electrochemical Society, v144, n5, p1717-1723, May 1997.

[Thomas 1992] Thomas, S. M., "Stereolithography Simplifies Tooling for Reinforced Rubber Parts", *Mechanical Engineering*, p62-66, July 1992.

[Trimmer 1997] Trimmer, W., *Micromechanics and MEMS*, Classic and Seminal Papers to 1990, *IEEE press*, Jan. 1997.

[U Quebec 1999] University of Quebec, *Lecture Notes on Rapid Prototyping*, Web-site: //ecoleing.uqtr.uquebec.ca/geniedoc/gmm/RP_GENER.HTM.

[Vliet 1999] Vliet, J. W. van, Luttervelt, C. A. van and Kals, H. J. J., "State-of the art report on design for manufacturing", *Proceedings of 1999 ASME design engineering technical conferences*, Las Vegas, NV, DETC99/DFM-8970.

[Voss 1993] Voss, H., et al., "Coolant Flow Field Plates for Electrochemical Fuel Cell", Ballard Power Systems, U.S. patent, 5,230,966, July 27, 1993x.

[Voss 1995] Voss, H., et al., "Anode water removal: A water removal management and diagnostic technique for solid polymer fuel cells", *Electrochemica Acta*, 40, 3, 1995, p321-328.

[Wang 1999] Wang, G., "A Quantitative Concurrent Engineering Design Method Using Virtual Prototyping-based Global Optimization and Its Application in Transportation Fuel Cell", Ph.D. dissertation, 1999.

[Warsi 1999] Warsi, Z. U. A., Fluid Dynamics: Theoretical and Computational Approaches, 2nd Edition, CRC Press, 1999.

[Watkins 1992] Watkins, D. S., et al, "Fuel cell fluid flow field plate", Ballard Power Systems, U.S. patent, 5,108,849, April 28, 1992.

[Watkins 1994] Watkins, D. S., et al, "Development of a PEM power plant for stationary power application", *Proceedings of 1994 Fuel Cell Seminar*, p250-252.

[Weisbrod 1996] Weisbrod, K. R. and Vanderborgh, N. E., "Modeling of Gaseous Flows within proton exchange membrane fuel cells", *Proceedings of 1996 Fuel Cell Seminar*, p635-638.

[Wessling 1998] Wessling, B., "Dispersion as the Link between Basic Research and Commercial Applications of Conductive Polymers (Polyaniline)", *Synthetic Metals*, 93, p143-154, 1998.

[Wetton 1999] Wetton, B., "Water movement in channels", *MMSC Ballard project meeting*, Ballard Headquarters, Oct. 5, 1999.

[Wilkinson 1997] Wilkinson, D. P., and Steck, A. E., "General progress in the research of solid polymer fuel cell technology at Ballard", *New materials for fuel cell and modern battery systems II*, 1997, p27-35.

[Wohlers 1992] Wohlers, T., "CAD Meets Rapid Prototyping", Computer Aided Engineering, v11, n4 April 1992.

[Xue 1997] Xue, D., and Dong, Z., "Coding and clustering of design and manufacturing feathers for concurrent design", *Computers in Industry*, 34, p139-153, 1997.

[Xue 1998] Xue, D., and Z. Dong, "Optimal Fuel Cell System Design Considering Functional Performance and Production Costs," *Journal of Power Sources*, Vol. 76, 1998, pp.69-80.

[Yang 1997] Yang, S. And Nezu, K., "Concurrent Engineering Design of Sheet Stamping by Using An Inverse FE Approach," *Proceedings Of 1997 ASME Design Engineering Technical Conferences*, Sacramento, CA, DETC97/DTM-3901.

[Yi 1999] Yi, J. S., and Nguyen, T. V., "Multicomponent Transport in Porous Electrodes of Proton Exchange Membrane Fuel Cells Using the Interdigitated Gas Distributors", Journal of the Electrochemical Society, v146, n1, p38-45, 1999.

[Yin 2001] Yin, Z., Ding, H., and Xiong, Y., "Virtual Prototyping of Mold Design: Geometric Mouldability Analysis for Near-net-shape Manufactured Parts by Feature Recognition and Geometric Reasoning", Computer-Aided Design, v33 p137-154, 2001.

[Zapach 1993] Zapach, T. G., "The Calculation of Flow and Heat Transfer over Surface Mounted Ribs using a Domain Decomposition Method." Master thesis, University of Victoria, 1993.

[Zeidan 1995] Zeidan, E-S. B., "A Numerical Study of Two- and Three-Dimensional Turbulent Obstacle Flows, Master thesis, University of Victoria, 1995.

Appendix A. Main Fortran routine used in REQPAL for integrating optimization code to CFX code

The routine was original made by S. Liu [Dong 1994] and extended by Rong Zheng for automated CFD design optimization.

```
      PROGRAM main21
c     USE DFPORT
      USE PORTLIB
      PARAMETER(N=2)
      implicit real*8 (a-h,o-z)
      dimension x(N), xl(N), xu(N)
      common/gradflag/gf,gc
      common/para/acc,rm,sfd,print
      INTEGER(4) I, errnum
      data nc,ne,nl/0,0,0/
c     data x/-1.0,1.0/
      data x/0.29,0.04/
c     data xl/-5.0,0.0/
c     data xu/10.0,15.0/

      data xl/0.10,0.005/
      data xu/0.35,0.15/
      gf='n'
      gc='n'
      acc=1.d-08
      rm=5.
      sfd=1.d-3
      print='n'
      write (*,*) acc, sfd
      call REQPAL(N,nc,ne,nl,x,xl,xu)
c     call CFXTEST(N,nc,ne,nl,x,xl,xu)
      stop
      end
      subroutine functf(X,f)
      USE PORTLIB
      implicit real*8 (a-h,o-z)
      dimension X(2)
      INTEGER(4) I, errnum
      IST = INT (X(1)*1000+0.5 )
      IFN = INT ((X(1)+X(2))*1000+0.5 )


      OPEN(2,FILE='E:/temp/testinput.dat',
     +  STATUS = 'UNKNOWN')

       WRITE(2,*) IST, IFN
```

```
      CLOSE (2, STATUS = 'KEEP')


      I = SYSTEM("E:\\CFX4.2\\bin\\runsolve4 -c m08.fc -f m08.f")
      If (I .eq. -1) then
      errnum = ierrno( )
      print *, 'Error ', errnum
      end if

      OPEN(1,FILE='E:/temp/testoutput.dat',
    + STATUS = 'UNKNOWN')

      READ(1,*) foutput

      f=-foutput
C1010 FORMAT (f12.5)
     CLOSE (1, STATUS = 'KEEP')


     OPEN(3,FILE='E:/temp/test.dat',POSITION= 'APPEND',
    + STATUS = 'UNKNOWN')
     WRITE(3,*) X, -f
     CLOSE (3, STATUS = 'KEEP')

    I = SYSTEM("del E:\temp\*.dump.*")
    If (I .eq. -1) then
    errnum = ierrno( )
    print *, 'Error ', errnum
    end if

    I = SYSTEM("del E:\temp\*.out.*")
    If (I .eq. -1) then
    errnum = ierrno( )
    print *, 'Error ', errnum
    end if
     return
     end
     subroutine functc(X,c)
     implicit real*8 (a-h,o-z)
     dimension X(2)
     return
    end
     subroutine gradf(x,gf)
     implicit real*8 (a-h,o-z)
     dimension x(2)
     return
     end
     subroutine gradc(x,gc)
     implicit real*8 (a-h,o-z)
     dimension x(2)
     return
     end
```

Appendix B. CFX program code for CFD simulation and automated design optimization

The code was original developed by Dongming Lu, then later extended and modified by Rong Zheng for moving boundary definition to integrate the optimization code REQPAL.

```
/**********************************************************/
/* TEST                                                   */
/* LAMINAR FLOW IN MEA + CHANNEL CONFIGURATION            */
/* COMPRESSIBLE, NON-ISOTHERMAL                           */
/* POROUS REGIONS                                         */
/* MASS TRANSFER EQUATIONS ADDED                          */
/**********************************************************/
>>CFX4
  >>SET LIMITS
    TOTAL INTEGER WORK SPACE 50000000
    TOTAL CHARACTER WORK SPACE 80000
    TOTAL REAL WORK SPACE 80000000
    MAXIMUM NUMBER OF BLOCKS 10
    MAXIMUM NUMBER OF PATCHES 10000
    MAXIMUM NUMBER OF INTER BLOCK BOUNDARIES 20
  >>OPTIONS
    THREE DIMENSIONS
    HEAT TRANSFER
    COMPRESSIBLE FLOW
    MASS FRACTION EQUATIONS 1
  >>USER FORTRAN
    USRTRN
    USRTPL
  >>VARIABLE NAMES
    MASS FRACTION1 'O2'
>>MODEL TOPOLOGY
/*  >>CREATE BLOCK
    BLOCK NAME 'BLOCK1'
    BLOCK DIMENSIONS 700 20 20
  >>CREATE PATCH
    PATCH NAME 'CSRC'
    BLOCK NAME 'BLOCK1'
    PATCH TYPE 'USER3D'
    PATCH LOCATION 1 700 1 1 1 20
  >>CREATE PATCH
    PATCH NAME 'INLETC'
    BLOCK NAME 'BLOCK1'
    PATCH TYPE 'INLET'
    LOW I
  >>CREATE PATCH
    PATCH NAME 'OUTLETC'
    BLOCK NAME 'BLOCK1'
    PATCH TYPE 'PRESSURE BOUNDARY'
    HIGH I */
/*  >>CREATE PATCH
    PATCH NAME 'RIB'
    BLOCK NAME 'BLOCK1'
```

```
    PATCH TYPE 'SOLID'
    PATCH LOCATION 290 330 11 20 1 20 */
/*  >>CREATE PATCH
    PATCH NAME 'RIB1'
    BLOCK NAME 'BLOCK1'
    PATCH TYPE 'SOLID'
    PATCH LOCATION 610 660 11 20 1 20 */
>>MODEL DATA
  >>SOURCES
    PATCH NAME 'CSRC'
    TOTAL
    O2 -8.70800E-08 0.000000E+00
  >>TITLE
    PROBLEM TITLE 'LAMINAR FLOW IN A SQUARE CHANNEL WITH A BUMP'
  >>PHYSICAL PROPERTIES
    >>STANDARD FLUID
      FLUID 'AIR'
      STANDARD FLUID REFERENCE TEMPERATURE 3.5600E+02
    >>COMPRESSIBILITY PARAMETERS
      FULLY COMPRESSIBLE
      UNIVERSAL GAS CONSTANT 8.3140E+03
      FLUID MOLECULAR WEIGHT 2.8790E+01
      REFERENCE PRESSURE 3.0390E+05
    >>HEAT TRANSFER PARAMETERS
      ENTHALPY REFERENCE TEMPERATURE 3.4000E+02
    >>MASS TRANSFER PARAMETERS
      >>DIFFUSIVITIES
        O2 2.8200E-06
      >>MOLECULAR WEIGHTS
        O2 3.2000E+01
      >>SPECIFIC HEATS
        O2 9.420000E+02
>>SOLVER DATA
  >>PROGRAM CONTROL
    MAXIMUM NUMBER OF ITERATIONS 2
    MINIMUM NUMBER OF ITERATIONS 2
    OUTPUT MONITOR BLOCK 'BLOCK1'
    OUTPUT MONITOR POINT 25 10 10
    MASS SOURCE TOLERANCE 1.0000E-10
  >>ALGEBRAIC MULTIGRID PARAMETERS
    WORK SPACE FACTOR 5.0000E+00
  >>EQUATION SOLVERS
    PRESSURE 'AMG'
  >>REDUCTION FACTORS
    PRESSURE 5.0000E-02
  >>SWEEPS INFORMATION
    >>MAXIMUM NUMBER
      PRESSURE 50
>>CREATE GRID
  >>SIMPLE GRID
    BLOCK NAME 'BLOCK1'
    DX 700* 1.000000E-04
    DY 20* 4.000000E-05
    DZ 20* 7.500000E-05
    X START 0.0000E+00
    Y START 0.0000E+00
    Z START 0.0000E+00
```

```
>>MODEL BOUNDARY CONDITIONS
  >>INLET BOUNDARY CONDITIONS
    VELOCITY SPECIFIED
  >>SET VARIABLES
    PATCH NAME 'INLETC'
    U VELOCITY 1.5640E-01
    TEMPERATURE 3.6300E+02
    O2 2.1800E-01
  >>SET VARIABLES
    PATCH NAME 'OUTLETC'
    PRESSURE 0.0000E+00
  >>WALL BOUNDARY CONDITIONS
    PATCH NAME 'WALL'
    TEMPERATURE 3.5300E+02
>>OUTPUT OPTIONS
  >>PRINT OPTIONS
    >>WHAT
      NO VARIABLES
      NO RESIDUAL HISTORY
      NO WALL PRINTING
  >>LINE GRAPH DATA
    EACH ITERATION
    FILE NAME 'RESIDUALS'
    ALL VARIABLES
    RESIDUAL
>>STOP
```

Appendix C. Fortran routine for integrating CFX code and REQPAL code

The program was developed and extended by Rong Zheng based on the commercial package.

```
      SUBROUTINE USRTRN(U,V,W,P,VFRAC,DEN,VIS,TE,ED,RS,T,H,RF,SCAL,
     +                  XP,YP,ZP,VOL,AREA,VPOR,ARPOR,WFACT,CONV,IPT,
     +                  IBLK,IPVERT,IPNODN,IPFACN,IPNODF,IPNODB,IPFACB,
     +                  WORK,IWORK,CWORK)
C
C***********************************************************************
C
C  USER SUBROUTINE TO ALLOW USERS TO MODIFY OR MONITOR THE SOLUTION AT
C  THE END OF EACH TIME STEP
C  THIS SUBROUTINE IS CALLED BEFORE THE START OF THE RUN AS WELL AS AT
C  THE END OF EACH TIME STEP
C
C  >>> IMPORTANT                                                    <<<
C  >>>                                                              <<<
C  >>> USERS MAY ONLY ADD OR ALTER PARTS OF THE SUBROUTINE WITHIN   <<<
C  >>> THE DESIGNATED USER AREAS                                    <<<
C
C***********************************************************************
C
C  THIS SUBROUTINE IS CALLED BY THE FOLLOWING SUBROUTINES
C     CUSR  TRNMOD
C
C***********************************************************************
C  CREATED
C     27/04/90  ADB
C  MODIFIED
C     05/08/91  IRH  NEW STRUCTURE
C     01/10/91  DSC  REDUCE COMMENT LINE GOING OVER COLUMN 72.
C     29/11/91  PHA  UPDATE CALLED BY COMMENT, ADD RF ARGUMENT,
C                    CHANGE LAST DIMENSION OF RS TO 6 AND IVERS TO 2
C     05/06/92  PHA  ADD PRECISION FLAG AND CHANGE IVERS TO 3
C     03/07/92  DSC  CORRECT COMMON MLTGRD.
C     23/11/93  CSH  EXPLICITLY DIMENSION IPVERT ETC.
C     03/02/94  PHA  CHANGE FLOW3D TO CFDS-FLOW3D
C     22/08/94  NSW  MOVE 'IF(IUSED.EQ.0) RETURN' OUT OF USER AREA
C     19/12/94  NSW  CHANGE FOR CFX-F3D
C
C***********************************************************************
C
C  SUBROUTINE ARGUMENTS
C
C    U      - U COMPONENT OF VELOCITY
C    V      - V COMPONENT OF VELOCITY
C    W      - W COMPONENT OF VELOCITY
C    P      - PRESSURE
C    VFRAC  - VOLUME FRACTION
```

```
C      DEN    - DENSITY OF FLUID
C      VIS    - VISCOSITY OF FLUID
C      TE     - TURBULENT KINETIC ENERGY
C      ED     - EPSILON
C      RS     - REYNOLD STRESSES
C      T      - TEMPERATURE
C      H      - ENTHALPY
C      RF     - REYNOLD FLUXES
C      SCAL   - SCALARS (THE FIRST 'NCONC' OF THESE ARE MASS FRACTIONS)
C      XP     - X COORDINATES OF CELL CENTRES
C      YP     - Y COORDINATES OF CELL CENTRES
C      ZP     - Z COORDINATES OF CELL CENTRES
C      VOL    - VOLUME OF CELLS
C      AREA   - AREA OF CELLS
C      VPOR   - POROUS VOLUME
C      ARPOR  - POROUS AREA
C      WFACT  - WEIGHT FACTORS
C      CONV   - CONVECTION COEFFICIENTS
C
C      IPT    - 1D POINTER ARRAY
C      IBLK   - BLOCK SIZE INFORMATION
C      IPVERT - POINTER FROM CELL CENTERS TO 8 NEIGHBOURING VERTICES
C      IPNODN - POINTER FROM CELL CENTERS TO 6 NEIGHBOURING CELLS
C      IPFACN - POINTER FROM CELL CENTERS TO 6 NEIGHBOURING FACES
C      IPNODF - POINTER FROM CELL FACES TO 2 NEIGHBOURING CELL CENTERS
C      IPNODB - POINTER FROM BOUNDARY CENTERS TO CELL CENTERS
C      IPFACB - POINTER FROM BOUNDARY CENTERS TO BOUNDARY FACESS
C
C      WORK   - REAL WORKSPACE ARRAY
C      IWORK  - INTEGER WORKSPACE ARRAY
C      CWORK  - CHARACTER WORKSPACE ARRAY
C
C    SUBROUTINE ARGUMENTS PRECEDED WITH A '*' ARE ARGUMENTS THAT MUST
C    BE SET  BY THE USER IN THIS ROUTINE.
C
C    NOTE THAT OTHER DATA MAY BE OBTAINED FROM CFX-F3D USING THE
C    ROUTINE GETADD, FOR FURTHER DETAILS SEE THE VERSION 4
C    USER MANUAL.
C
C**********************************************************************
C
C
      LOGICAL LDEN,LVIS,LTURB,LTEMP,LBUOY,LSCAL,LCOMP
     +       ,LRECT,LCYN,LAXIS,LPOROS,LTRANS
C
      CHARACTER*(*) CWORK
C
C++++++++++++++++ USER AREA 1 ++++++++++++++++++++++++++++++++++++++++++
C---- AREA FOR USERS EXPLICITLY DECLARED VARIABLES
C
C++++++++++++++++ END OF USER AREA 1 +++++++++++++++++++++++++++++++++++
C
      COMMON
     + /ALL/    NBLOCK,NCELL,NBDRY,NNODE,NFACE,NVERT,NDIM
     + /ALLWRK/ NRWS,NIWS,NCWS,IWRFRE,IWIFRE,IWCFRE
     + /ADDIMS/ NPHASE,NSCAL,NVAR,NPROP
     +         ,NDVAR,NDPROP,NDXNN,NDGEOM,NDCOEF,NILIST,NRLIST,NTOPOL
```

```
     + /CHKUSR/ IVERS,IUCALL,IUSED
     + /CONC/   NCONC
     + /DEVICE/ NREAD,NWRITE,NRDISK,NWDISK
     + /IDUM/   ILEN,JLEN
     + /LOGIC/  LDEN,LVIS,LTURB,LTEMP,LBUOY,LSCAL,LCOMP
     +         ,LRECT,LCYN,LAXIS,LPOROS,LTRANS
     + /MLTGRD/ MLEVEL,NLEVEL,ILEVEL
     + /SGLDBL/ IFLGPR,ICHKPR
     + /SPARM/  SMALL,SORMAX,NITER,INDPRI,MAXIT,NODREF,NODMON
     + /TIMUSR/ DTUSR
     + /TRANSI/ NSTEP,KSTEP,MF,INCORE
     + /TRANSR/ TIME,DT,DTINVF,TPARM
C
C++++++++++++++++ USER AREA 2 +++++++++++++++++++++++++++++++++++++++++
C---- AREA FOR USERS TO DECLARE THEIR OWN COMMON BLOCKS
C     THESE SHOULD START WITH THE CHARACTERS 'UC' TO ENSURE
C     NO CONFLICT WITH NON-USER COMMON BLOCKS
C
C++++++++++++++++ END OF USER AREA 2 ++++++++++++++++++++++++++++++++++
C
      DIMENSION
     + U(NNODE,NPHASE),V(NNODE,NPHASE),W(NNODE,NPHASE),P(NNODE,NPHASE)
     +,VFRAC(NNODE,NPHASE),DEN(NNODE,NPHASE),VIS(NNODE,NPHASE)
     +,TE(NNODE,NPHASE),ED(NNODE,NPHASE),RS(NNODE,NPHASE,6)
     +,T(NNODE,NPHASE),H(NNODE,NPHASE),RF(NNODE,NPHASE,4)
     +,SCAL(NNODE,NPHASE,NSCAL)
      DIMENSION
     + XP(NNODE),YP(NNODE),ZP(NNODE)
     +,VOL(NCELL),AREA(NFACE,3),VPOR(NCELL),ARPOR(NFACE,3)
     +,WFACT(NFACE),CONV(NFACE,NPHASE)
     +,IPT(*),IBLK(5,NBLOCK)
     +,IPVERT(NCELL,8),IPNODN(NCELL,6),IPFACN(NCELL,6),IPNODF(NFACE,4)
     +,IPNODB(NBDRY,4),IPFACB(NBDRY)
     +,IWORK(*),WORK(*),CWORK(*)
C
C++++++++++++++++ USER AREA 3 +++++++++++++++++++++++++++++++++++++++++
C---- AREA FOR USERS TO DIMENSION THEIR ARRAYS
C
C---- AREA FOR USERS TO DEFINE DATA STATEMENTS
C
C++++++++++++++++ END OF USER AREA 3 ++++++++++++++++++++++++++++++++++
C
C---- STATEMENT FUNCTION FOR ADDRESSING
      IP(I,J,K)=IPT((K-1)*ILEN*JLEN+(J-1)*ILEN+I)
C
C----VERSION NUMBER OF USER ROUTINE AND PRECISION FLAG
C
      IVERS=3
      ICHKPR = 1
C
C++++++++++++++++ USER AREA 4 +++++++++++++++++++++++++++++++++++++++++
C---- TO USE THIS USER ROUTINE FIRST SET IUSED=1
C
       IUSED=1
C
C++++++++++++++++ END OF USER AREA 4 ++++++++++++++++++++++++++++++++++
C
```

```
       IF (IUSED.EQ.0) RETURN
C
C---- FRONTEND CHECKING OF USER ROUTINE
       IF (IUCALL.EQ.0) RETURN
C
C+++++++++++++++ USER AREA 5 ++++++++++++++++++++++++++++++++++++++++
C
C---- EXAMPLE (SET TIME INCREMENT FOR NEXT TIME STEP)
C
C     DTUSR = 0.1
C
C----END OF EXAMPLE
C
C--  CALCULATE AVERAGE YO2 AT THE CATHODE-CHANNEL INTERFACE
  IF(KSTEP.EQ.NSTEP) THEN
  CALL GETSCA('O2',ISCO2,CWORK)
  IPHASE=1
  CALL IPREC('BLOCK1','BLOCK','CENTRES',IPT,
     +              ILEN,JLEN,KLEN,CWORK,IWORK)
C----  LOOP OVER CATHODE-CHANNEL INTERFACE
  SUMO21=0.0
  SUMAE1=0.0
  DO 103 K=1,KLEN
   DO 102 J=1,1
    DO 101 I=1,ILEN
    INODE=IP(I,J,K)
    IFACE=IPFACN(INODE,2)
    SUMO21=SUMO21+SCAL(INODE,IPHASE,ISCO2)*AREA(IFACE,2)
    SUMAE1=SUMAE1+AREA(IFACE,2)
 101  CONTINUE
 102  CONTINUE
 103  CONTINUE

  WRITE(NWRITE,*) 'AVG O2 B1', SUMO21/SUMAE1,'  AERA1=',SUMAE1

  OPEN(1,FILE='E:/temp/test.dat',POSITION= 'APPEND',
     +  STATUS = 'UNKNOWN')

  WRITE(1,*) SUMO21/SUMAE1

       CLOSE (1, STATUS = 'KEEP')

  ENDIF
C
C
C+++++++++++++++ END OF USER AREA 5 +++++++++++++++++++++++++++++++++
C
      RETURN
      END

      SUBROUTINE USRTPL(NBLOCK,NPATCH,NGLUE
     +                ,NDBLK,CBLK,INFPCH,CPATCH,INFGLU,IBBPP,IBBPD
     +                ,WORK,IWORK,CWORK)
C
C*********************************************************************
C
C   USER SUBROUTINE TO ADD GRID TOPOLOGY
```

```
C   NAMELY BLOCKS, PATCHES AND INTER-BLOCK BOUNDARIES.
C
C   >>> IMPORTANT                                                    <<<
C   >>>                                                              <<<
C   >>> USERS MAY ONLY ADD OR ALTER PARTS OF THE SUBROUTINE WITHIN   <<<
C   >>> THE DESIGNATED USER AREAS                                    <<<
C
C***********************************************************************
C
C   CALLED BY SUBROUTINE
C     CUSR  GETTPL
C
C***********************************************************************
C   CREATED
C      28/08/91  IRH
C   MODIFIED
C      05/09/91  IRH  CHANGE ICALL TO IUCALL
C      29/11/91  PHA  UPDATE CALLED BY COMMENT
C      03/06/92  PHA  ADD PRECISION FLAG AND CHANGE IVERS TO 2
C      10/02/93  NSW  CORRECT CALL TO GLUE IN EXAMPLE
C      24/01/94  IRH  CORRECT COMMENTS
C      22/08/94  NSW  MOVE 'IF(IUSED.EQ.0) RETURN' OUT OF USER AREA
C      29/09/94  BAS  NEW ARGUMENT LIST + EXAMPLE FOR UNMATCHED GRIDS
C      26/03/96  NSW  CORRECT COMMENTS ABOUT USRPCH
C
C***********************************************************************
C
C   SUBROUTINE ARGUMENTS
C
C     NBLOCK - TOTAL NUMBER OF BLOCKS
C     NPATCH - TOTAL NUMBER OF PATCHES
C     NGLUE  - TOTAL NUMBER OF GLUING OPERATIONS
C     NDBLK  - BLOCK SIZE ARRAY
C     CBLK   - BLOCK NAME
C     INFPCH - INTEGER PATCH DATA
C     CPATCH - PATCH NAME
C     INFGLU - INTEGER GLUE DATA
C     IBBPP  - UNMATCHED-GRID GLUE DATA (PATCH POINTERS)
C     IBBPD  - UNMATCHED-GRID GLUE DATA (PATCH DATA)
C
C     WORK   - REAL WORKSPACE ARRAY
C     IWORK  - INTEGER WORKSPACE ARRAY
C     CWORK  - CHARACTER WORKSPACE ARRAY
C
C   SUBROUTINE ARGUMENTS PRECEDED WITH A '*' ARE ARGUMENTS THAT MUST
C   BE SET  BY THE USER IN THIS ROUTINE.
C
C***********************************************************************
C
      CHARACTER*(*) CBLK,CPATCH,CWORK
C
C+++++++++++++++++ USER AREA 1 ++++++++++++++++++++++++++++++++++++++++++
C---- AREA FOR USERS EXPLICITLY DECLARED VARIABLES
C
C     THESE FOLLOWING CHARACTER VARIABLES ARE USED IN THE USER EXAMPLES
      CHARACTER*32  CNAME,CNAME1,CNAME2,CLIST1,CLIST2,CBLOCK
      CHARACTER*6 CTYPE
```

```
C
C++++++++++++++++ END OF USER AREA 1 ++++++++++++++++++++++++++++++++++
C
      COMMON
     + /ALLWRK/ NRWS,NIWS,NCWS,IWRFRE,IWIFRE,IWCFRE
     + /BBCYCL/ XCYCLE(3)
     + /BBDIM/  MBB, MBBPAT, MBBNOD, MBBNBR,
     +          MBB1, MBB2, MBB3, MBB4, MBB5,
     +          MBB6, MBB7, MBB8, MBB9, MBB10,
     +          MBB11, MBB12, MBB13, MBB14, MBB15,
     +          MBB16, MBB17, MBB18, MBB19, MBB20
     + /CHKUSR/ IVERS,IUCALL,IUSED
     + /DEVICE/ NREAD,NWRITE,NRDISK,NWDISK
     + /LIMTPL/ NBLMAX,NPCMAX,NGLMAX
     + /SGLDBL/ IFLGPR,ICHKPR
C
C++++++++++++++++ USER AREA 2 +++++++++++++++++++++++++++++++++++++++++
C---- AREA FOR USERS TO DECLARE THEIR OWN COMMON BLOCKS
C     THESE SHOULD START WITH THE CHARACTERS 'UC' TO ENSURE
C     NO CONFLICT WITH NON-USER COMMON BLOCKS
C
C++++++++++++++++ END OF USER AREA 2 ++++++++++++++++++++++++++++++++++
C
C
      DIMENSION WORK(NRWS),IWORK(NIWS),CWORK(NCWS)
     +,NDBLK(3,*),CBLK(*),INFPCH(9,*),CPATCH(2,*),INFGLU(5,*)
     +,IBBPP(MBB1,MBB2),IBBPD(MBB3)
C
C++++++++++++++++ USER AREA 3 +++++++++++++++++++++++++++++++++++++++++
C---- AREA FOR USERS TO DIMENSION THEIR ARRAYS
C
C     THESE FOLLOWING ARRAYS ARE USED IN THE USER EXAMPLES
      PARAMETER (MNAME1=10,MNAME2=10)
      DIMENSION CLIST1(MNAME1), CLIST2(MNAME2)
C
C---- AREA FOR USERS TO DEFINE DATA STATEMENTS
C
C++++++++++++++++ END OF USER AREA 3 ++++++++++++++++++++++++++++++++++
C
C----VERSION NUMBER OF USER ROUTINE AND PRECISION FLAG
C
      IVERS=3
      ICHKPR = 1
C
C++++++++++++++++ USER AREA 4 +++++++++++++++++++++++++++++++++++++++++
C---- TO USE THIS USER ROUTINE FIRST SET IUSED=1
C
       IUSED=1
C
C++++++++++++++++ END OF USER AREA 4 ++++++++++++++++++++++++++++++++++
C
       IF (IUSED.EQ.0) RETURN
C
C---- FRONTEND CHECKING OF USER ROUTINE
       IF (IUCALL.EQ.0) RETURN
C
C++++++++++++++++ USER AREA 5 +++++++++++++++++++++++++++++++++++++++++
```

```
C
C---- INFORMATION ON UTILITY ROUTINE BLOCK
C
C     BLOCKS ARE DEFINED BY CALLS TO THE SUBROUTINE BLOCK AS FOLLOWS
C
C     CALL BLOCK (CBLOCK,NI,NJ,NK,NBLOCK,NDBLK,CBLK)
C
C     THE BLOCK NAME 'CBLOCK' SHOULD BE AT MOST 32 CHARACTERS LONG.
C     NI,NJ,NK ARE THE BLOCK DIMENSIONS
C     THE OTHER ARGUMENTS SHOULD NOT BE ALTERED
C
C---- EXAMPLE: ADDING A BLOCK
C
      CBLOCK = 'BLOCK1'
      CALL BLOCK(CBLOCK,700,20,20,NBLOCK,NDBLK,CBLK)
C
C---- END OF EXAMPLE
C
C++++++++++++++++ END OF USER AREA 5 +++++++++++++++++++++++++++++++++
C
C++++++++++++++++ USER AREA 6 +++++++++++++++++++++++++++++++++++++++++
C
C---- INFORMATION ON UTILITY ROUTINE PATCH
C
C     PATCHES ARE DEFINED BY CALLS TO THE SUBROUTINE PATCH AS FOLLOWS
C
C     CALL PATCH (CTYPE,CNAME,CBLOCK
C    +           ,LABEL,IST,IFN,JST,JFN,KST,KFN,NWL
C    +           ,NBLOCK,NPATCH,NDBLK,CBLK,INFPCH,CPATCH)
C
C  THIS DEFINES A PATCH ON BLOCK NAMED CBLOCK (CHARACTER*32) WITH:
C
C      CTYPE  = CHARACTER*6 STRING SPECIFYING PATCH TYPE.
C               SEE BELOW FOR LIST OF VALID TYPES.
C
C      CNAME  = CHARACTER*32 STRING SPECIFYING PATCH NAME.
C
C      LABEL  = INTEGER LABEL (LABELS MUST BE POSITIVE AND CONTIGUOUS)
C
C      IST, IFN, JST, JFN, KST, KFN, NWL
C
C             = STARTING & FINISHING I,J,K INDICES POINTING TO PATCH
C               IN THE NWL-DIRECTION.
C
C               A VALUE OF NWL = 1-6 MUST BE SET FOR 2D PATCHES.
C               NWL SHOULD BE SET TO 0 FOR 3D PATCHES
C
C               HIGH I = 1
C               HIGH J = 2
C               HIGH K = 3
C               LOW I = 4
C               LOW J = 5
C               LOW K = 6
C
C     THE OTHER ARGUMENTS SHOULD NOT BE ALTERED
C
C  THE CURRENTLY VALID PATCH TYPES ARE:
```

```
C     'INLET ','OUTLET','PRESS ','SYMMET','WALL  ','CNDBDY','BLKBDY'
C     'SOLID ','SOLCON','POROUS'
C
C---- EXAMPLE: ADDING A PATCH
C
 OPEN(2,FILE='E:/temp/testinput.dat',
     +  STATUS = 'UNKNOWN')

 READ(2,*) IST, IFN

      CLOSE (2, STATUS = 'KEEP')

      LABEL  = 1
      CTYPE  = 'SOLID '
      CNAME  = 'RIB'
      CBLOCK = 'BLOCK1'
c      IST=290
c      IFN=330
      JST=11
      JFN=20
      KST=1
      KFN=20
C
C-- UTILITY ROUTINE ADDS INLET PATCH TO LOW I FACE
C
      CALL PATCH (CTYPE,CNAME,CBLOCK
     +            ,LABEL, IST,IFN,JST,JFN,KST,KFN, 0
     +            ,NBLOCK,NPATCH,NDBLK,CBLK,INFPCH,CPATCH)
C
C
      LABEL  = 1
      CTYPE  = 'USER3D'
      CNAME  = 'CSRC'
      CBLOCK = 'BLOCK1'
      IST=1
      IFN=700
      JST=1
      JFN=1
      KST=1
      KFN=20
C
C-- UTILITY ROUTINE ADDS INLET PATCH TO LOW I FACE
C
      CALL PATCH (CTYPE,CNAME,CBLOCK
     +            ,LABEL, IST,IFN,JST,JFN,KST,KFN, 0
     +            ,NBLOCK,NPATCH,NDBLK,CBLK,INFPCH,CPATCH)
C
C
      LABEL  = 1
      CTYPE  = 'INLET '
      CNAME  = 'INLETC'
      CBLOCK = 'BLOCK1'
      IST=1
      IFN=1
      JST=1
      JFN=20
      KST=1
```

```
      KFN=20
C
C-- UTILITY ROUTINE ADDS INLET PATCH TO LOW I FACE
C
      CALL PATCH (CTYPE,CNAME,CBLOCK
     +            ,LABEL, IST,IFN,JST,JFN,KST,KFN, 4
     +            ,NBLOCK,NPATCH,NDBLK,CBLK,INFPCH,CPATCH)

C
C
      LABEL  = 1
      CTYPE  = 'PRESS '
      CNAME  = 'OUTLETC'
      CBLOCK = 'BLOCK1'
      IST=700
      IFN=700
      JST=11
      JFN=20
      KST=1
      KFN=20
C
C-- UTILITY ROUTINE ADDS INLET PATCH TO LOW I FACE
C
      CALL PATCH (CTYPE,CNAME,CBLOCK
     +            ,LABEL, IST,IFN,JST,JFN,KST,KFN, 1
     +            ,NBLOCK,NPATCH,NDBLK,CBLK,INFPCH,CPATCH)
C
C
      LABEL  = 2
      CTYPE  = 'SOLID '
      CNAME  = 'RIB1'
      CBLOCK = 'BLOCK1'
      IST=610
      IFN=660
      JST=11
      JFN=20
      KST=1
      KFN=20
C
C-- UTILITY ROUTINE ADDS INLET PATCH TO LOW I FACE
C
      CALL PATCH (CTYPE,CNAME,CBLOCK
     +            ,LABEL, IST,IFN,JST,JFN,KST,KFN, 0
     +            ,NBLOCK,NPATCH,NDBLK,CBLK,INFPCH,CPATCH)
C
C---- END OF EXAMPLE
C
C++++++++++++++++ END OF USER AREA 6 +++++++++++++++++++++++++++++++++++
C
C++++++++++++++++ USER AREA 7 ++++++++++++++++++++++++++++++++++++++++++
C
C
C---- INFORMATION ON UTILITY ROUTINE GLUE
C
C  INTER-BLOCK BOUNDARIES ARE DEFINED BY CALLS TO THE SUBROUTINE GLUE,
C  AS FOLLOWS:
C
```

```
C     CALL GLUE(CNAME1,CNAME2,NWL1,NWL2,NWL3
C    +         ,NBLOCK,NPATCH,NGLUE,NDBLK,INFPCH,CPATCH,INFGLU)
C
C  THIS GLUES TOGETHER TWO INTER-BLOCK BOUNDARY PATCHES WITH:
C
C      CNAME1 = NAME OF 1ST. INTER-BLOCK BOUNDARY PATCH
C      CNAME2 = NAME OF 2ND. INTER-BLOCK BOUNDARY PATCH
C      (NWL1,NWL2,NWL3) = ORIENTATION CHANGE OF HIGH I, HIGH J, HIGH K
C                         IN CROSSING FROM 1ST. BLOCK TO 2ND. BLOCK.
C      HIGH I = 1
C      HIGH J = 2
C      HIGH K = 3
C      LOW I = 4
C      LOW J = 5
C      LOW K = 6
C
C     THE OTHER ARGUMENTS SHOULD NOT BE ALTERED
C
C---- EXAMPLE: ADDING GLUE (ORIENTATION CHANGE I,J,K -> I,-J,K)
C
C     CNAME1 = 'DUCT BOUNDARY1'
C     CNAME2 = 'BOUNDARY2'
C     CALL GLUE (CNAME1,CNAME2,1,5,3
C    +             ,NBLOCK,NPATCH,NGLUE,NDBLK,INFPCH,CPATCH,INFGLU)
C
C---- END OF EXAMPLE
C
C+++++++++++++++++ END OF USER AREA 7 ++++++++++++++++++++++++++++++++
C
C++++++++++++++++ USER AREA 8 +++++++++++++++++++++++++++++++++++++++++
C
C
C---- INFORMATION ON UTILITY ROUTINE GUM
C
C  INTER-BLOCK BOUNDARIES WITH UNMATCHED-GRIDS
C  ARE DEFINED BY CALLS TO THE SUBROUTINE GUM AS FOLLOWS:
C
C     CALL GUM( CLIST1,CLIST2,NNAME1,NNAME2, CPATCH,IBBPP,IBBPD )
C
C  THIS GLUES TOGETHER TWO SETS OF INTER-BLOCK BOUNDARY PATCHES WITH:
C
C      NNAME1 = NO. OF NAMES IN 1ST SET OF INTER-BLOCK BOUNDARY PATCHES
C      NNAME2 = NO. OF NAMES IN 2ND SET OF INTER-BLOCK BOUNDARY PATCHES
C      CLIST1(NNAME1) = NAMES IN 1ST. SET
C      CLIST2(NNAME2) = NAMES IN 2ND. SET
C
C      THE OTHER ARGUMENTS SHOULD NOT BE ALTERED
C
C   NOTE ALSO THAT THE KEYWORD            UNMATCHED GRIDS
C   SHOULD BE INCLUDED UNDER THE COMMAND   >>OPTIONS
C
C
C---- EXAMPLE: ADDING GLUE BETWEEN INTERBLOCK BOUNDARY PATCHES
C             'IBB1' ON ONE SIDE OF AN UNMATCHED GRID INTERFACE
C              AND 'IBB2A' 'IBB2B' ON THE OTHER SIDE
C
C
```

```
C     NNAME1 = 1
C     CLIST1(1) = 'IBB1'
C
C     NNAME2 = 2
C     CLIST2(1) = 'IBB2A'
C     CLIST2(2) = 'IBB2B'
C
C     CALL GUM( CLIST1,CLIST2,NNAME1,NNAME2, CPATCH,IBBPP,IBBPD )
C
C---- END OF EXAMPLE
C
C+++++++++++++++++ END OF USER AREA 8 ++++++++++++++++++++++++++++++++
C
C++++++++++++++++ USER AREA 9 ++++++++++++++++++++++++++++++++++++++++++
C
C
C---- INFORMATION ON COMMON BLOCK /BBCYCL/ XCYCLE(3)
C
C  THIS IS USED TO SPECIFY CYCLIC CONNECTIONS FOR ALL
C  UNMATCHED GRID INTERFACES IN A PERIODIC GEOMETRY.
C
C  XCYCLE(I)=0.0 INDICATES THAT GEOMETRY IS NON-CYCLIC
C                IN COORDINATE DIRECTION I.
C  XCYCLE(I)>0.0 INDICATES THAT GEOMETRY IS CYCLIC
C                IN COORDINATE DIRECTION I,
C                WITH PERIOD XCYCLE(I).
C
C  WHERE I INDICATES THE FOLLOWING COORDINATE
C
C        I      CARTESIAN COORDINATES   CYLINDRICAL COORDINATES
C       ----------------------------------------------------------
C        1             X                    AXIAL COORDINATE
C        2             Y                    NOT APPLICABLE
C        3             Z                    THETA
C
C
C---- EXAMPLE: SET CYCLIC CONNECTIONS IN Z (THETA) DIRECTION ONLY
C              WITH A REPEAT PERIOD OF TWO PI, AS WOULD BE USED
C              IN A CYLINDRICAL COORDINATE PROBLEM WITH A FULL
C              360-DEGREE COMPUTATIONAL DOMAIN.
C
C     TWOPI = 8.0*ATAN(1.0)
C     XCYCLE(1) = 0.0
C     XCYCLE(2) = 0.0
C     XCYCLE(3) = TWOPI
C
C---- END OF EXAMPLE
C
C+++++++++++++++++ END OF USER AREA 9 ++++++++++++++++++++++++++++++++
C
      RETURN
      END
```

Appendix D. ANSYS code used for nonlinear structure analysis and design optimization

The program was developed by Rong Zheng.

```
!finish
!/clear
/PREP7
! Set parameters.
*SET,WWidth,0.00164
*SET,LThick,0.002
*SET,Side,0.055626
*SET,SideW,1.2*WWidth
*SET,CLength,Side-2*SideW
*SET,CWidth,(Side-2*SideW-16*WWidth)/17
*SET,CW,CWidth+WWidth
*SET,YoungE,3e9
!Strain points definition.....(They are used to define Data Table of
nonlinear materials)
*SET,Point1,5.000000000E-05
*SET,Point2,1.000000000E-04
*SET,Point3,2.000000000E-04
*SET,Point4,3.000000000E-04
*SET,Point5,4.000000000E-04
*SET,Point6,6.000000000E-04
*SET,Point7,8.000000000E-04
*SET,Point8,12.000000000E-04
*SET,Point9,16.000000000E-04
*SET,Point10,30.000000000E-04
*SET,Point11,60.000000000E-04
*SET,Point12,100.000000000E-04
*SET,Point13,150.000000000E-04
*SET,Point14,200.000000000E-04
*SET,Point15,280.000000000E-04
*SET,Point16,400.000000000E-04

! Define element type.

ET,1,SOLID92

!*
KEYOPT,1,1,0
KEYOPT,1,2,0
KEYOPT,1,4,0
KEYOPT,1,5,2
KEYOPT,1,6,0
!*

! Define Model.
! Define Channel Geometry
! BLOCK,0,Side,0,Side,0,LThick,
```

```
BLC4,0,0,side,side

BLC4,sidew,sidew,cwidth,clength
BLC4,sidew+cw,sidew,cwidth,clength
BLC4,sidew+2*cw,sidew,cwidth,clength
BLC4,sidew+3*cw,sidew,cwidth,clength
BLC4,sidew+4*cw,sidew,cwidth,clength
BLC4,sidew+5*cw,sidew,cwidth,clength
BLC4,sidew+6*cw,sidew,cwidth,clength
BLC4,sidew+7*cw,sidew,cwidth,clength
BLC4,sidew+8*cw,sidew,cwidth,clength
BLC4,sidew+9*cw,sidew,cwidth,clength
BLC4,sidew+10*cw,sidew,cwidth,clength
BLC4,sidew+11*cw,sidew,cwidth,clength
BLC4,sidew+12*cw,sidew,cwidth,clength
BLC4,sidew+13*cw,sidew,cwidth,clength
BLC4,sidew+14*cw,sidew,cwidth,clength
BLC4,sidew+15*cw,sidew,cwidth,clength
BLC4,sidew+16*cw,sidew,cwidth,clength
BLC4,sidew+cwidth,side-sidew,wwidth,-cwidth
BLC4,sidew+2*cw+cwidth,side-sidew,wwidth,-cwidth
BLC4,sidew+4*cw+cwidth,side-sidew,wwidth,-cwidth
BLC4,sidew+6*cw+cwidth,side-sidew,wwidth,-cwidth
BLC4,sidew+8*cw+cwidth,side-sidew,wwidth,-cwidth
BLC4,sidew+10*cw+cwidth,side-sidew,wwidth,-cwidth
BLC4,sidew+12*cw+cwidth,side-sidew,wwidth,-cwidth
BLC4,sidew+14*cw+cwidth,side-sidew,wwidth,-cwidth
BLC4,sidew+cw+cwidth,sidew,wwidth,cwidth
BLC4,sidew+3*cw+cwidth,sidew,wwidth,cwidth
BLC4,sidew+5*cw+cwidth,sidew,wwidth,cwidth
BLC4,sidew+7*cw+cwidth,sidew,wwidth,cwidth
BLC4,sidew+9*cw+cwidth,sidew,wwidth,cwidth
BLC4,sidew+11*cw+cwidth,sidew,wwidth,cwidth
BLC4,sidew+13*cw+cwidth,sidew,wwidth,cwidth
BLC4,sidew+15*cw+cwidth,sidew,wwidth,cwidth

ASBA,1,all

!Extrude from area to block

VOFFST,35,lthick, ,

!Adding areas

FLST,2,3,5,ORDE,2
FITEM,2,98
FITEM,2,-100
AADD,P51X
FLST,2,3,5,ORDE,2
FITEM,2,92
FITEM,2,-94
AADD,P51X
FLST,2,3,5,ORDE,2
FITEM,2,86
FITEM,2,-88
AADD,P51X
FLST,2,3,5,ORDE,2
```

```
FITEM,2,80
FITEM,2,-82
AADD,P51X
FLST,2,3,5,ORDE,2
FITEM,2,74
FITEM,2,-76
AADD,P51X
FLST,2,3,5,ORDE,2
FITEM,2,68
FITEM,2,-70
AADD,P51X
FLST,2,3,5,ORDE,2
FITEM,2,62
FITEM,2,-64
AADD,P51X
FLST,2,3,5,ORDE,2
FITEM,2,56
FITEM,2,-58
AADD,P51X

FLST,2,3,5,ORDE,3
FITEM,2,6
FITEM,2,-7
FITEM,2,106
AADD,P51X
FLST,2,3,5,ORDE,2
FITEM,2,11
FITEM,2,-13
AADD,P51X
FLST,2,3,5,ORDE,2
FITEM,2,17
FITEM,2,-19
AADD,P51X
FLST,2,3,5,ORDE,2
FITEM,2,23
FITEM,2,-25
AADD,P51X
FLST,2,3,5,ORDE,2
FITEM,2,29
FITEM,2,-31
AADD,P51X
FLST,2,3,5,ORDE,2
FITEM,2,36
FITEM,2,-38
AADD,P51X
FLST,2,3,5,ORDE,2
FITEM,2,42
FITEM,2,-44
AADD,P51X
FLST,2,3,5,ORDE,2
FITEM,2,48
FITEM,2,-50
AADD,P51X

!Materials properties
!*
TB,MELAS,1,1,16, ,
```

```
TBTEMP,353,1
!*
TBMODIF,1,1,Point1
TBMODIF,1,2,Point1*YoungE
TBMODIF,2,1,Point2
TBMODIF,2,2,Point2*YoungE*0.98
TBMODIF,3,1,Point3
TBMODIF,3,2,Point3*YoungE*0.94
TBMODIF,4,1,Point4
TBMODIF,4,2,Point4*YoungE*0.90
TBMODIF,5,1,Point5
TBMODIF,5,2,Point5*YoungE*0.85
TBMODIF,6,1,Point6
TBMODIF,6,2,Point6*YoungE*0.80
TBMODIF,7,1,Point7
TBMODIF,7,2,Point7*YoungE*0.75
TBMODIF,8,1,Point8
TBMODIF,8,2,Point8*YoungE*0.70
TBMODIF,9,1,Point9
TBMODIF,9,2,Point9*YoungE*0.65
TBMODIF,10,1,Point10
TBMODIF,10,2,Point10*YoungE*0.60
TBMODIF,11,1,Point11
TBMODIF,11,2,Point11*YoungE*0.55
TBMODIF,12,1,Point12
TBMODIF,12,2,Point12*YoungE*0.50
TBMODIF,13,1,Point13
TBMODIF,13,2,Point13*YoungE*0.45
TBMODIF,14,1,Point14
TBMODIF,14,2,Point14*YoungE*0.40
TBMODIF,15,1,Point15
TBMODIF,15,2,Point15*YoungE*0.35
TBMODIF,16,1,Point16
TBMODIF,16,2,Point16*YoungE*0.30
!*

!*
UIMP,1,EX, , ,YoungE,
UIMP,1,NUXY, , ,0.37,
UIMP,1,ALPX, , ,6e-5,
UIMP,1,REFT, , , ,
UIMP,1,MU, , , ,
UIMP,1,DAMP, , , ,
UIMP,1,DENS, , ,1299.52,
UIMP,1,KXX, , , ,
UIMP,1,C, , , ,
UIMP,1,ENTH, , , ,
UIMP,1,HF, , , ,
UIMP,1,EMIS, , , ,
UIMP,1,QRATE, , , ,
UIMP,1,VISC, , , ,
UIMP,1,SONC, , , ,
UIMP,1,MURX, , , ,
UIMP,1,MGXX, , , ,
UIMP,1,RSVX, , , ,
UIMP,1,PERX, , , ,
!*
```

```
!Meshing

LESIZE,ALL, , ,6,-2,1, , ,1,
FLST,5,76,4,ORDE,73
FITEM,5,1
FITEM,5,-4
FITEM,5,6
FITEM,5,8
FITEM,5,10
FITEM,5,12
FITEM,5,14
FITEM,5,20
FITEM,5,24
FITEM,5,32
FITEM,5,36
FITEM,5,44
FITEM,5,48
FITEM,5,56
FITEM,5,60
FITEM,5,68
FITEM,5,70
FITEM,5,74
FITEM,5,79
FITEM,5,82
FITEM,5,87
FITEM,5,90
FITEM,5,95
FITEM,5,98
FITEM,5,100
FITEM,5,105
FITEM,5,108
FITEM,5,113
FITEM,5,116
FITEM,5,121
FITEM,5,124
FITEM,5,129
FITEM,5,132
FITEM,5,137
FITEM,5,139
FITEM,5,141
FITEM,5,-142
FITEM,5,144
FITEM,5,-145
FITEM,5,147
FITEM,5,-148
FITEM,5,150
FITEM,5,-151
FITEM,5,153
FITEM,5,-154
FITEM,5,156
FITEM,5,-157
FITEM,5,159
FITEM,5,-160
FITEM,5,162
FITEM,5,-163
FITEM,5,165
```

```
FITEM,5,-166
FITEM,5,168
FITEM,5,-169
FITEM,5,171
FITEM,5,-172
FITEM,5,174
FITEM,5,-175
FITEM,5,177
FITEM,5,-178
FITEM,5,180
FITEM,5,-181
FITEM,5,183
FITEM,5,-185
FITEM,5,187
FITEM,5,191
FITEM,5,193
FITEM,5,197
FITEM,5,199
FITEM,5,203
FITEM,5,205
FITEM,5,207
CM,_Y,LINE
LSEL, , , ,P51X
CM,_Y1,LINE
CMSEL,,_Y
!*
LESIZE,_Y1, , ,16,-2, , , ,1
CMDELE,_Y
CMDELE,_Y1
!*
MSHKEY,0
MSHAPE,1,3d
CM,_Y,VOLU
VSEL, , , ,       1
CM,_Y1,VOLU
CHKMSH,'VOLU'
CMSEL,S,_Y
!*
VMESH,_Y1
!*
CMDELE,_Y
CMDELE,_Y1
CMDELE,_Y2
!*
MSHKEY,0
MSHAPE,1,3d

!Load step..........
!*
TIME,0
AUTOTS,-1
NSUBST,10, , ,1
KBC,0
!*
TSRES,ERASE

FINISH
```

```
/SOLU

!Applying fix bottom

FLST,2,1,5,ORDE,1
FITEM,2,35
!*
/GO
DA,P51X,ALL,0

!Applying top pressure

FLST,2,1,5,ORDE,1
FITEM,2,1
/GO
!*
SFA,P51X,1,PRES,544000

!Applying inner channel pressure

FLST,2,68,5,ORDE,31
FITEM,2,6
FITEM,2,-18
FITEM,2,20
FITEM,2,-22
FITEM,2,26
FITEM,2,-28
FITEM,2,32
FITEM,2,-34
FITEM,2,39
FITEM,2,-41
FITEM,2,45
FITEM,2,-47
FITEM,2,51
FITEM,2,-56
FITEM,2,59
FITEM,2,-62
FITEM,2,65
FITEM,2,-68
FITEM,2,71
FITEM,2,-74
FITEM,2,77
FITEM,2,-80
FITEM,2,83
FITEM,2,-86
FITEM,2,89
FITEM,2,-92
FITEM,2,95
FITEM,2,-98
FITEM,2,101
FITEM,2,-105
FITEM,2,107
/GO
!*
SFA,P51X,1,PRES,204000

!Applying temperature load
```

```
TREF,293,
FLST,2,1,6,ORDE,1
FITEM,2,1
!*
BFV,P51X,TEMP,353

SOLVE

/POST1
/EFACE,1
AVPRIN,0,0,
!*
PLNSOL,S,EQV,0,1
*GET,STSVM,PLNSOL,,MAX
AVPRIN,0,0,
!*
PLESOL,EPTO,1,0,1
*GET,STN1,PLNSOL,,MAX
FINISH
```

```
/OPT
OPANL,try5-opt,txt,
!*
OPVAR,WWIDTH,DV,0.0005,0.0018,0.000001,
!*
OPVAR,LTHICK,DV,0.001,0.002,0.000001,
!*
!OPVAR,YoungE,DV,1e9,1e10,1e4,
!*
OPVAR,STN1,SV, ,0.01,0.000001,
!*
!*
OPVAR,STSVM,OBJ, , ,0.1e4,
!*
```

Appendix E. ANSYS code used for thermal analysis and design optimization

The program was developed by Rong Zheng.

```
!finish
!/clear
/PREP7
! Set parameters.

*SET,WWidth,0.00071
*SET,LThick,0.002
*SET,Side,0.055626
*SET,SideW,1.2*WWidth
*SET,CLength,Side-2*SideW
*SET,CWidth,(Side-2*SideW-16*WWidth)/17
*SET,CW,CWidth+WWidth
*SET,YoungE,3e9
*SET,SpeHeat,1047.6 !Specific Heat: 1047.6 J/kg.c
*SET,Density,1299.52  !Density: 1299.52 kg/m3
*SET,TherK,0.187599 !Thermal Conductivity 0.187599 J/m.s.c
*SET,HeatFlu,1200  !Heat Flux 1200 J/s.m2
*SET,BulkT,90   !Fluid bulk temperature 90 c
*SET,ConvH,80   !Convection coefficient 80 J/s.m2.c
*SET,HeatCoo,3400  !negative Heat Flux for cooling at bottom -200
J/s.m2
*SET,Cooling,-HeatCoo

!Strain points definition.....(They are used to define Data Table of
nonlinear materials)


! Define element type.

ET,1,SOLID87

!* Consistent specific heat matrix
KEYOPT,1,1,0

!*

! Define Model.
! Define Channel Geometry
! BLOCK,0,Side,0,Side,0,LThick,

BLC4,0,0,side,side

BLC4,sidew,sidew,cwidth,clength
BLC4,sidew+cw,sidew,cwidth,clength
BLC4,sidew+2*cw,sidew,cwidth,clength
BLC4,sidew+3*cw,sidew,cwidth,clength
BLC4,sidew+4*cw,sidew,cwidth,clength
```

```
BLC4,sidew+5*cw,sidew,cwidth,clength
BLC4,sidew+6*cw,sidew,cwidth,clength
BLC4,sidew+7*cw,sidew,cwidth,clength
BLC4,sidew+8*cw,sidew,cwidth,clength
BLC4,sidew+9*cw,sidew,cwidth,clength
BLC4,sidew+10*cw,sidew,cwidth,clength
BLC4,sidew+11*cw,sidew,cwidth,clength
BLC4,sidew+12*cw,sidew,cwidth,clength
BLC4,sidew+13*cw,sidew,cwidth,clength
BLC4,sidew+14*cw,sidew,cwidth,clength
BLC4,sidew+15*cw,sidew,cwidth,clength
BLC4,sidew+16*cw,sidew,cwidth,clength
BLC4,sidew+cwidth,side-sidew,wwidth,-cwidth
BLC4,sidew+2*cw+cwidth,side-sidew,wwidth,-cwidth
BLC4,sidew+4*cw+cwidth,side-sidew,wwidth,-cwidth
BLC4,sidew+6*cw+cwidth,side-sidew,wwidth,-cwidth
BLC4,sidew+8*cw+cwidth,side-sidew,wwidth,-cwidth
BLC4,sidew+10*cw+cwidth,side-sidew,wwidth,-cwidth
BLC4,sidew+12*cw+cwidth,side-sidew,wwidth,-cwidth
BLC4,sidew+14*cw+cwidth,side-sidew,wwidth,-cwidth
BLC4,sidew+cw+cwidth,sidew,wwidth,cwidth
BLC4,sidew+3*cw+cwidth,sidew,wwidth,cwidth
BLC4,sidew+5*cw+cwidth,sidew,wwidth,cwidth
BLC4,sidew+7*cw+cwidth,sidew,wwidth,cwidth
BLC4,sidew+9*cw+cwidth,sidew,wwidth,cwidth
BLC4,sidew+11*cw+cwidth,sidew,wwidth,cwidth
BLC4,sidew+13*cw+cwidth,sidew,wwidth,cwidth
BLC4,sidew+15*cw+cwidth,sidew,wwidth,cwidth

ASBA,1,all

!Extrude from area to block

VOFFST,35,lthick, ,

!Adding areas

FLST,2,3,5,ORDE,2
FITEM,2,98
FITEM,2,-100
AADD,P51X
FLST,2,3,5,ORDE,2
FITEM,2,92
FITEM,2,-94
AADD,P51X
FLST,2,3,5,ORDE,2
FITEM,2,86
FITEM,2,-88
AADD,P51X
FLST,2,3,5,ORDE,2
FITEM,2,80
FITEM,2,-82
AADD,P51X
FLST,2,3,5,ORDE,2
FITEM,2,74
FITEM,2,-76
AADD,P51X
```

```
FLST,2,3,5,ORDE,2
FITEM,2,68
FITEM,2,-70
AADD,P51X
FLST,2,3,5,ORDE,2
FITEM,2,62
FITEM,2,-64
AADD,P51X
FLST,2,3,5,ORDE,2
FITEM,2,56
FITEM,2,-58
AADD,P51X

FLST,2,3,5,ORDE,3
FITEM,2,6
FITEM,2,-7
FITEM,2,106
AADD,P51X
FLST,2,3,5,ORDE,2
FITEM,2,11
FITEM,2,-13
AADD,P51X
FLST,2,3,5,ORDE,2
FITEM,2,17
FITEM,2,-19
AADD,P51X
FLST,2,3,5,ORDE,2
FITEM,2,23
FITEM,2,-25
AADD,P51X
FLST,2,3,5,ORDE,2
FITEM,2,29
FITEM,2,-31
AADD,P51X
FLST,2,3,5,ORDE,2
FITEM,2,36
FITEM,2,-38
AADD,P51X
FLST,2,3,5,ORDE,2
FITEM,2,42
FITEM,2,-44
AADD,P51X
FLST,2,3,5,ORDE,2
FITEM,2,48
FITEM,2,-50
AADD,P51X

!Materials properties
!*

!*
UIMP,1,EX, , , ,
UIMP,1,NUXY, , , ,
UIMP,1,ALPX, , , ,
UIMP,1,REFT, , , ,
UIMP,1,MU, , , ,
UIMP,1,DAMP, , , ,
```

```
UIMP,1,DENS, , ,Density,
UIMP,1,KXX, , ,TherK,
UIMP,1,C, , ,SpeHeat,
UIMP,1,ENTH, , , ,
UIMP,1,HF, , ,ConvH,
UIMP,1,EMIS, , , ,
UIMP,1,QRATE, , , ,
UIMP,1,VISC, , , ,
UIMP,1,SONC, , , ,
UIMP,1,MURX, , , ,
UIMP,1,MGXX, , , ,
UIMP,1,RSVX, , , ,
UIMP,1,PERX, , , ,
!*

!Meshing

LESIZE,ALL, , ,6,-2,1, , ,1,
FLST,5,76,4,ORDE,73
FITEM,5,1
FITEM,5,-4
FITEM,5,6
FITEM,5,8
FITEM,5,10
FITEM,5,12
FITEM,5,14
FITEM,5,20
FITEM,5,24
FITEM,5,32
FITEM,5,36
FITEM,5,44
FITEM,5,48
FITEM,5,56
FITEM,5,60
FITEM,5,68
FITEM,5,70
FITEM,5,74
FITEM,5,79
FITEM,5,82
FITEM,5,87
FITEM,5,90
FITEM,5,95
FITEM,5,98
FITEM,5,100
FITEM,5,105
FITEM,5,108
FITEM,5,113
FITEM,5,116
FITEM,5,121
FITEM,5,124
FITEM,5,129
FITEM,5,132
FITEM,5,137
FITEM,5,139
FITEM,5,141
FITEM,5,-142
FITEM,5,144
```

```
FITEM,5,-145
FITEM,5,147
FITEM,5,-148
FITEM,5,150
FITEM,5,-151
FITEM,5,153
FITEM,5,-154
FITEM,5,156
FITEM,5,-157
FITEM,5,159
FITEM,5,-160
FITEM,5,162
FITEM,5,-163
FITEM,5,165
FITEM,5,-166
FITEM,5,168
FITEM,5,-169
FITEM,5,171
FITEM,5,-172
FITEM,5,174
FITEM,5,-175
FITEM,5,177
FITEM,5,-178
FITEM,5,180
FITEM,5,-181
FITEM,5,183
FITEM,5,-185
FITEM,5,187
FITEM,5,191
FITEM,5,193
FITEM,5,197
FITEM,5,199
FITEM,5,203
FITEM,5,205
FITEM,5,207
CM,_Y,LINE
LSEL, , , ,P51X
CM,_Y1,LINE
CMSEL,,_Y
!*
LESIZE,_Y1, , ,16,-2, , , ,1
CMDELE,_Y
CMDELE,_Y1
!*
MSHKEY,0
MSHAPE,1,3d
CM,_Y,VOLU
VSEL, , , ,       1
CM,_Y1,VOLU
CHKMSH,'VOLU'
CMSEL,S,_Y
!*
VMESH,_Y1
!*
CMDELE,_Y
CMDELE,_Y1
CMDELE,_Y2
```

```
!*
MSHKEY,0
MSHAPE,1,3d

!Load step...........
!*
TIME,0
AUTOTS,1
NSUBST,10, , ,1
KBC,0
!*
TSRES,ERASE

!Maximum equilibrium iteration #
NEQIT, 50

FINISH
/SOLU

ANTYPE,0


!Applying bottom cooling flux ((!!!temperature))

FLST,2,1,5,ORDE,1
FITEM,2,35
!*
/GO
!!!DA,P51X,TEMP,353,1
SFA,P51X, ,HFLUX,Cooling


!Applying top heat flux


FLST,2,1,5,ORDE,1
FITEM,2,1
/GO
!*
SFA,P51X, ,HFLUX,HeatFlu


!Applying inner channel convections
FLST,2,68,5,ORDE,31
FITEM,2,6
FITEM,2,-18
FITEM,2,20
FITEM,2,-22
FITEM,2,26
FITEM,2,-28
FITEM,2,32
FITEM,2,-34
FITEM,2,39
FITEM,2,-41
FITEM,2,45
FITEM,2,-47
FITEM,2,51
```

```
FITEM,2,-56
FITEM,2,59
FITEM,2,-62
FITEM,2,65
FITEM,2,-68
FITEM,2,71
FITEM,2,-74
FITEM,2,77
FITEM,2,-80
FITEM,2,83
FITEM,2,-86
FITEM,2,89
FITEM,2,-92
FITEM,2,95
FITEM,2,-98
FITEM,2,101
FITEM,2,-105
FITEM,2,107
/GO
!*
SFA,P51X, ,CONV,ConvH,363

SOLVE

/POST1
!!!!!SET,LAST
/EFACE,1
!*
PLNSOL,TEMP, ,0,
*GET,MaxTemp,PLNSOL,,MAX

*SET,TempTo80,abs(MAXTEMP-353)
!!!!*GET,STN1,PLNSOL,,MAX

FINISH

/OPT
OPANL,try7-thermal,txt,
!*
OPVAR,WWIDTH,DV,0.0005,0.0018,0.000001,
!*
OPVAR,LTHICK,DV,0.001,0.002,0.000001,
!*
!OPVAR,HeatCoo,DV,100,10000,1,
!*
!OPVAR,STN1,SV,,0.01,0.000001,
!*
!*
OPVAR,TempTo80,OBJ,,,0.01,
!*
```